MODELLING AND PERFORMANCE ANALYSIS OF LINEAR FRESNEL COLLECTOR FOR PROCESS HEAT GENERATION FOR ICE CREAM FACTORY IN KONYA

A THESIS SUBMITTED TO
THE GRADUATE SCHOOL OF NATURAL AND APPLIED SCIENCES
OF
MIDDLE EAST TECHNICAL UNIVERSITY

BY

RAHUL SINGH

IN PARTIAL FULFILLMENT OF THE REQUIREMENTS
FOR
THE DEGREE OF MASTER OF SCIENCE
IN
MECHANICAL ENGINEERING

FEBRUARY 2017

Approval of the thesis:

MODELLING AND PERFORMANCE ANALYSIS OF LINEAR FRESNEL COLLECTOR FOR PROCESS HEAT GENERATION FOR ICE CREAM FACTORY IN KONYA

submitted by RAHUL SINGH in partial fulfillment of the requirements for the degree of **Master of Science in Mechanical Engineering Department, Middle East Technical University** by,

Prof. Dr. M. Gülbin Dural Ünver _____
Dean, Graduate School of **Natural and Applied Sciences**

Prof. Dr. Raif Tuna Balkan _____
Head of Department, **Mechanical Engineering**

Prof. Dr. Derek K. Baker _____
Supervisor, **Mechanical Engineering Dept., METU**

Assoc. Prof. Dr. İlker Tarı _____
Co-Supervisor, **Mechanical Engineering Dept., METU**

Examining Committee Members:

Ass't. Prof. Dr. Özgür Bayer _____
Mechanical Engineering Dept., METU

Prof. Dr. Derek K. Baker _____
Mechanical Engineering Dept., METU

Assoc. Prof. Dr. İlker Tarı _____
Mechanical Engineering Dept., METU

Assoc. Prof. Dr. Serkan Kıncal _____
Chemical Engineering Dept., METU

Prof. Dr. Aynur Eray _____
Physics Engineering Dept., Hacettepe University

Date: 03.02.2017

I hereby declare that all information in this document has been obtained and presented in accordance with academic rules and ethical conduct. I also declare that, as required by these rules and conduct, I have fully cited and referenced all material and results that are not original to this work.

Name, Last name : Rahul Singh

Signature :

ABSTRACT

MODELLING AND PERFORMANCE ANALYSIS OF LINEAR FRESNEL COLLECTOR FOR PROCESS HEAT GENERATION FOR ICE CREAM FACTORY IN KONYA

Rahul, Singh

M.S., Department of Mechanical Engineering

Supervisor : Prof. Dr. Derek K. Baker

Co-Supervisor : Assoc. Prof. Dr. İlker Tarı

February 2017, 123 pages

In this thesis, a linear Fresnel collector has been designed to supply solar heat for industrial process. Firstly, optical analysis using ray tracing is done to determine the effects of collector's parameters, such as height of receiver, mirror width and profile, gap between adjacent rows and slope deviation. Afterwards, one-dimensional thermal model is presented which predicts surface temperatures of receiver components and heat loss. The results obtained from both optical and thermal studies are then benchmarked against published data and then applied to design a linear Fresnel collector for an ice cream factory located in Konya (Turkey). The collector's thermal performance is investigated for different weather conditions along with monthly outputs. Furthermore, flux distribution on absorber tube for different sun positions is studied as well.

According to parametric study, slightly curved mirrors are able to collect significantly more solar energy compared to flat ones and optimal optical efficiency is achieved for particular range of collector parameters. The peak thermal efficiency and maximum solar fraction is found to be 66.35% and 33.6% (in July) respectively. Additionally, it is observed that most of the solar radiation is concentrated on the bottom section of the absorber tube; however, same is not true for high values of incidence angle. Therefore, non-uniform flux distribution should be taken into consideration for more accurate thermal analysis of the receiver.

Keywords: Linear Fresnel Collector, Ray Tracing, Solar Heat for Industrial Process, Flux Distribution

ÖZ

KONYA DONDURMA FABRİKASI ISI ÜRETIMI IÇIN LİNEER FRESNEL KOLEKTÖRÜN MODELLENMESİ VE PERFORMANS ANALİZİ

Rahul, Singh

Yüksek Lisans, Makina Mühendisliği Bölümü

Tez Yöneticisi : Prof. Dr. Derek K. Baker

Ortak Tez Yöneticisi : Doç. Dr. İlker Tarı

Şubat 2017, 123 sayfa

Bu tezde, endüstriyel işlemlere güneş kaynaklı ısı sağlamak üzere bir lineer Fresnel kolektörü tasarlanmıştır. İlk önce, ışın izleme kullanan optik analizlerle, alıcı yüksekliği, ayna genişliği ve profili, bitişik sıralar arasındaki boşluk ve eğim sapma gibi kolektör parametrelerinin etkileri belirlendi. Sonrasında alıcı bileşenlerinin yüzey sıcaklıklarını ve ısı kaybını öngören bir boyutlu ısıl model sunuldu. Daha sonra hem optik hem de ısıl araştırmalardan elde edilen sonuçlar, yayınlanan verilerle kıyaslandı ve Konya'da bulunan bir dondurma fabrikası için doğrusal bir lineer Fresnel kolektörü tasarlamak için uygulandı. Kolektörün ısıl performansı, aylık çıktılarla birlikte farklı hava koşulları için incelendi. Ayrıca, farklı güneş pozisyonları için emici tüp üzerindeki akı dağılımı da incelendi.

Parametrik çalışmaya göre, hafif kavisli aynalar düz aynalara göre önemli ölçüde fazla güneş enerjisi toplayabilir ve belirli kolektör parametreleri aralığı için optimum optik verim elde edilir. Pik ısıl verimlilik ve maksimum güneş fraksiyonu sırasıyla %66.35 ve %33.6 (Temmuz ayında) olarak bulundu. Ek olarak, güneş radyasyonunun çoğunun emici borunun alt kısmında yoğunlaştığı gözlemlendi. Gerçi, yüksek güneş düşme açısı değerleri için aynı şey geçerli değildir. Bu nedenle, alıcının daha hassas ısıl analizi için homojen olmayan akı dağılımı göz önünde bulundurulmalıdır.

Anahtar kelimeler: Lineer Fresnel Kolektörü, Işın İzleme Metodu, Endüstriyel Süreçlerde Güneş Isısı, Akı Dağılımı

To The Planet Earth

ACKNOWLEDGEMENTS

I would like to express my deepest gratitude to my supervisor Prof. Dr. Derek Baker and my co-supervisor Assoc. Prof. Dr. Ilker Tari for their guidance, criticism, and encouragement throughout the research.

I would also like to thank Nima Bonyadi, Arash Karshenass, Kazim Sönmek, Cihan Özalevli and Sina Shafee for their help and suggestions.

Finally, I am grateful to my family and Ayşe Saygın for their support, understanding and most of all, their immense patience.

TABLE OF CONTENTS

LIST OF TABLES

TABLES

LIST OF FIGURES

FIGURES

LIST OF SYMBOLS AND ABBREVIATIONS

P_{abs}	Power incident on the absorber tube (W)
N_{Ph}	Number of photons impinging on the receiver
P_{Ph}	Power of each photon calculated using ray tracing (W)
A_P	Aperture area of the collector (m^2)
$n_{receiver}$	Number of photons absorbed by receiver
$n_{aperture}$	Number of photons directly incident upon aperture plane
h	Height of receiver
d_i	Position of the mirrors relative to central axis (m)
I_b	Direct normal irradiance (W m^{-2})
A_w	Collector's aperture width (m)
$r_{abs,i}$	Absorber inner surface radius (m)
$r_{abs,o}$	Absorber outer surface radius (m)
$r_{g,i}$	Glass cover outer surface radius (m)
$r_{g,o}$	Glass cover outer surface radius (m)
$r_{sr,i}$	Secondary reflector inner surface radius (m)
$r_{sr,o}$	Secondary reflector outer surface radius (m)
k_{abs}	Thermal conductivity of absorber tube material (W m^{-2} K^{-1})
k_g	Thermal conductivity of glass cover (W m^{-2} K^{-1})
k_{ins}	Thermal conductivity of insulation (W m^{-2} K^{-1})
h_{HTF}	Convective heat transfer coefficient inside absorber (W m^{-2} K^{-1})
$h_{w,g}$	Convective heat transfer coefficient for glass cover to wind heat exchange (W m^{-2} K^{-1})
$h_{w,sr}$	Convective heat transfer coefficient for secondary reflector to wind (W m^{-2} K^{-1})
T_{HTF}	Average temperature of heat transfer fluid (°C)
$T_{abs,i}$	Average temperature of absorber's inner surface (°C)
$T_{abs,o}$	Average temperature of absorber's outer surface (°C)
$T_{g,i}$	Average temperature of glass cover's outer surface (°C)

$T_{g,o}$	Average temperature of glass cover's outer surface (°C)
T_{env}	Temperature of surrounding (°C)
$T_{sr,i}$	Average temperature of secondary reflector's inner surface (°C)
$T_{sr,o}$	Average temperature of secondary reflector's outer surface (°C)
T_{amb}	Temperature of ambient air (°C)
T_{sky}	Temperature of sky (°C)
$T_{HTF,i}$	Inlet temperature in the absorber tube section of unit length(°C)
$T_{HTF,o}$	Outlet temperature in the absorber section of unit length (°C)
T_i	Temperature at the inlet of the receiver tube (°C)
T_o	Temperature at the exit of the absorber tube (°C)
A_g	Outer surface area of glass cover per unit length (m)
A_{sr}	Inner surface area of secondary reflector per unit length (m)
Q_{sol_abs}	Solar radiation absorbed by receiver tube (W m^{-1})
Q_{conv_HTF}	Convective heat transfer between inner surface of absorber tube and heat transfer fluid (W m^{-1})
Q_{cond_abs}	Heat conduction from outer absorber surface to inner absorber surface (W m^{-1})
Q_{rad_ann}	Heat exchange through radiation between outer surface of absorber and inner glass cover surface (W m^{-1})
Q_{cond_gl}	Conductive heat transfer from inner glass surface to outer glass surface (W m^{-1})
$Q_{rad\_absorbed}$	Solar radiation absorbed by the glass envelope (W m^{-1})
Q_{rad_env}	Radiation heat transfer between glass cover and environment (W m^{-1})
Q_{conv_amb}	Heat transfer through convection to ambient through outer surface of glass cover (W m^{-1})
Q_{rad_sr}	Heat exchange from outer surface of glass cover to inner secondary reflector surface by radiation (W m^{-1})
Q_{cond_sr}	Conductive heat transfer between secondary reflector's inner and outer surface (W m^{-1})
Q_{conv_sr}	Heat transfer to ambient air from outer surface of secondary reflector (W m^{-1})
$Q_{rad\_sr\_amb}$	Radiative exchange between outer secondary reflector surface and sky (W m^{-1})

Q_u	Useful energy gain by the heat transfer fluid in the absorber tube section of unit length (W m^{-1})
Q_{u_tot}	Total energy absorbed by the heat transfer fluid (W)
$\dot{m}$	Mass flow rate of heat transfer fluid (kg s^{-1})
c_{HTF}	Specific heat capacity of heat transfer fluid (J kg^{-1} K^{-1})

GREEK SYMBOLS

θ_c	Half Acceptance Angle (°)
η_{opt}	Optical efficiency
α	Absorptivity of absorber tube
τ	Transmittance of glass cover
ρ_R	Reflectivity of primary mirrors
ρ_{SR}	Reflectivity of primary mirrors
ϕ_T	Transversal incidence angle (°)
ϕ_L	Longitudinal incidence angle (°)
γ_s	Solar azimuth (°)
α_s	Solar altitude (°)
θ_z	Solar zenith angle (°)
ϕ_i	Inclination angle (°)
α_T	Transversal solar altitude angle (°)
σ	Stefan-Boltzmann constant (W m^{-2} K^{-4})
ε_{abs}	Emittance of absorber tube's outer surface
ε_g	Emittance of inner glass cover surface
ε_{sr}	Emittance of secondary reflector's outer surface
α_g	Absorptivity of glass cover
α_{abs}	Absorptivity of receiver tube
τ_g	Transmittance of glass cover
η_{th}	Thermal efficiency of the collector

ABBREVIATIONS

CST	Concentrating Solar Thermal
SEGS	Solar Energy Generating System
PT	Parabolic Trough
PD	Parabolic Dish
CR	Central Receiver
LF	Linear Fresnel
SHIP	Solar Heat for Industrial Processes
IAM	Incidence Angle Modifier
CLFR	Compact Linear Fresnel Reflector
CFD	Computational Fluid Dynamics
TRM	Thermal Resistance Model
DNI	Direct Normal Irradiance
MCRT	Monte Carlo Ray Tracing
HTF	Heat Transfer Fluid

CHAPTER 1

INTRODUCTION

Solar Heat for Industrial Processes (SHIP) is a rapidly emerging application area for Concentrating Solar Thermal (CST) technology due to large market potentials. The importance of Research, Development and Innovation to developing and exploiting SHIP markets is highlighted by the European Union Horizon 2020 project INSHIP: Integrating National Research Agendas on Solar Heat for Industrial Processes (Grant: 731287). INSHIP is a 4-year project that started on 01 January 2017 and includes 28 research partners from 12 different countries. The Center for Solar Energy Research and Applıcatıons (GÜNAM) at Middle East Technical University (METU) is representing Turkey in this project. This thesis is GÜNAM's first scientific work in SHIP technologies and applications. This thesis specifically advances the state-of-the-art in Linear Fresnel (LF) collector design methodologies and demonstrates the methodology through its novel application to process heat for an ice-cream factory in Turkey. Therefore, to provide the background and context required for a group's first scientific work in an area, in this chapter, an introduction to LF and SHIP is presented followed by LF applications for SHIP.

1.1. Linear Fresnel Collector (LF)

A linear Fresnel collector is similar to Parabolic Trough (PT) collector but instead of using a parabolic reflector, flat or curved mirror strips are used to achieve desired aperture area and approximate the parabolic profile as illustrated in Figure 1.1. The receiver is a fixed one unlike parabolic trough and thus made up of fewer moving parts which eliminates the need for strengthening materials. The whole idea of LF is to provide cheaper alternative to PT.

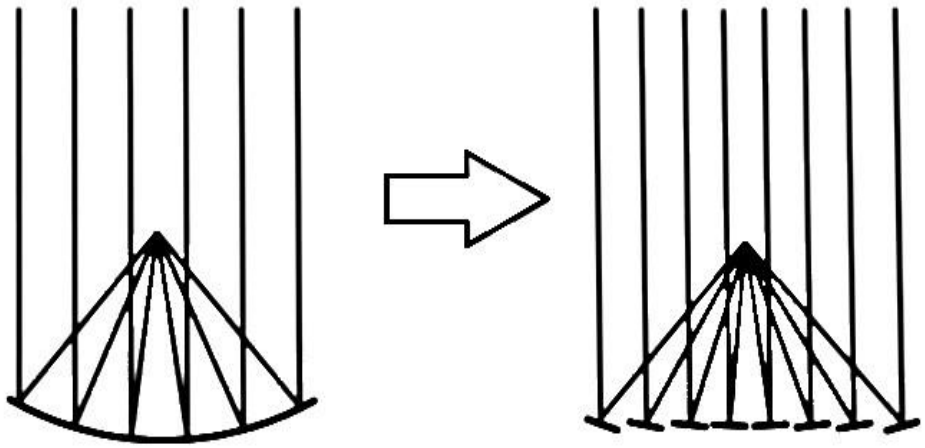

Figure 1.1 Working principle of a linear Fresnel collector.

In some occasions, linear Fresnel systems can serve dual purpose, for example, apart from collecting insolation for process heat or electricity production, LF modules can act as shade for farm animals or parking areas. Along with this, Fresnel collectors are most suited for applications where land availability is restricted such as industrial areas. Additional advantages include lower wind load, mass-produced flat glass mirrors can be used, and lower set-up cost as less building materials like steel and cement are required. Since receiver is the most expensive part of a solar collector, LF's higher mirror surface per unit receiver keeps the price down. On the other hand, drawbacks are lower optical efficiency and immaturity.

A typical LF is shown in Figure 1.2 and main components of a linear Fresnel collector are discussed in the following sections.

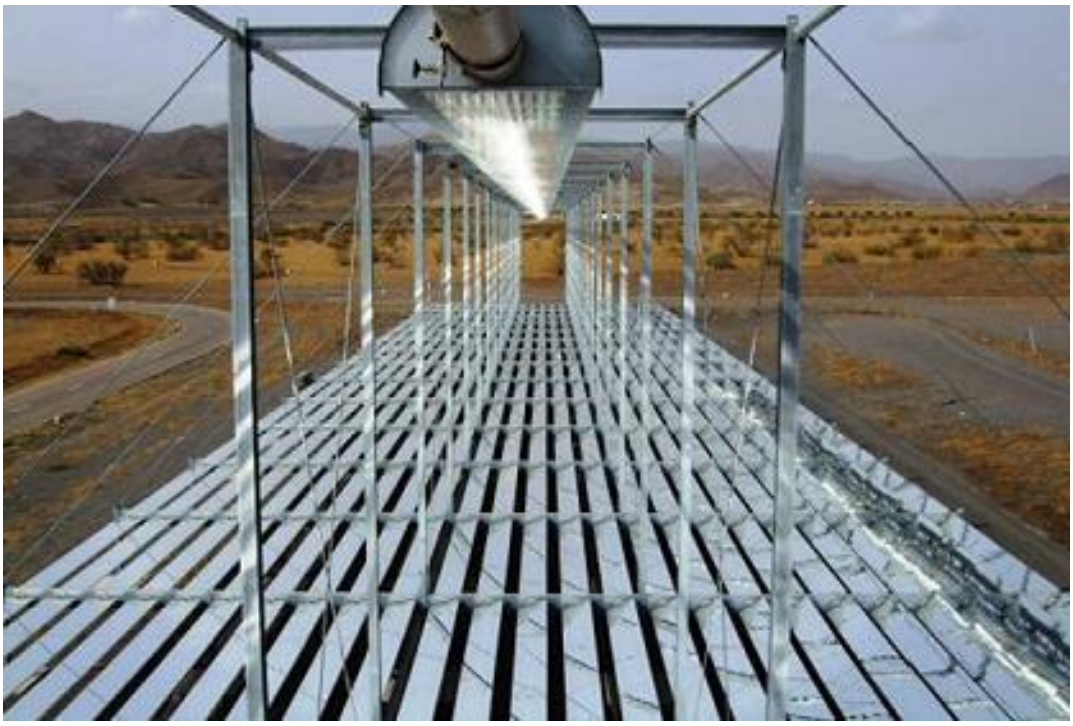

Figure 1.2 A linear Fresnel reflector [1].

1.1.1. Primary Reflectors

The primary reflectors comprise of flat or elastically curved low iron glass mirrors of high reflectivity [2]. The rudimentary production process involves cleaving these mirrors on a corrugated sheet using special glue. The function of corrugated sheet is to act as support for the mirrors and prevent any damage to the reflective paint because of weather. This assembly is then mounted on a frame which is essentially a truss made of galvanized iron (GI) tubes as shown in Figure 1.3. The framework is also fitted with tracking devices assisting the mirrors to trace sun throughout the day.

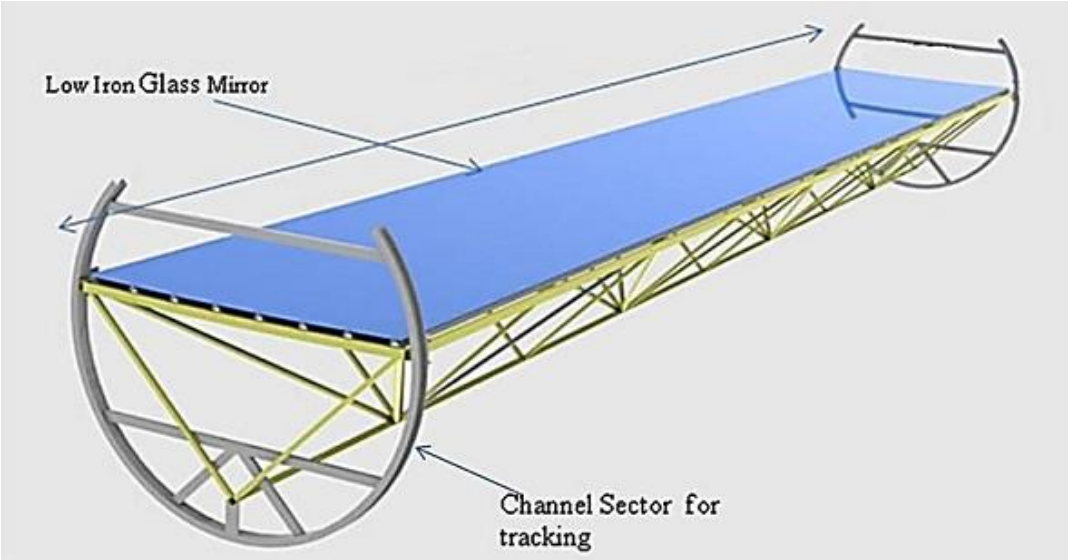

Figure 1.3 Primary reflector of a linear Fresnel collector [3].

1.1.2. Receiver

The receiver of LF, given in Figure 1.4 and Figure 1.5, can be divided into three basic parts: absorber tube, insulation cover and support structures. However many iterations are commercially available nowadays, for example, trapezoidal cavity receivers [4] with multiple non-evacuated absorber tubes (Figure 1.6). The benefit is larger absorber surface area, however, due to significant thermal loss at high temperature, this configuration is most suitable for low temperature processes (180-300°C) [4]. A second common type of receiver is a combination of an evacuated tube with secondary reflector which is used to improve the optical efficiency of the collector. The secondary reflector is in the form of compound parabola which is formed by intersection of two parabolas as illustrated in Figure 1.7 and the design of compound parabola depends on geometry of receiver [2]. The secondary reflector profile is determined using equations described subsequently.

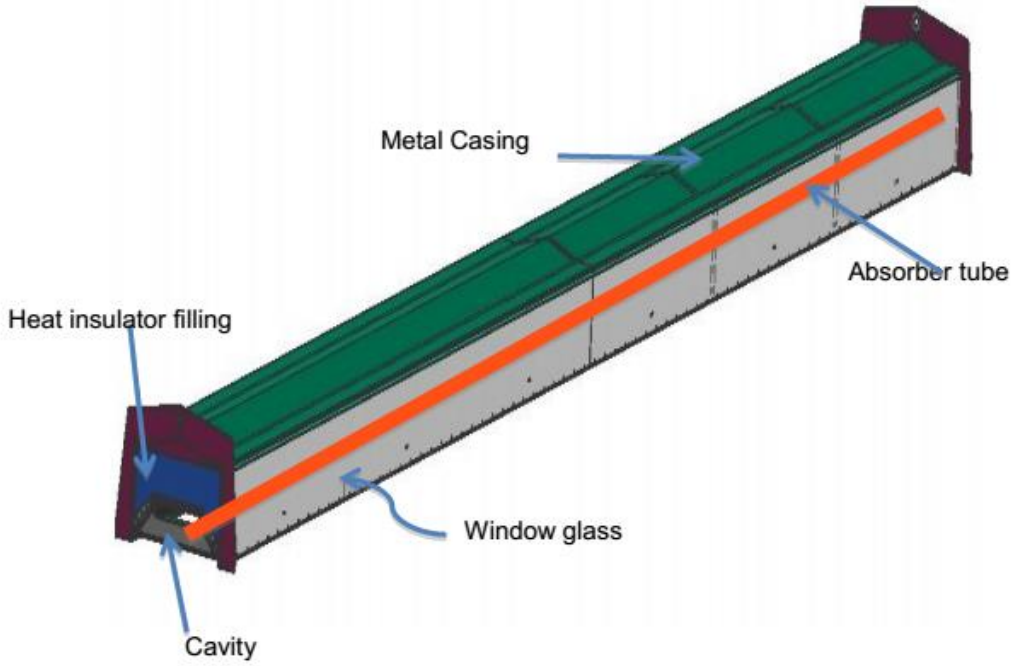

Figure 1.4 Typical receiver of a linear Fresnel collector [3].

Figure 1.5 An installed LF receiver at Plataforma Solar de Almería (PSA), Spain (Photographed by D.Baker and used with permission).

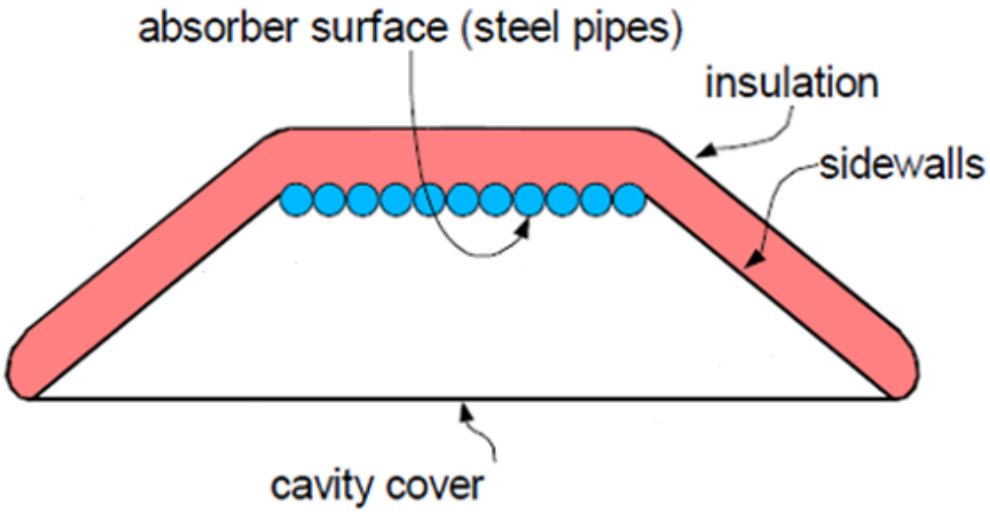

Figure 1.6 A trapezoidal cavity LF receiver [4].

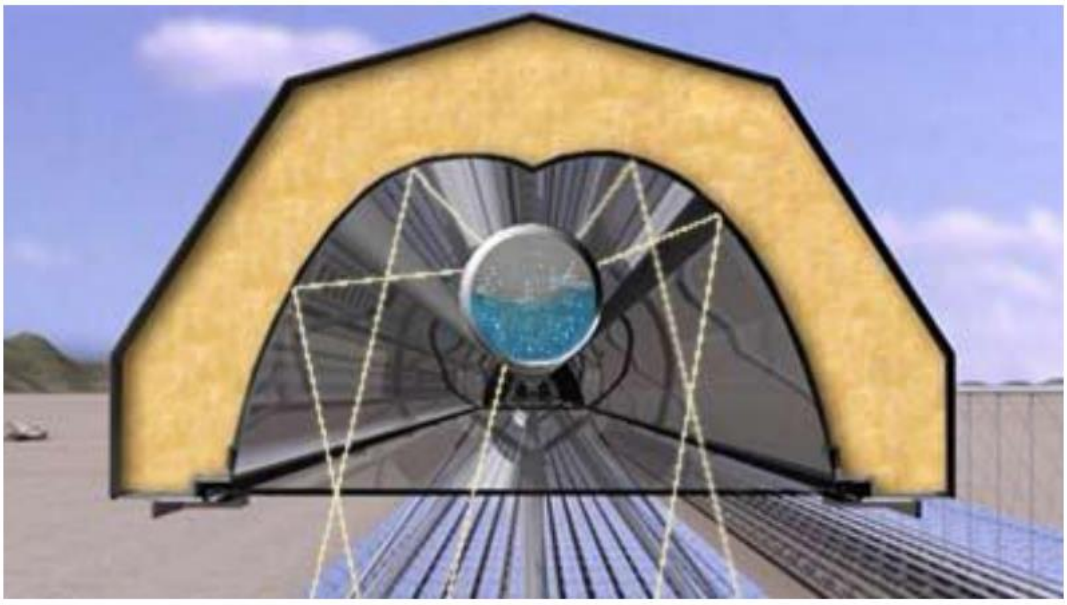

Figure 1.7 Receiver with compound parabolic reflector [4].

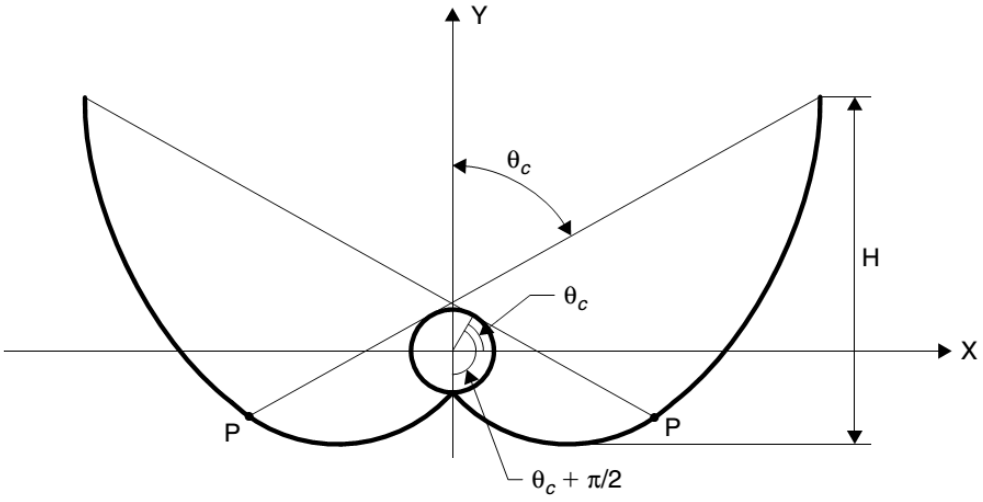

Figure 1.8 Description of compound parabolic geometry [2].

The shape of compound parabola, with maximum possible concentration ratio, for a tubular receiver of radius R and half acceptance angle θ_c, shown in Figure 1.8, is obtained from Equations (1.1) to (1.4) [2].

$$\rho(\theta) = R\theta \text{ for } |\theta| \leq \theta_c + \frac{\pi}{2} \tag{1.1}$$

$$\rho(\theta) = R\left[\frac{\theta + \theta_c + \left(\frac{\pi}{2}\right) - \cos(\theta - \theta_c)}{1 + \sin(\theta - \theta_c)}\right] \text{ for } \left(\theta_c + \frac{\pi}{2}\right) \leq \theta \leq \left(\frac{3\pi}{2} - \theta_c\right) \tag{1.2}$$

And coordinates of point P,

$$X = R\sin(\theta) - \rho\cos(\theta) \tag{1.3}$$

$$Y = -R\cos(\theta) - \rho\sin(\theta) \tag{1.4}$$

The curve generated using above equations is a full untruncated compound parabola and not the most economical choice, therefore, for practical reasons the profile is trimmed slightly at the ends.

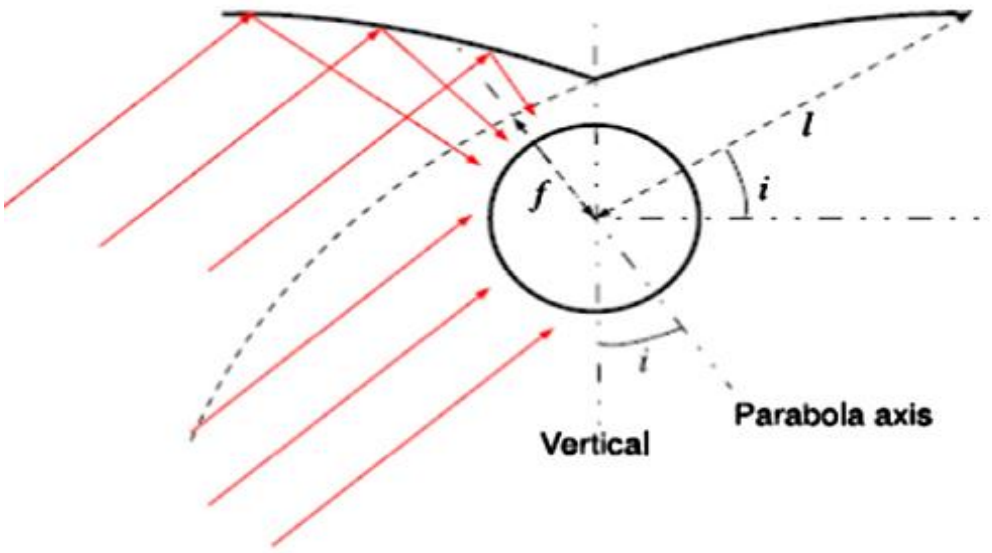

Figure 1.9 A flatter-shaped secondary reflector [4].

Additionally, some recent researches suggest employing a flatter-shaped secondary reflector (Figure 1.9) for enhanced performance [4], on the other hand, there are assertions that using a large-sized evacuated tube absorber makes secondary reflector dispensable and hence reducing the manufacturing and maintenance cost. Moreover, the general consensus on most efficient receiver design is still lacking [4].

Moving on to the absorber, which is a stainless steel tube with selective coating (high absorptivity and low emissivity). The tube may have vacuum glass cover, shown in Figure 1.10, to minimize heat loss. The dimensions of absorber tube such as diameter and thickness are in accordance with operating conditions. The schematic of an evacuated tube receiver is given in Figure 1.11. Next is the outer casing made of cast iron embedded with insulating material like glass wool. A steel structure supports the receiver and must be strong enough to bear the wind load.

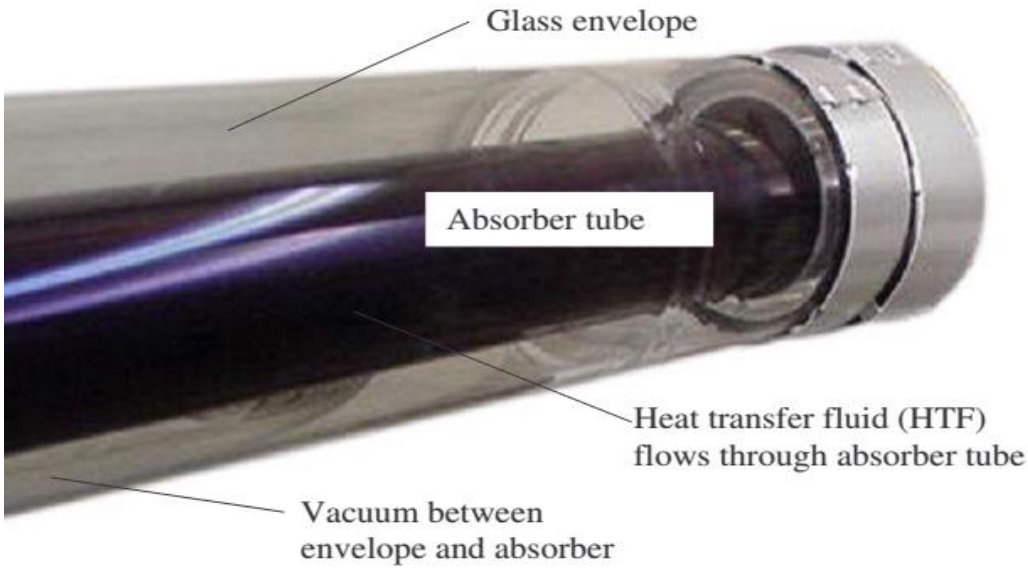

Figure 1.10 An evacuated tube absorber [5].

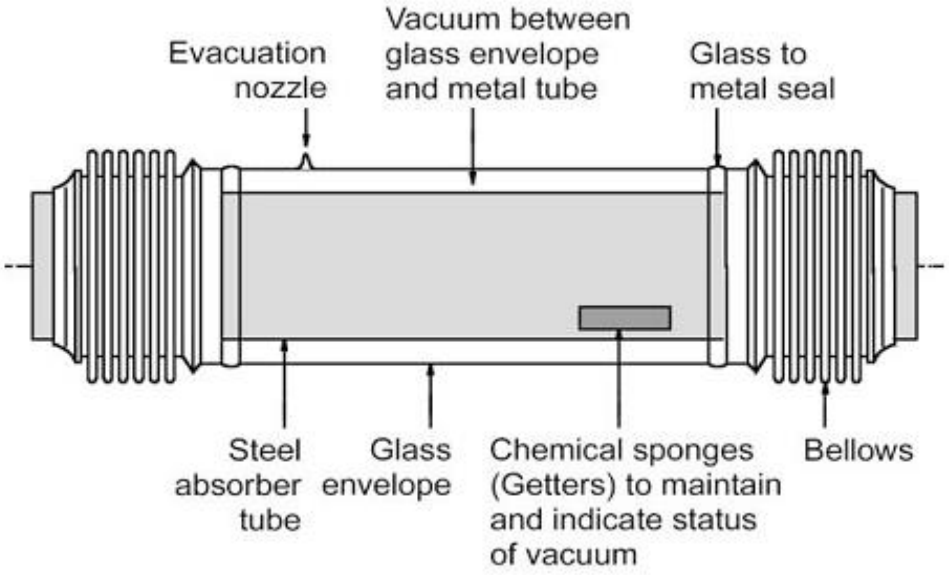

Figure 1.11 Schematic of a vacuum absorber tube [5].

1.1.3. Tracking System

The purpose of tracking mechanism is not only rotating the mirrors to concentrate maximum amount of solar radiation as shown in Figure 1.12, but also defocus mirrors during excessive output, maintenance and emergency situation. In addition to this, tracking also allows mirrors to turn back to their initial position when operation hours end.

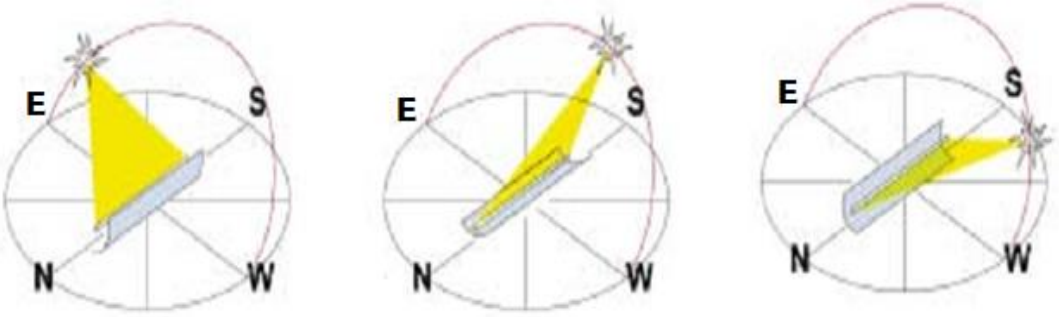

Figure 1.12 Tracking motion of a concentrating collector throughout a day [6].

There are two basic mechanisms of tracking the sun – the altazimuth or two-axis tracking and single-axis tracking. The more efficient but expensive altazimuth method allows collector to track sun in both altitude and azimuth whereas single axis method follows sun either north to south or east to west. The tracking mechanism can be regulated mechanically or electronically with electronic control being more reliable and accurate. The electronic tracking can be achieved by two ways described as [2]:

1. The sensors measure the solar illumination and turn the motor on accordingly.
2. A computer-controlled system with feedback from solar flux sensors on the receiver.

In some modern designs, sun-reflector synchronization is done through GPS devices. The basic elements which drive a tracking mechanism are – stepper motor, gear box and drive train such as sprocket, belt or chain (Figure 1.13). A linear Fresnel collector in the parked (off) position is given in Figure 1.14 and mirror rows are turned to face down using tracking drivers.

Some addenda are given below:

- Potentiometer to measure mirror position
- Heat transfer fluid temperature sensor
- Solar radiation sensors on receiver
- Flow rate meter
- Weather station to measure ambient temperature, humidity and wind velocity
- Back – up power such as battery

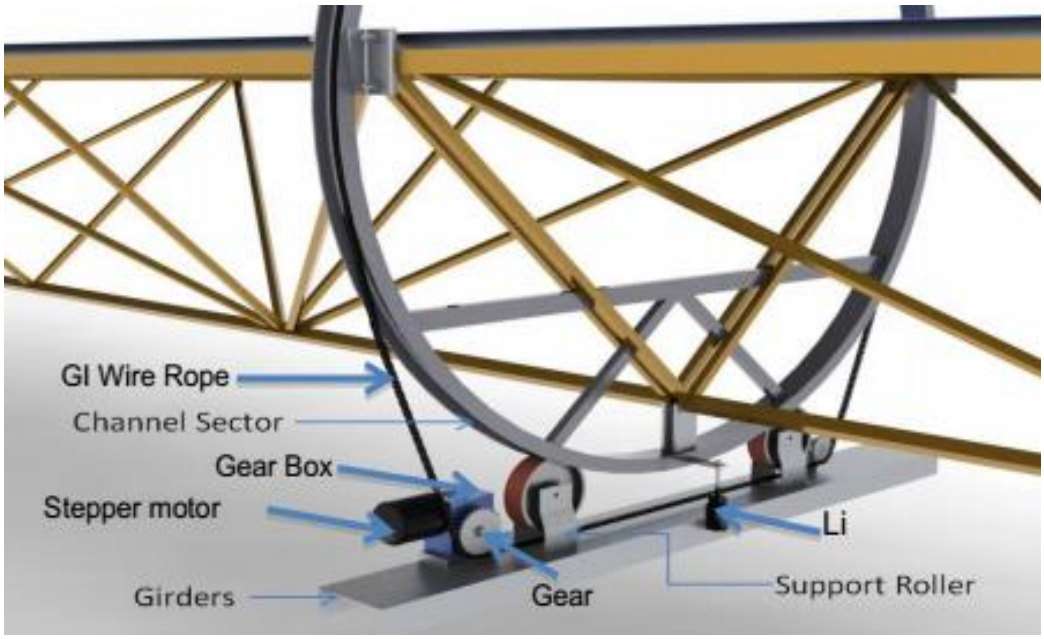

Figure 1.13 Tracking mechanism of a linear Fresnel collector [3].

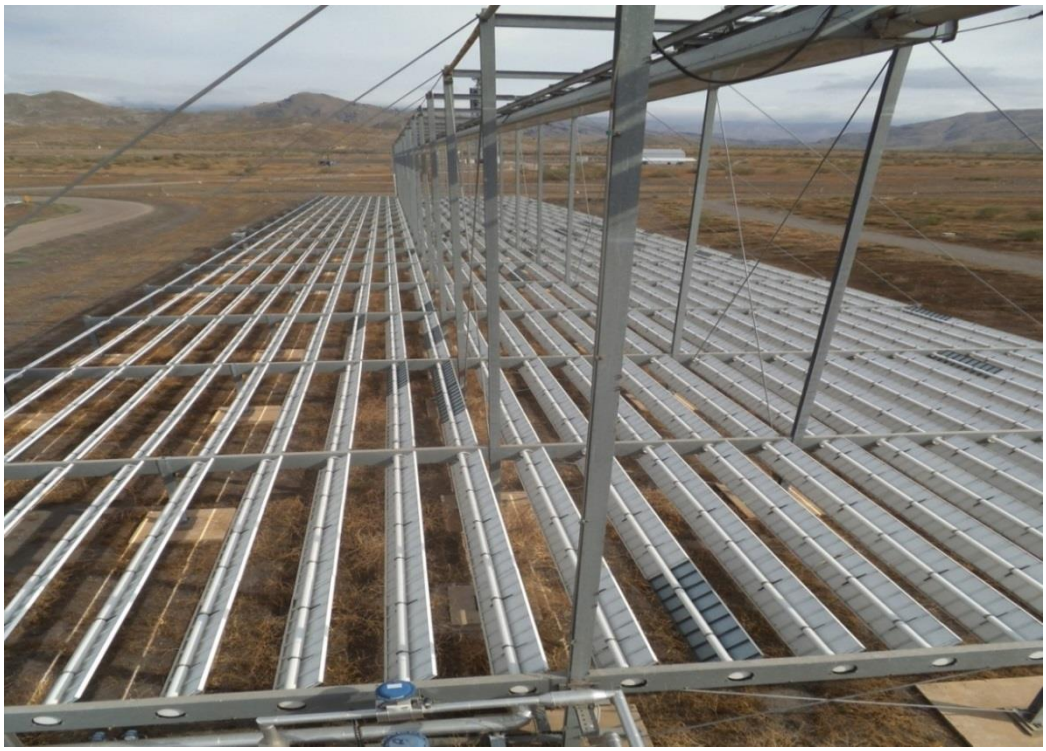

Figure 1.14 LF parked position at Plataforma Solar de Almería (PSA), Spain (Photographed by D.Baker and used with permission).

1.2. Solar Heat for Industrial Process (SHIP)

This section covers the application aspect of concentrating collectors specifically in the industrial sector which consumes a large proportion of the total power consumed and is second only to domestic use, for example, the share of energy consumption by industrial sector in the U.S. is approximately 40% and nearly 60% of which is employed to produce steam or direct heat [7]. The temperature range for most industrial application is 80°C-250°C and about 45% of the process heat is consumed in low and medium heat applications [8].

A list of industries where there is a possibility of energy delivery through solar is given in Table 1.1.

Table 1.1 Industrial processes and working temperature range [2].

Industry	Process	Temperature (°C)
Dairy	Pressurization	60–80
	Sterilization	100–120
	Drying	120–180
	Concentrates	60–80
	Boiler feedwater	60–90
Tinned food	Sterilization	110–120
	Pasteurization	60–80
	Cooking	60–90
	Bleaching	60–90
Textile	Bleaching, dyeing	60–90
	Drying, degreasing	100–130
	Dyeing	70–90
	Fixing	160–180
	Pressing	80–100
Paper	Cooking, drying	60–80
	Boiler feedwater	60–90
	Bleaching	130–150
Chemical	Soaps	200–260
	Synthetic rubber	150–200
	Processing heat	120–180
	Pre-heating water	60–90
Beverages	Washing, sterilization	60–80
	Pasteurization	60–70
Flours and by-products	Sterilization	60–80
Timber by-products	Thermodifussion beams	80–100
	Drying	60–100
	Pre-heating water	60–90
	Preparation pulp	120–170
Bricks and blocks	Curing	60–140
Plastics	Preparation	120–140
	Distillation	140–150
	Separation	200–220

It can be inferred from the Table 1.1 that a significant proportion of low temperature heat is required in food, beverages, paper and textile sector while plastics and chemical industry's heat demand is in medium temperature range, that is, up to 250°C. Solar thermal systems for low heat (less than 150°C) basically consist of flat plate collectors, with or without an evacuated tube, which can supply energy at temperatures around 120°C. The major advantage of this technology is that it is relatively mature and readily available. Some improvements in the design are transparent insulation material which can help flat plate collector to achieve temperatures in the north of 150°C, multiple glazing, employing inert gas or maintaining ultra-high vacuum and adding tracking mechanism [8].

However, such modifications raise question of financial feasibility and therefore in order to supply medium heat (temperature range of 150°C-400°C) solar concentrating collectors are best suited because of high concentration ratio and efficiency. Concentrating collectors have been used for generating electricity for decades and smaller version of similar design can be employed to provide process heat with a capacity of 10 kW_{th} to 2 MW_{th} [8].

The interest in supplying heat for industrial processes through solar energy has been growing worldwide in recent years but with a slow pace. Several projects with a total capacity of 42 MW_{th} were in operation in 2010. In the next four years, the energy supplied by solar reached over 93 MW_{th} with 140 applications around the globe and estimated potential is about 900 GW_{th} in 2030 [8]. That being said, substantial amount of installations are small-scale demonstration projects with 70% of them are based on flat plate collectors.

The largest plant which provides solar process heat started operating in October 2013 and located in a copper mine in Chile [8]. The plant capacity is 32 MW_{th} and covers 85% of demand. Other large scale applications are 9 MW_{th} system in China for a textile industry (opened in 2008) and in 2012, a food processing plant with solar capacity of 5.5 MW_{th} that was developed in the USA.

Developing countries such as India, Turkey and Mexico are also stepping forward in utilizing solar power to fulfill energy demand in industrial sector. A total number of 78 solar concentrating systems for commercial applications were set up in India in 2013 and 61% of the energy generated through solar were utilized for process heat [8]. The capacity factor of solar unit not only depends on the system configuration but also on location, for instance, 4% in regions such as Japan, 16-20% in Middle East and India and 29% in Mexico [8].

Furthermore, solar thermal energy systems for an industrial process and for domestic purpose have several major dissimilarities [7]. First, residential solar heating systems can operate for long durations without any maintenance whereas industrial solar systems require maintenance checks on a regular basis. Second difference is related to social awareness and promotion. Due to several campaigns and advertisements, both by government and private groups, residential solar units have gained popularity and the sales of these systems are driven by both cost savings and environmental concerns. The potential of solar energy for process heat on the other hand has largely been ignored by government and more importantly by the industry where financial feasibility is a significant motive force. Finally, the domestic loads are highly intermittent and depend on the seasons. In contrast, typical industrial demands are unfluctuating all around the year. This results in major design difference between industrial and residential solar system. Domestic systems are typically designed based on peak solar resources while industrial systems are designed based on winter solar resources and are oversized in most cases.

1.3. Challenges for SHIP and Possible Solutions

The market potential for applications of solar heat in industry is rising but still going through elementary stage and there are few hurdles to cope with before reaching maturity. This section enumerates some of the fundamental obstacles in incorporation of solar heat system into industrial processes and strategies to handle these barriers.

The major problems are as follows:

- Lack of awareness – Most companies do not consider or are unaware of solar process heat and go for either photovoltaics or more conventional systems.
- High investment – Current solar systems tend to be expensive especially compared to fossil fuel based options. Higher cost and longer payback time repels the decision makers from investing and due to lack of financial aid small and medium sized enterprises cannot afford such projects.
- Lack of confidence – most of the solar collectors designed for industrial purposes are relatively new and this raises question of durability and reliability.
- Lack of experience – most industrial setups are either pilot projects or small scale and there is deficiency of field experts and guidelines related to planning, installation and maintenance.
- Lack of training – the number of professionals who can actually provide service that industry demands, for example proper installation and maintenance, remains low.

Now the solutions to tackle the challenges mentioned previously:

- Awareness programs and advertising campaigns – events such as conferences, technical and economic presentations etc. should be promoted and focused especially at policy makers both in industry and government.
- Financing – solar process heat projects can be discounted or subsidized. Some investments can also be done in research and development of new technologies like optimized tracking, standardization, cheaper and better materials, for making solar systems more efficient and suitable for industrial use.
- Pilot projects – increase in number of demonstration projects will not only allow planners and installers to gain experience and broaden the planning guidelines but also strengthen the confidence.

- Education and training programs – organization of training courses will help raise awareness as well as improving the quality and number of experts in the field of solar process heat.

1.4. Abridged Summary of SHIP Design

The standard procedure in planning and designing a SHIP project can be split into two steps which are described below:

1. Technical Aspect – This involves considering the demand and constraints. During the technical assessment of a solar project following points should be ruminated:

- Type of process
- Heat demand temperature
- Location such as roof tops
- Collector and heat transfer fluid choice
- Energy storage alternatives
- Heat recovery options

2. Economic Aspect – After investigating the technical feasibility, next step is financial evaluation of the design by determining the following:

- Up-front, operation and maintenance costs
- Cost of generated energy for present and future
- Availability of financial assistance
- Economic parameters like payback time and rate of return

1.5. Scope of LF for SHIP

As mentioned earlier, selecting the type of collector largely depends on operation constraints such as working temperature, location, available space and monetary aspect. Linear Fresnel collector is an attractive option to cope with restrictions imposed by the industrial application and has significant edge over other types of collectors because of its versatility in design, modest land use and reasonable efficiency.

These collectors can be adapted to operate on factory roof-tops or fit in compact areas by varying collector dimensions such as length, width, height of receiver and installing with best suited orientation. The LFs are generally used for district heating/cooling and different kinds of prototypes are being developed all over the globe [8].

The first real world application of LF was done by Giovanni Francia whose design got patented in 1962 [9]. Francia's collector, illustrated in Figure 1.15, was made up of seven aluminum mirror rows each 8 m long and had a width of 1 m and total area covered by the system was about 8.2 X 7.9 m^2. The receiver was 6 m high with approximately 8 m in length and 0.25 m wide. Extra additions to the receiver included a heat recovery device and insulation. Electronic commands and motors helped each row to track sun all day long. According to the experimental results of the prototype in Marseille (France), the collector generated 38 kg h^{-1} of steam at 450°C and 100 atm [9].

In 1965, Francia envisaged the "Solar City Project – Hypothesis for an urban structure" which outlined a layout of constructing solar energy system based on linear Fresnel collector that would be able to meet basic urban energy demands such as space heating/cooling, lightning and electricity. The initial design was aimed at an urban region with population of one hundred thousand. The schematics of Francia's proposal are shown in Figure 1.16 and Figure 1.17.

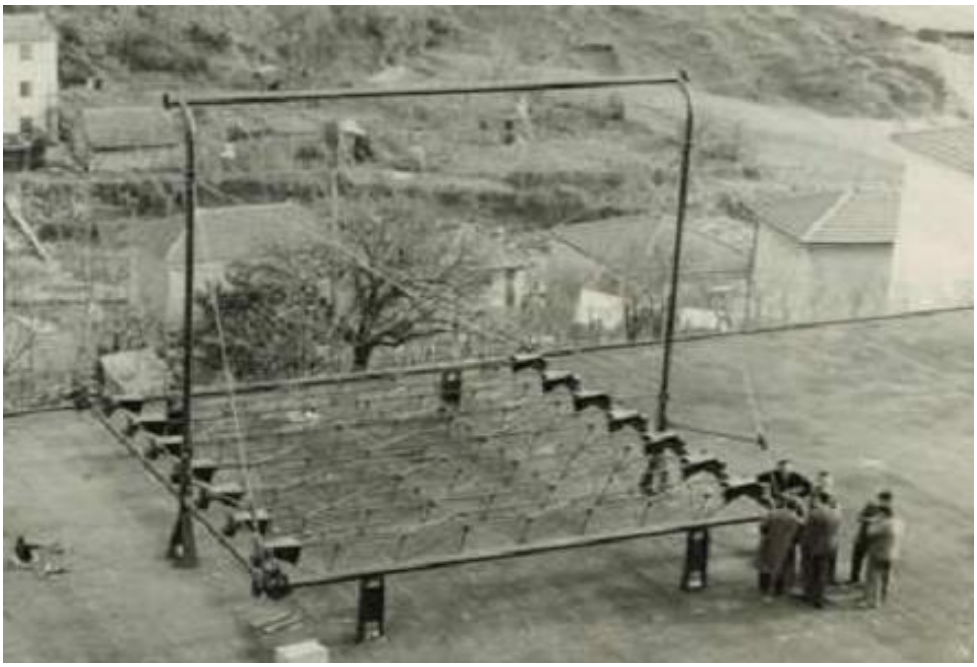

Figure 1.15 Francia's linear Fresnel set -up [9].

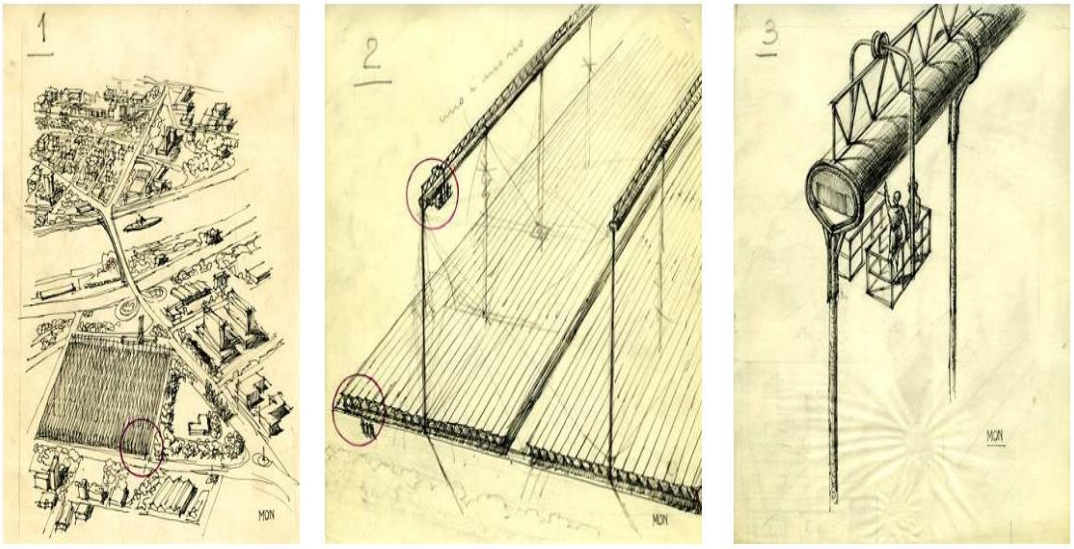

Figure 1.16 Solar City proposal by Francia [9].

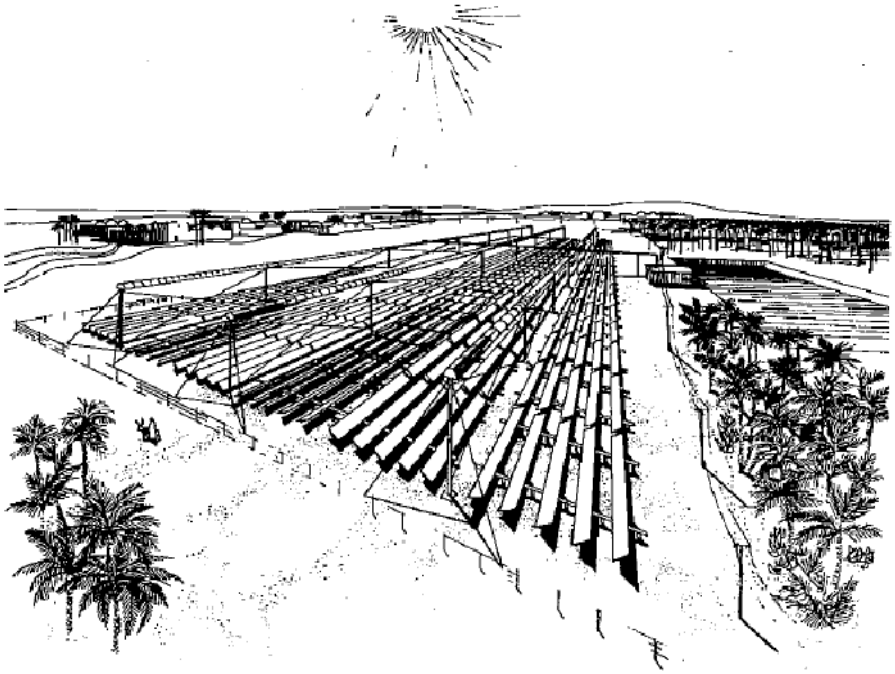

Figure 1.17 Illustration of LF system in urban environment suggested by Francia [9].

Some recent projects related to process heat generation through LF are described in two ways: small scale experimental setups and full size industrial setups. One of the largest experimental installations is at Engineering School of Seville, Spain where a linear Fresnel concentrator is constructed on the roof-top which generates steam and produces 174 kW_{th} supplied to a double effect lithium-bromide water absorption chiller [10]. The solar steam system is also assisted by an auxiliary gas boiler. The project's target is to analyze the performance of the collector and suggest possible improvements in design in order to come up with a set of guidelines for future projects. The installation is shown in Figure 1.18 and the basic design features of the solar steam generation system are summarized in Table 1.2.

Figure 1.18 Experimental unit installed in Seville, Spain [10].

Figure 1.19 Experimental unit installed in Freiburg, Germany [6].

Table 1.2 Design specification of LF set-up in Seville, Spain [10].

Characteristic	**Value**	**Unit**
Number of mirror rows	11	-
Number of mirrors in each row	16	-
Total collector area	352	m^2
Row spacing	0.2	m
Mirror profile	Curved	-
Focal length of mirrors	8.6 – 10.6	m
Reflectivity of primary reflectors at normal incidence	0.92	-
Receiver type	Schott PTR 70	-
Absorptivity of receiver at normal incidence	0.95	-
Receiver height above primary reflector plane	4	m
Total receiver tube length	64	m
Secondary reflector material	Polished aluminium	-
Reflectivity of secondary reflector	0.77	-
Maximum temperature	200	°C
Peak pressure	13	bar
Nominal flowrate	13	$m^3 h^{-1}$

According to the experiments conducted in May, 2009, nominal temperature output was 174°C and 72% average absorber efficiency. Other previous projects based on similar LF are – a prototype installation in Freiburg, Germany (Figure 1.19) where experimental analysis was done during summer of 2006 and another 132 m^2 system manufactured in Bergano, Italy, shown in Figure 1.20, which was coupled with ammonia-water absorption chiller [6].

Figure 1.20 Experimental unit installed in Bergamo, Italy [6].

Experimental units outside of Europe were installed in India [11] and Algeria [12] both of which are illustrated in Figure 1.21 and Figure 1.22 respectively.

The roof top installation in India consists of flat mirrors of 0.5 m width and 1 m length. The receiver is double tube with trapezoidal cover and wool insulation. Tracking is achieved by using four bar link mechanism which tracks sun from east to west and a motor which rotates the gear, attached to each mirror row, at 15° per hour. The experimental results showed that steam at a rate of 2.4 kg h^{-1} and 6.3 kg h^{-1} at 1.5 bars can be generated with total reflector area of 5 m^2 and 13 m^2 respectively.

The small LF prototype at Saad Dahlab University, Blinda, Algeria was evaluated in winter of 2015 using tap water as heat transfer fluid. The total area of system was 1.65 m^2 with 11 flat mirror strips and each strip 1.5 m long and 0.1 m wide. The receiver was 1.6 m long and made of four selectively coated copper tubes inside a trapezoidal cavity. The results from analysis done on 22nd January 2015 and 19th February 2015 indicated that thermal efficiency of the system was close to 29% and 74°C maximum output water temperature

Figure 1.21 Experimental unit installed in New Delhi, India [11].

Figure 1.22 Experimental unit installed in Blinda, Algeria [12].

An outdoor test unit, given in Figure 1.23, was constructed in Isparta, Turkey using 10 flat mirror strips of 1.8 m length and 0.38 m width each and copper tube in trapezoidal cavity as receiver with glass wool insulation [13]. System analysis was done on 2nd August, 2012 by circulating water at 0.025 kg s^{-1}. Maximum temperature difference of 23°C between inlet and outlet was recorded and peak efficiency during the day was 34.1%.

Figure 1.23 Experimental unit installed in Isparta, Turkey [13].

In addition to experimental prototypes, an operational industrial setup is installed in South Africa at datacenter of a telecommunication company [14]. This roof top unit, presented in Figure 1.24, has a peak cooling capacity of 330 kW and used as a power source for driving a lithium bromide-water absorption chiller. Employing such a system for cooling purposes brings down both ozone depletion potential and global warming potential of the refrigerant to naught. The total collector area is 484 m^2 and made up of 22 LF modules (11 mirror rows in each module). Tracking is done through a computer code in which GPS coordinates, date, time and mirror inclination are control inputs.

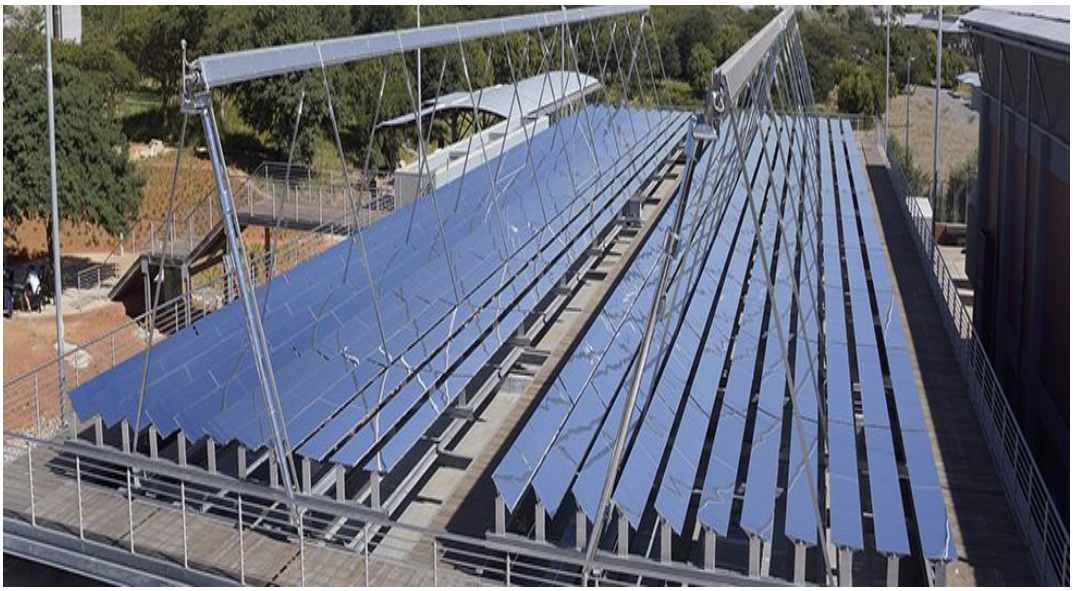

Figure 1.24 The roof-top installation in South Africa [14].

The receiver is a combination of an evacuated tube and compound parabolic secondary reflector to prevent radiation spillage. The working fluid is water which is heated to maximum temperature of 180°C at 12 bars and return temperature is 165°C. The output of the system is controlled either by varying flowrate of the water or defocusing mirror rows in case of excess energy collection. The safety protocols are also installed for emergency situations, for example high wind load or pressure variation and no flow, during which the tracking system turns the mirrors into stow position.

An extra power back up is provided in case of outage and other additional features include automatic self-cleaning position adjustment when it rains. The LF system contributes up to half of the total cooling demand of the datacenter

An LF system, shown in Figure 1.25, is installed at a mining site in Aydin,Turkey to assist in ore drying process and curtail LNG consumption [15]. The plant capacity is 1 MW_{th} and annual energy production is 1.4 GWh_{th} and system is used to generate hot pressurized water at 200°C.

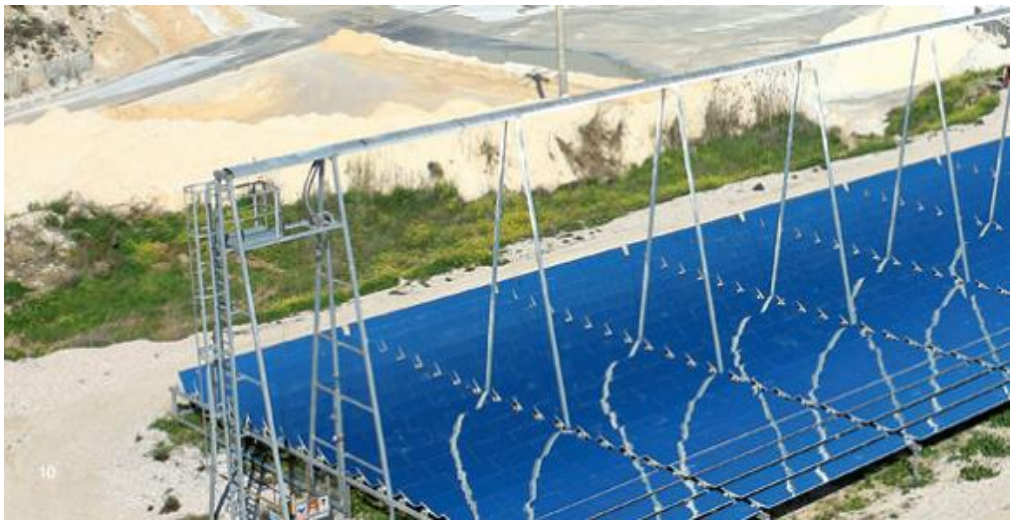

Figure 1.25 LF system at mining site in Turkey [15].

In Jordan, a LF based direct steam generation unit is installed in a pharmaceutical company [16]. The collector comprises of 18 Fresnel modules of 22 m^2 each which are set up on factory's roof top. The receiver is evacuated tube place 4.5 m above ground and other components are steam drum, recirculation and feed pumps, treated water tank and steam interface to the factory. The plant capacity is 222 kW_{th} and will be used to supply steam at 166°C and 6 bars as depicted in the Figure 1.26.

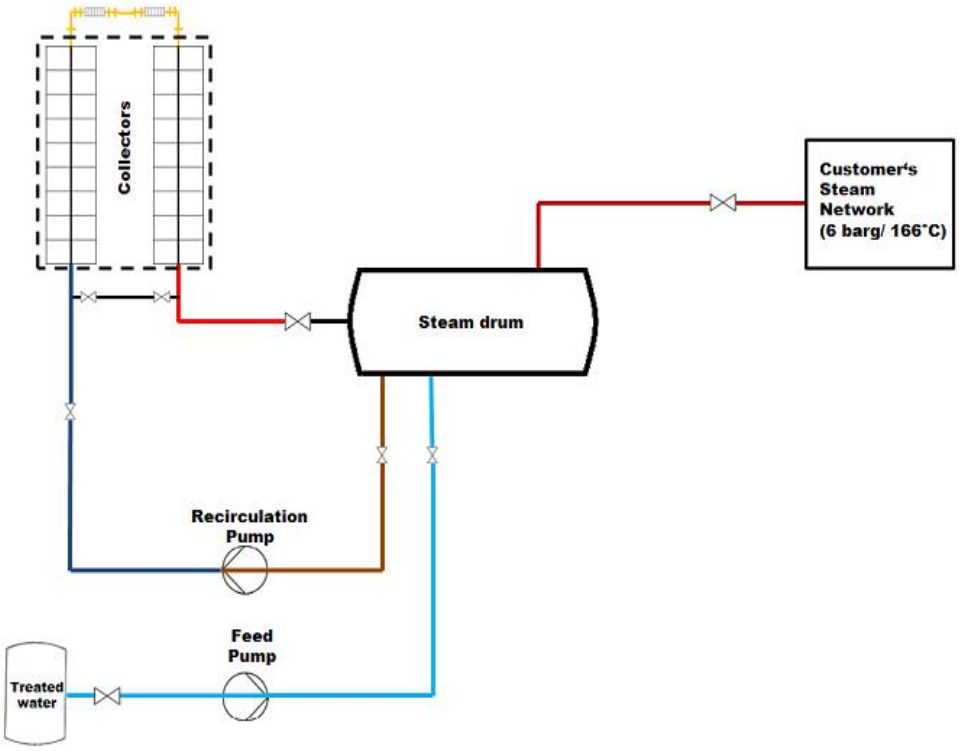

Figure 1.26 Diagram of direct-steam LF system planned in Jordan [16].

CHAPTER 2

LITERATURE REVIEW AND OBJECTIVE

In this chapter a more focused literature review on the state-of-the-art in LF design methodologies is presented in two sections – Optical and Thermal. This chapter concludes with the definition for the objectives and scope for this thesis, and the organization for the rest of the chapters.

2.1. Literature Review of Optical Analysis

A case study on optimization of gap between mirror rows to achieve peak power output was performed by Nixon and Davies [17]. The analysis was done in terms of exergy per unit total mirror area and cost per exergy. First a method to determine appropriate mirror spacing and shadow efficiency was developed. This method was then used to calculate cost per exergy for an LF system in Gujarat, India. The results showed that the mirrors should be aligned in such a way that shading between mutual rows begins at a transversal incidence angle of 45° which was achieved by uneven row spacing but cost sensitivity analysis must be done in locations with high land cost.

A design method was developed by He et al. [18] to calculate efficiency of mirror elements through ray tracing and geometrical study. Simulations were performed by varying mirror width and receiver height using an LF collector with eight mirror rows. It was found that mirrors closer to the central line of the collector had higher efficiency than outer rows at normal incidence.

Furthermore, in the morning rows on the East side performed better than Western rows, however, reverse was observed for the times after solar noon, that is, West side efficiency was higher than East side during second half of the day.

A theory on optical design process of LF reflectors was presented by Abbas et al. [19]. The purpose of the study was analysis and optimization of collector's performance using a Monte Carlo model. According to simulation results, width of individual mirrors affected radiation deviation and should be optimized according to requirement. Along with this, the choice of mirror geometry and surface quality should also be considered during designing process.

Zhu [20] developed an analytical approach, for optical analysis of LF collector, called FirstOPTIC which is basically a batch of MATLAB code. The results were validated by comparing with previously verified ray tracing program SolTrace. The study focused on calculation of incidence angle modifier (IAM) and suggested that dividing IAM into longitudinal and transversal can provide results with reasonable accuracy.

Abbas et al. [21] studied performance of an LF prototype using ray tracing model. Detailed analysis was done on performance of flat as well as curved mirrors coupled with a trapezoidal cavity multi-tube receiver. It was concluded that reflectors with slight curvature lead to significantly higher concentration ratio – almost four times than that of flat mirrors.

A performance comparison between linear Fresnel reflector (LFR) and compact linear Fresnel reflector (CLFR) was carried out by Montes et al. [22]. The results showed decrease in shading and blocking losses in case of CLFR but the amount of radiation incident on the receiver was lower compared to LFR because of beam spread as mirror rows are aligned farther away from receiver in CLFR. The overall efficiency of LFR was found to be higher than that of CLFR.

Huang et al. [23] presented a model for optical analysis of a solar azimuth tracking LF collector. The results obtained from analytical model were compared with ray tracing software SolTrace. The model predicted total efficiency of 61% which was higher than parabolic trough collector operating at similar conditions. Along with this, it was observed that height of receiver affected shading and blocking among mirror rows – as height was increased, shading and blocking also went up. Also, width of receiver influenced heat loss significantly.

Variation in shading and blocking with respect to row spacing, receiver height and collector orientation was analyzed by Sharma [24]. The results showed that shading and blocking changed substantially during the day but not much in a year for North-South oriented collector (axis of rotation in the North-South plane). On the other hand, opposite behavior was observed for East-West orientation, that is, significant variation with months but not during the day. Furthermore, in North-South orientation, shading was zero at noon and maximum during low solar altitude (near sunrise and sunset time) whereas blocking peaked at noon and during sunrise and sunset dropped to zero. When East-West orientation was considered, results showed least shading around summer solstice and maximum around winter solstice but vice-versa for blocking – minimum around winter solstice and maximum around summer solstice.

A mathematical model for calculation of optical losses, such as end losses, cosine losses, shading and blocking losses, was developed by Song et al. [25]. This model was eventually used to study the effect of design parameters like height of receiver, width of reflectors and gap between the rows. It was observed that for receiver height below 3 m, the losses due to receiver's shadow were significant so recommended height was greater than 3 m. additional results showed decrease in shading and blocking on increasing row spacing, however, wider mirrors lead to lower optical efficiency because of higher shading and blocking.

In a work presented by Abbas and Val [26], a novel LF collector design was analyzed, over a period of one year, using ray tracing. Results showed 0.4% gain in collected energy by using variable spacing between adjacent rows. The reflectors were aligned in such a way that shading and blocking were the least. Furthermore, it was advised to employ a design with variable gap instead of variable mirror width due to higher efficiency and cost effectiveness.

A yearly analysis on influence of field parameters (collector length and width, receiver height, row spacing, number of rows and collector orientation) was done by Sharma et al. [27]. The results were used to find out optical as well as thermal losses and finally amount and cost of electricity generated. According to the results, the energy losses were affected by the ratio of the length of collector to the width of reflector due to end effects. Along with this, East-West orientation had more annual energy losses compared to North-South orientation because of cosine losses. A sample simulation showed annual energy loss of 32.7% in East-West orientation and 25.1% in case of North-South for Murcia, Spain.

Hofer et al. [28] tested a small scale LF collector using two methods – Quasi-Dynamic Testing (QDT) and Dynamic Testing (DT). Biaxial incidence angle modifier (IAM) was obtained using both methods and results were compared with ray tracing simulations. The comparison showed that, on average, the differences in IAM values were under 0.017.

The optical performance of an LF collector was compared with parabolic trough collector (PTC) by Abbas et al. [29]. Two types of receivers were considered in the study – multi-tube receiver and secondary reflector receiver. A Monte Carlo ray tracing code was used to evaluate optical efficiency and flux distribution on receivers. PT achieved maximum efficiency and the LF collector with multi-tube receiver was least efficient among the lot. Additionally, it was concluded that North-South orientation was most efficient for PT, however, same was not true for LF collector, for which performance was similar for both orientations.

A mathematical model was developed by V. Sharma et al. [30] to calculate shading and blocking in a compact linear Fresnel reflector (CLFR). The CLFR design included two fixed parallel receivers and 2n number of mirror rows. The results suggested that the ideal collector configuration was the one in which mirror rows direct radiation on to corresponding nearer receiver and the mirror rows between the receivers reflect in alternate order. This configuration resulted in minimum blocking, maximum energy collection and least cost of electricity.

A Monte Carlo ray tracing method was developed by Benyakhlef et al. [31] in order to study the effect of curvature of mirrors on the flux distribution over the receiver and optical efficiency of a linear Fresnel collector in Morocco both of which were found to be highly dependent on mirror curvature and height of receiver. Higher concentration ratios could be obtained using curved mirror and an inverse relationship between mirror curvature and receiver height was observed, that is, the collectors with low receiver height were affected most by the change in mirror curvature. It was suggested that curved mirrors can lead to reduction in overall cost by improving optical efficiency and decreasing size of receiver.

2.2. Literature Review of Thermal Analysis

A detailed thermal analysis of an evacuated tube receiver was done by Foristall [32] using both one and two dimensional heat transfer models. The results were then compared with the ones obtained from laboratory tests and good agreement was seen between theoretical and experimental surface temperatures.

Burkholder and Kutscher [33] performed tests on two Schott PTR70 receivers to determine heat loss for temperature range 100°C to 500°C. The experimental results were found to be close to predictions made by one dimensional heat loss model. Furthermore, the test results were used to develop heat loss correlations for commercial software like Excelenergy and System Advisor Model (SAM).

A performance analysis of small scale LF collector with two-tube trapezoidal cavity receiver was done by Sen et al. [11]. The collector was equipped with four bar link

mechanism for single axis tracking and orientation was along North-South axis. The collector could produce 2.4 kg\h and 6.3 kg\h steam at 1.5 bar with reflector area of 5 m^2 and 13 m^2 respectively.

A one-dimensional heat loss model was developed by Pino et al. [10] for an LF with secondary reflector and evacuated tube receiver. The maximum output temperature was set to be 170°C and 13 m^3/h flowrate.

This model was compared with experimental results and the difference between calculated and measured output temperature and heat absorbed by receiver was found to be below 1% and 7% respectively. Along with this, during the experiment, the average efficiency of the receiver was 72%.

Hemisath et al. [34] presented two different methods for heat loss calculations and temperature distribution of receiver. First procedure using ray tracing combined with CFD and second was Thermal Resistance Model (TRM). The TRM gave similar results when compared with CFD model, however, the advantage of latter was detailed representation of convection and temperature distribution but was relatively time consuming. It was concluded that for absorber temperature close to 250°C and above, the radiation absorbed by secondary reflector should be taken into consideration.

An experimental investigation of thermal efficiency of an LF located in Isparta, Turkey was done by Dostucok et al. [13]. Empirical relations were used to design the collector and predict its performance. The results were presented for 2nd August and peak thermal efficiency of collector was 34%. Furthermore, it was observed that ambient conditions did not influence thermal efficiency significantly.

A numerical study on heat loss from a non-evacuated receiver was performed by Patil et al. [35]. The aim of the study was to determine temperature and flux distribution on the receiver. The analysis showed 140% increase in convection losses when wind velocity was changed from 0 to 10 m/s; however, there was a decline of 71% in the losses due to radiation. Hence the increase in the net heat loss was not as substantial as convection losses. In addition to this, the difference between heat loss

obtained by considering uniform and non-uniform temperature distribution was found to be 1.5%.

Design optimization of a non-evacuated receiver using CFD was presented by Patil et al. [36]. Non-uniform temperature distribution was considered and non-uniformity was defined using sinusoidal ad square wave functions. According to simulations, in case of non-evacuated receiver, non-uniform temperature distribution resulted in lower heat losses compared to uniform temperature distribution and both sinusoidal and square wave functions made similar heat loss predictions. Along with this, it was observed that heat losses rose with increase in hour angle for fixed absorber temperature and non-uniformity. Hence, it was advised to design collector so that significant amount of radiation is concentrated at the bottom of the receiver.

Reddy and Kumar [37] performed a two-dimensional numerical analysis of convective and radiation losses in an inverted trapezoidal cavity receiver with multiple tubes and glass shield. The study was done by varying receiver dimensions, operating temperature and ambient conditions. In the optimum design proposed in the research, convective and radiative heat losses were 12.76% and 54% lower respectively. Furthermore, radiation losses from glass shield were found to be most significant compared to other losses for all geometries considered in the study.

A modular object-oriented methodology for thermal analysis of an LF's receiver was presented by Guadanud et al. [38]. The aim of the study was to develop suitable and versatile method for accurate thermal analysis of receiver. The temperature distribution inside the receiver, obtained after simulation, is shown in Figure 2.1.

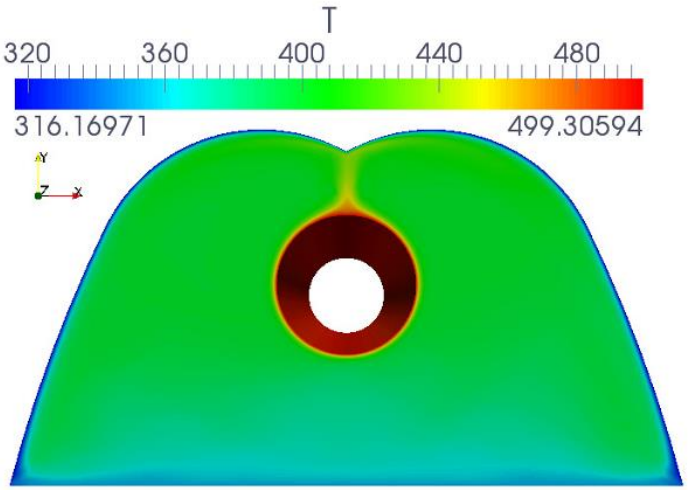

Figure 2.1 Temperature distribution in receiver cavity [38].

Xu et al. [39] developed a thermal resistance model to calculate thermal losses and useful energy gain in a non-evacuated tube receiver with secondary reflector and glass shield. The results obtained from thermal analysis were later used to estimate performance of an LF for direct steam generation.

A detailed study on effect of radiation absorption by secondary reflector on receiver heat loss through thermal resistance model was done by Hofer et al. [40]. Three types of receiver configurations were considered – absorber with non-evacuated glass envelope, evacuated tube absorber and absorber tube with flat glass shield. The analysis was done for temperature range 100°C to 550°C where 100°C-250°C called small-scale and 250°C-550°C as large-scale. Heat loss and secondary reflector surface temperature with respect to absorber temperature are shown in Figure 2.2. The heat losses as well as secondary reflector surface temperatures were least for evacuated tube receiver. Also, for small-scale applications, it was suggested to use receiver with glass shield because of easier construction and performance similar to non-evacuated receiver.

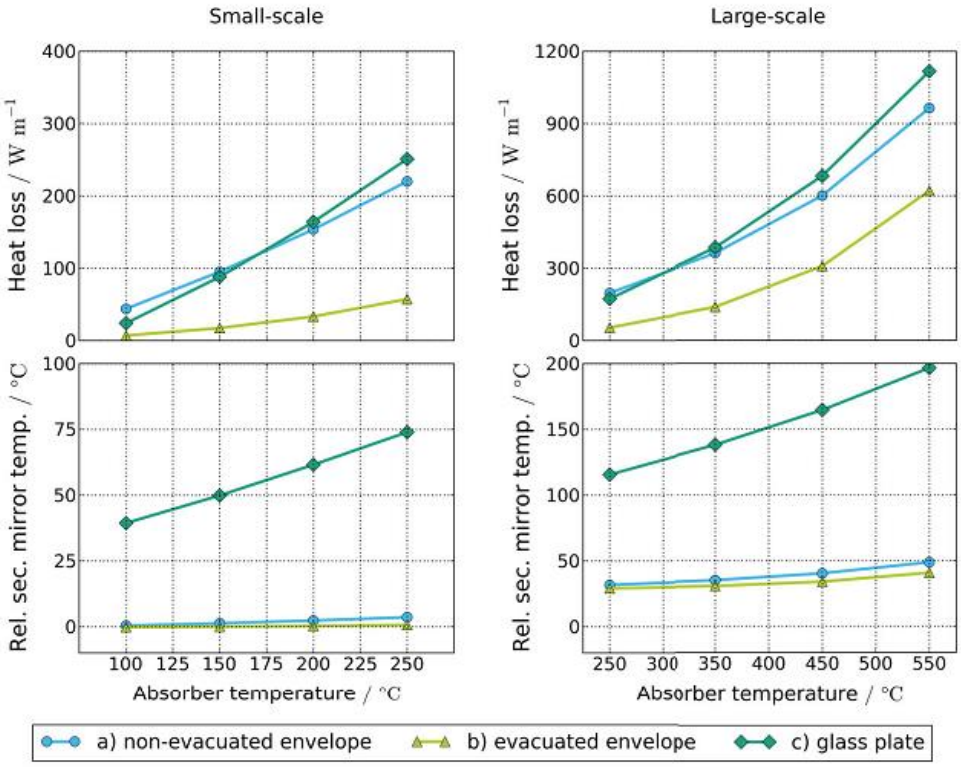

Figure 2.2 Heat loss and secondary reflector temperature for large and small scale temperature range [40].

Qiu et al. [41] developed a model for performance analysis of an LF with receiver comprising evacuated tube and compound parabolic reflector. The heat transfer fluid used in the model was molten salt. First, optical efficiency was obtained through Monte Carlo ray tracing code and was then coupled with finite volume method to evaluate thermal performance. The peak optical efficiency was found to be 65% and collector efficiencies for all conditions were more than 46%. The flux and temperature distribution on absorber had similar profile and it was recommended to design mirrors with appropriate slope deviation for more uniform distribution. Along with this, it was observed that large tracking errors may lead to formation of local hot spots.

A small sized LF was studied by Mokhtar et al. [12]. The collector, located in Blinda (Algeria), was made up of reflective mirror strips and trapezoidal cavity receiver and was used for heating tap water. The study was conducted both theoretically and

experimentally. The theoretical model was based on energy balance and finite difference method. Results from both numerical and experimental analysis showed good agreement and thermal efficiency of collector was slightly above 29%.

2.3. Objective of Current Work

The present work emphasizes on modelling of a medium size (6-15 mirror rows) linear Fresnel collector for an industrial process. A similar procedure can be followed to design CST system of any type or size at any location. The main purpose is to quantify the effects of design parameters such as height of receiver, width of mirrors and collector, gap between mirror rows and mirror profile. Thereupon selecting the appropriate configuration and determining the thermal performance.

The collector model is based on previously discussed works, however, in this thesis; the results obtained from comprehensive optical and thermal analysis are coupled to design a custom-built LF system for SHIP unlike the researches presented in the literature where main focus is on either optical or thermal performance of a commercially available collector.

Furthermore, literature lacks the information on how and why a specific LF design was selected for the study. Additionally, almost all the studies are performed on either trapezoidal cavity or non-evacuated receiver, however, in the current study, an evacuated tube absorber with compound parabolic reflector is considered and the design of secondary reflector is discussed in detail. In addition to receiver's design, the flux distribution on absorber for varying position of sun is also presented, which has not been done in the literature.

Furthermore, the factory considered in this study is located in Konya, which is a major industrial city in the Central Anatolia region of Turkey with sufficient solar resource. That being said, in Turkey, SHIP is still in its infancy along with LF technology, for instance, the first LF based process heat generation system in Turkey was installed in 2012 and is still the only working LF system for industrial use in the country.

Therefore, the summary of main objectives of this thesis is as follows:

- Develop a mathematical model to determine the optical and energetic performance of an LF and perform parametric studies in order to quantify the influence of key design parameters on collector's efficiency.
- Use the model to design an LF for a SHIP in Turkey based on simulations and predict system's output for varying weather conditions.

2.4. Thesis Organization

In this thesis, a numerical investigation of linear Fresnel collector is performed and an LF for industrial process is designed. Therefore, to provide context for this work, Chapter 1 is an overview of LF technology (Section 1.1) and SHIP (Section 1.2 to Section 1.4). Finally, in Section 1.5, feasibility of LF for SHIP is explored with illustrations of both experimental and industrial set-ups.

Next, in Chapter 2, a detailed literature review of optical (Section 2.1) and thermal (Section 2.2) analysis is presented along with thesis objectives and organization.

In Chapter 3, first optical model is considered as it is essential for LF field sizing and calculation of IAM which is required in thermal model. Optical efficiency is defined in Section 3.1 and then influence of collector design parameters on optical performance (Section 3.1.1 to 3.1.7). Later ray tracing method is discussed which is used for parametric analysis. After covering major points related to optical side of LF, thermal model is explained in Section 3.2 in two steps: calculation of receiver surface temperatures (Section 3.2.1) and then outlet temperature and total energy gain (Section 3.2.2). Furthermore, in Section 3.3, industrial process, requirements and collector location in the factory is described.

In Chapter 4, the results obtained through models described previously are presented. In order to validate the models, both optical and thermal models are benchmarked with published data in Section 4.1.

After validation, from Section 4.2.1 to 4.2.5, parametric study is performed by varying key design features of an LF. Next, flux distribution on absorber tube for varying solar altitude is studied in Section 4.3. The purpose of this section is to find out how well primary mirror field and secondary reflector are working in conjunction. The basic trends in key design parameters are used to specify LF field which is given in Section 4.4. In the end of Section 4.4, a summary of LF design specification is presented in Section 4.4.3 in form of a table for quick access to key features of the collector. After the LF design is complete, next step is to predict daily and monthly performance of the system but before that, it is necessary to find IAM of the designed collector which is done in Section 4.5. The IAM values are then used to calculate total radiation absorbed and eventually receiver surface temperatures and heat losses (Section 4.6).

Thermal analysis is then further extended to find out daily and monthly energetic performance of the designed LF. Temperature outputs during specific days and total monthly energy yield along with thermal efficiency are illustrated in Section 4.7. Conclusions and recommendations resulting from this work are summarized in Chapter 5

CHAPTER 3

MODEL DESCRIPTION

The topics covered in this chapter include descriptions of, first, optical model followed by thermal model and finally industrial process with factory requirements.

3.1. Optical Model

The primary objective of the optical analysis is to determine solar rays which are reflected from mirrors and intercepted by the receiver at any sun position. The ratio of solar energy absorbed by the receiver and solar energy that impinges on the reflectors is the optical efficiency and for a LF, it depends on sun's position, focal length of primary mirrors, height of the absorber above the primary mirror plane, width of primary mirror strips, latitude of location, gap between the mirror strips and number of parallel mirror rows. The optical efficiency at a given solar altitude and solar azimuth is determined using Equations (3.1), (3.2) and (3.3) as shown below.

$$P_{abs} = N_{Ph} \times P_{Ph} \quad (3.1)$$

$$P_{Ap} = DNI \times A_P \quad (3.2)$$

$$\eta_{opt} = \frac{P_{abs}}{P_{Ap}} \quad (3.3)$$

Where

P_{abs} is the power incident on the absorber tube (W)

N_{Ph} is the number of photons impinging on the receiver (-)

P_{Ph} is the power of each photon calculated using ray tracing (W)

DNI is direct normal irradiance (W m^{-2})

A_p is the aperture area of the collector (m^2)

η_{opt} is the optical efficiency (-)

3.1.1. Incidence Angle Modifier (IAM)

A collector attains peak optical efficiency in case of normal incidence and there is decline in optical performance at off-normal incidence due to dependence of optical properties of the collector on direction of incident sun rays. So IAM is used to correct the collector's performance at normal incidence to off normal directions [42]. The IAM is calculated using Equation (3.4),

$$\text{IAM} = \frac{\alpha\tau\rho_R\rho_{SR}}{(\alpha\tau\rho_R\rho_{SR})_n} \tag{3.4}$$

Where $\alpha\tau\rho_R\rho_{SR}$ and $(\alpha\tau\rho_R\rho_{SR})_n$ are product of absorptivity of absorber tube, transmittance of glass cover, reflectivity of primary mirrors and reflectivity of secondary reflector at a given angle of incidence and at normal incidence respectively. This product is found using Equation (3.5) and defined as ratio of number of photons absorbed by receiver to number of photons directly incident upon aperture plane [42].

$$(\alpha\tau\rho_R\rho_{SR}) = \frac{\sum n_{receiver}}{\sum n_{aperture}} \tag{3.5}$$

In case of LF, biaxial IAM is required, that is, one for transversal incidence angle (ϕ_T) and other for longitudinal (ϕ_L) as shown in Figure 3.1.

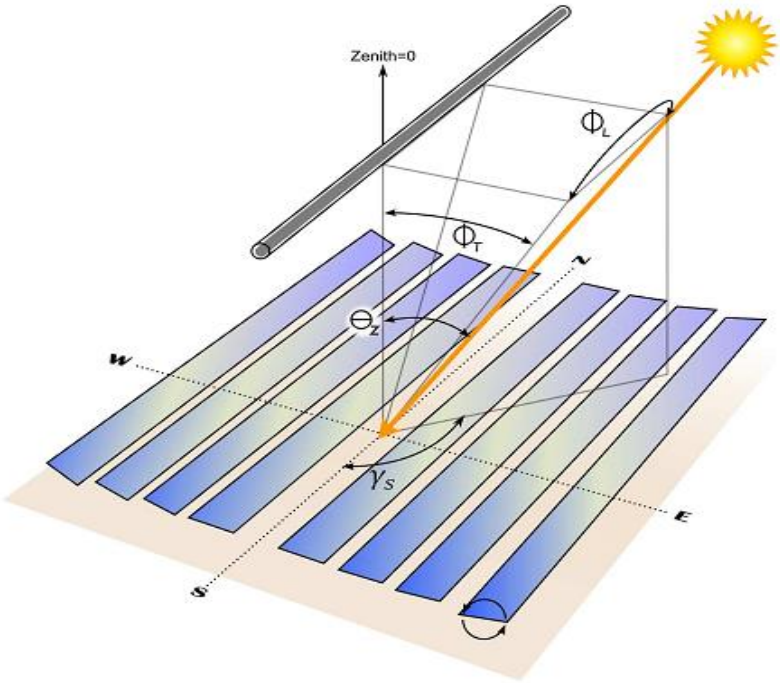

Figure 3.1 Transversal and longitudinal incidence angle for LF [43].

The relation between ϕ_T, solar azimuth (γ_s) and solar altitude (α_s) for North-South orientation is shown in Equation (3.6) and for ϕ_L by Equation (3.7) [43].

$$\tan(\phi_T) = \frac{\sin(\gamma_s)}{\tan(\alpha_s)} \tag{3.6}$$

$$\tan(\phi_L) = \cos(\gamma_s) \times \cos(\alpha_s) \tag{3.7}$$

$$\text{and } \alpha_s = 90° - \theta_z$$

Where θz is the solar zenith angle

The IAM is determined by taking product of two components [1] as shown in Equation (3.8).

$$\text{IAM}(\phi_L, \phi_T) = \text{IAM}(\phi_L, 0) \times \text{IAM}(0, \phi_T) \tag{3.8}$$

3.1.2. Mirror Inclination

LF is equipped with single axis tracking system and it changes the inclination of mirrors throughout the day. The inclination angle (ϕ_i) depend on position of sun, height of receiver (h) and position of the mirrors relative to central axis (d_i) and is found by means of Equation (3.9) and Equation (3.10) and using geometries shown in Figure 3.2 and Figure 3.3 [44].

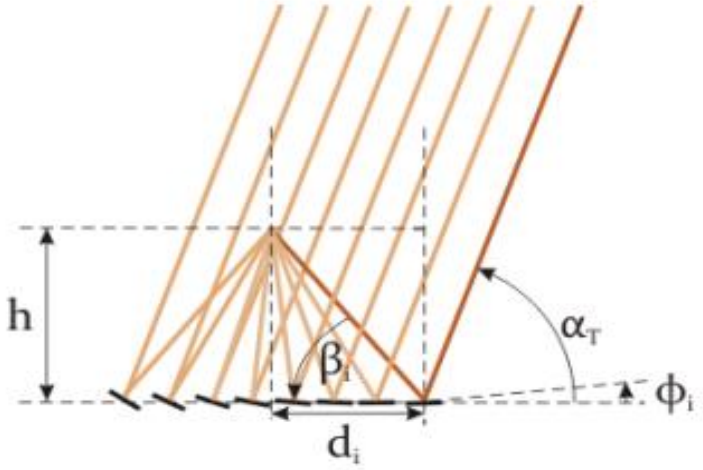

Figure 3.2 Inclination of facets [44].

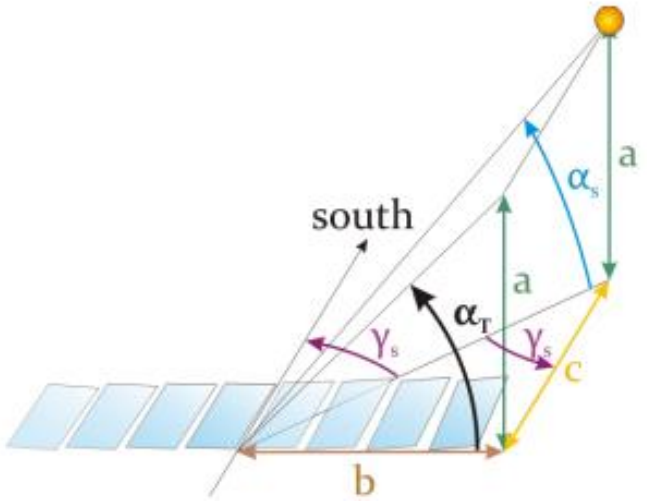

Figure 3.3 Transversal solar altitude angle for N-S orientation [44].

$$\phi_i = \frac{\alpha_T - \beta_i}{2} \tag{3.9}$$

$$\tan(\phi_T) = \tan^{-1}\left(\frac{h}{d_i}\right) \tag{3.10}$$

Where α_T is the transversal solar altitude angle which is determined using Equation (3.11) and Equation (3.12) for North-South (N-S) orientation.

$$\tan(\alpha_T) = \frac{\tan(\alpha_s)}{\sin(\gamma_s)} \tag{3.11}$$

$$0° \leq \alpha_T \leq 180° \text{ and } \alpha_T = 90° \text{ at } \sin(\gamma_s) = 0 \tag{3.12}$$

On differentiating Equation (3.9) with respect to time, we get:

$$\frac{d\phi_i}{dt} = \frac{1}{2}\frac{(d\alpha_T)}{dt} \tag{3.13}$$

According to Equation (3.13), the rate of change of ϕ_i depends solely on sun's motion. Therefore, tracking for all primary mirrors can be achieved with a single motor with constant angular velocity. However, in practice, each primary mirror has its own tracking motor to increase tracking accuracy and ease of energy dumping.

3.1.3. Curvature of the primary mirrors

The focal length of primary reflectors is crucial for the optimum optical efficiency. The primary objective is to accumulate maximal radiation onto the absorber and if the profile is not designed properly, the flux incident on the receiver is attenuated. Thus, there is a favorable radius of curvature range that gives the foremost optical performance. A cheaper and less complicated alternative is using flat mirrors which is beneficial for small scale applications as plane mirrors can reduce the initial investment significantly, however, the collectors based on flat mirrors have considerably lower optical efficiency.

The improved performance of curved mirrors compared to flat mirrors is attributed to reduction in radiation spillage, that is, more of the reflected sun rays are able to reach the absorption pipe. Despite this, due to continuous movement of the sun over the day in both transverse and longitudinal direction, relative to mirror rows, focusing the sun rays onto a fixed focal line is unfeasible and a caustic is formed [44]. This phenomenon is shown in Figure 3.4(a) and 3.4(b).

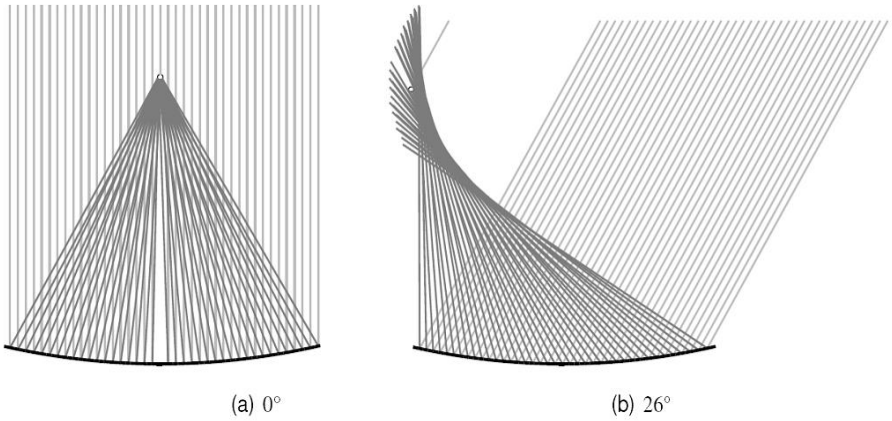

Figure 3.4 (a) Rays focused onto a fixed point in case of normal incidence (b) Caustic formation during off normal condition [44].

3.1.4. Height of Receiver

The LFs with high receivers have low optical efficiency because mirrors are unable to focus accurately and there are tracking errors. On the other hand, receiver situated very close to aperture plane leads to increment in blocking between the mirror rows and shading by both receiver and neighboring rows along with higher angle of incidence [44].

3.1.5. Width of Primary Mirrors

The use of too narrow or too wide primary reflectors can decrease the optical efficiency of the system significantly. If the number of parallel rows is kept constant

and narrower mirrors are used, there is loss of aperture area and hence less flux is incident on the receiver.

On the other hand, when collector width is not fixed, higher numbers of mirrors are needed to achieve required aperture area and therefore additional investment to cover more complicated frame and tracking. In case of wider mirrors, the parabolic trough behavior cannot be achieved effectively as wider mirrors suffer stronger astigmatic effects and tracking inaccuracy [44].

3.1.6. Gap between Primary Mirror Rows

Spacing between adjacent mirrors rows must be in such a way that it prevents shading and blocking without making collector unnecessarily wide. Excessive gap leads to larger land usage and decrease in contribution from outer mirror rows.

3.1.7. Slope Deviation

Reflector shape is a key design feature for optimal optical performance of a solar collector because an inaccurate shape causes deviation of reflected rays from target, that is, receiver. The reason for shape errors can be attributed to faulty production technique, collector orientation and mounting method.

The parameter used to define the optical quality of mirror is slope error which is the angle between real surface normal and ideal surface normal as shown in Figure 3.5.

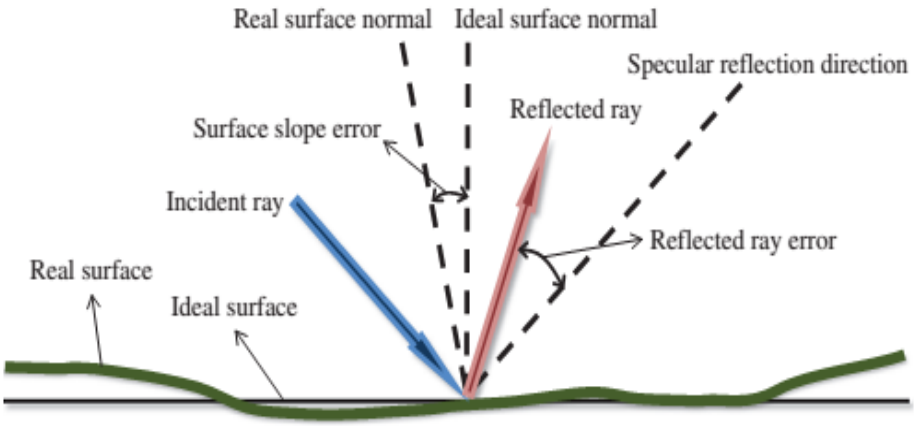

Figure 3.5 Slope errors causing reflected ray to deviate from specular reflection direction [45].

The slope deviation of the whole collector surface (σ slope) is calculated by taking sum of root mean square of the local slope deviation. There are three main methods to measure the mirror shape [46]:

- Laser Reflection Count
- High – Density Close – Range Photogrammetry
- Deflectometry (Fringe reflection)

The space frame and mounting points of a curved reflector are shown in Figure 3.6 and Figure 3.7 shows the surface error of EuroTrough.

Figure 3.6 Space frame and mirror mounting points of a concentrating collector [46].

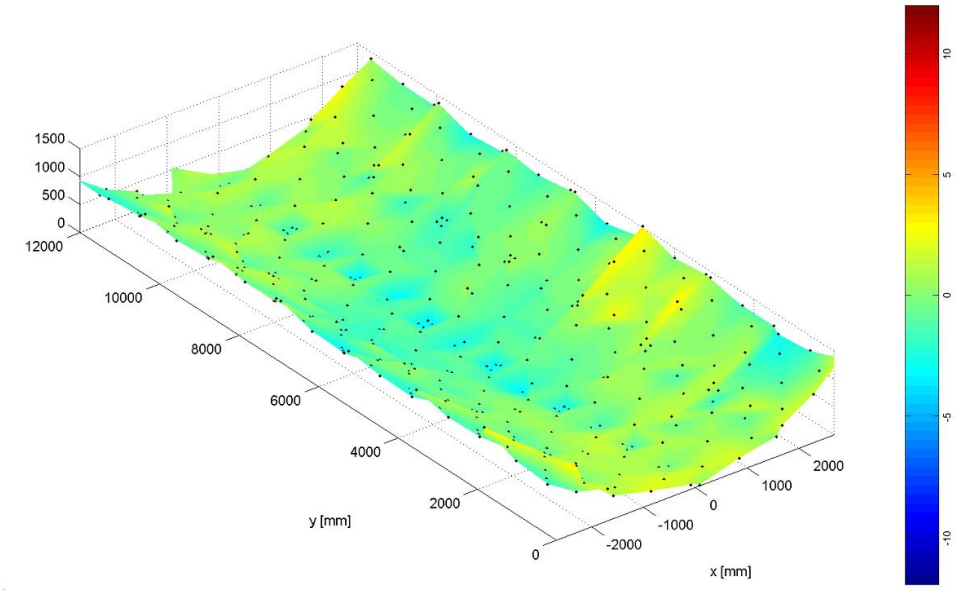

Figure 3.7 Three dimensional slope error of EuroTrough [46].

3.1.8. Ray Tracing

A common method to analyze the optical properties of concentrating solar collectors is ray tracing. This involves tracking path of large bundle of statistically random photons, emitted from a particular luminaire, from their points of emission to points of absorption. The distribution and intensity of rays are determined by finding points of intersection between receiver surface and reflected rays using vectors.

Most commercially available ray tracing programs employ Monte Carlo (MC) method in order to evaluate optical characteristics of a solar collector. The MC method solves a mathematical problem using statistical sampling technique and is well suited to solve relatively complex scenarios which are rather difficult to handle by conventional numerical technique. Therefore, in order to determine the effect of LF field parameters on its optical performance, ray tracing program 'Tonatiuh' [47] is used in this study. A sample ray tracing in Tonatiuh is shown in Figure 3.8.

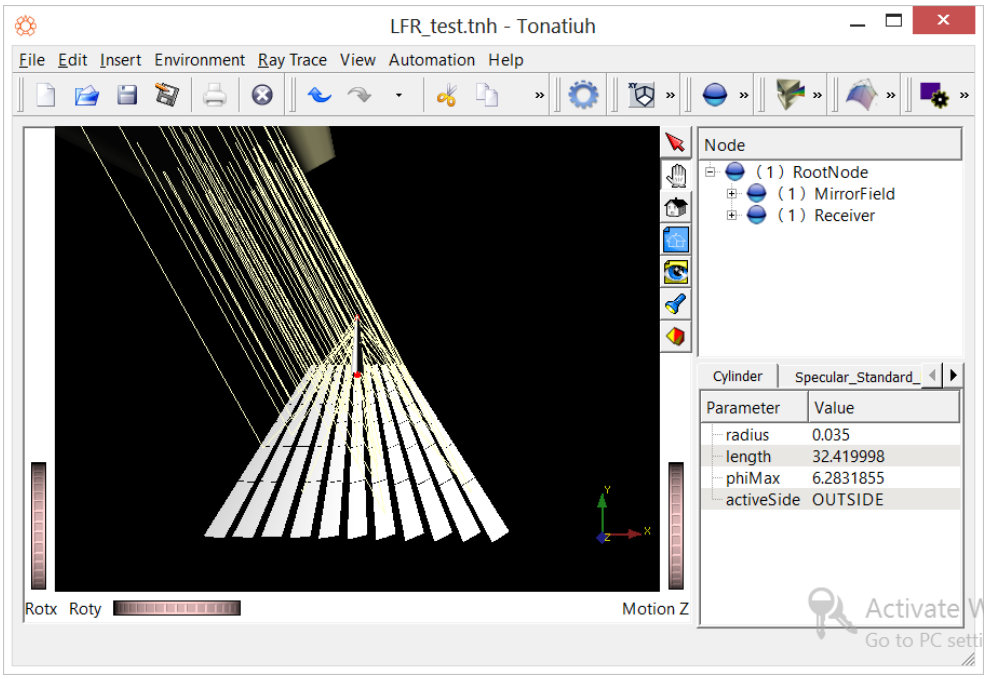

Figure 3.8 LF model and ray tracing in Tonatiuh.

3.2. Thermal Model

The thermal performance of the linear Fresnel collector is determined using a one dimensional steady state heat transfer model and uniform flux distribution on the absorber tube. In order to calculate the receiver heat loss, outlet heat transfer fluid temperature, heat gain and collector efficiency, the required inputs are absorber geometry, optical properties, HTF properties, DNI, wind speed, ambient and sky temperature.

3.2.1. Surface Temperatures and Receiver Heat Loss

Due to absorption of heat by the receiver, its temperature rises and this leads to a temperature difference between absorber tube and surrounding. Consequently the receiver loses heat through conduction, convection and radiation as shown in Figure 3.9.

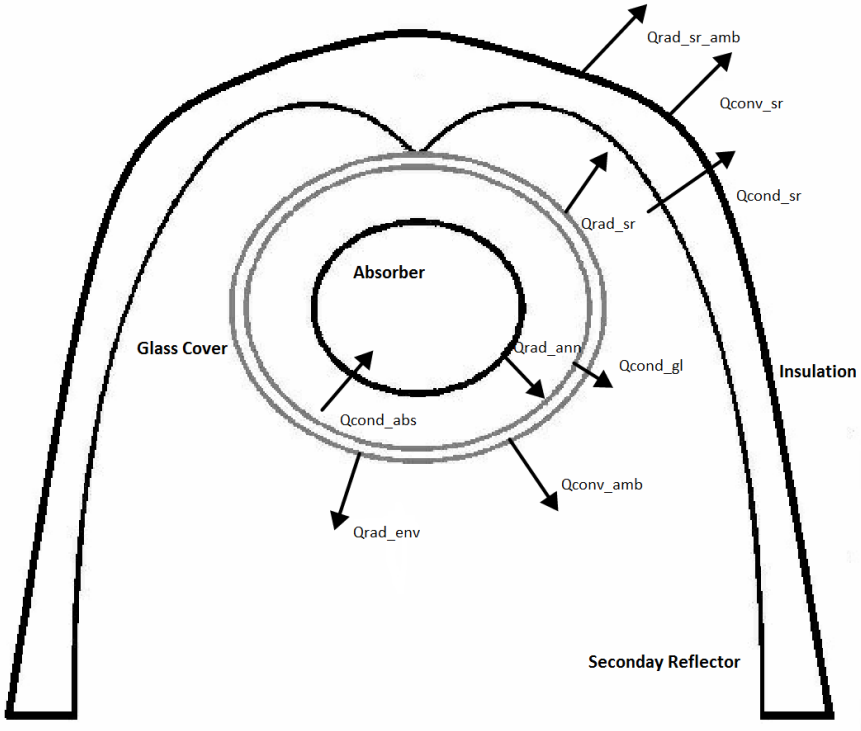

Figure 3.9 One dimensional heat transfer model.

The temperature of different receiver surfaces is calculated by forming one dimensional heat transfer equations through energy balance and solving them simultaneously. All the heat exchanges occurring in the receiver, as illustrated in Figure 11, are described as follows,

Solar radiation absorbed by receiver tube in W m^{-1} [48],

$$Q_{sol\_abs} = I_b A_w \eta_{opt} IAM \tag{3.14}$$

Where

I_b is direct normal irradiance (W m^{-2})

IAM is incidence angle modifier (-)

A_w is collector's aperture width (m)

η_{opt} is the optical efficiency (-)

Convective heat transfer between inner surface of absorber tube and heat transfer fluid in W m^{-1},

$$Q_{conv\_HTF} = h_{HTF}(2\pi r_{abs,i})(T_{abs,i} - T_{HTF}) \tag{3.15}$$

Where

h_{HTF} is convective heat transfer coefficient (W m^{-2} K^{-1})

$r_{abs,i}$ is absorber inner surface radius (m)

$T_{abs,i}$ is average temperature of absorber's inner surface (°C)

T_{HTF} is temperature of heat transfer fluid (°C)

Heat conduction from outer absorber surface to inner absorber surface in W m^{-1} [49],

$$Q_{cond\_abs} = \frac{(2\pi k_{abs})(T_{abs,o} - T_{abs,i})}{\ln\left(\frac{r_{abs,o}}{r_{abs,i}}\right)} \tag{3.16}$$

Where

k_{abs} is thermal conductivity of absorber tube material (W m^{-2} K^{-1})

$r_{abs,o}$ is absorber outer surface radius (m)

$T_{abs,o}$ is average temperature of absorber's outer surface (°C)

Heat exchange through radiation between outer surface of absorber and inner glass cover surface in W m^{-1} [48]

$$Q_{rad\_ann} = \frac{\sigma(2\pi r_{abs,o})(T_{abs,o}^4 - T_{g,i}^4)}{\frac{1}{\varepsilon_{abs}} + \left(\frac{1-\varepsilon_g}{\varepsilon_g}\right)\left(\frac{r_{abs,o}}{r_{g,i}}\right)} \quad (3.17)$$

Where

σ is the Stefan-Boltzmann constant, 5.67E-8 (W m^{-2} K^{-4})

ε_{abs} is emittance of absorber tube's outer surface (-)

ε_g is emittance of inner glass cover surface (-)

r_g,i is glass cover outer surface radius (m)

$T_{g,i}$ is average temperature of glass cover's outer surface (K)

Conductive heat transfer from inner glass surface to outer glass surface in W m^{-1},

$$Q_{cond\_gl} = \frac{(2\pi k_g)(T_{g,i} - T_{g,o})}{\ln\left(\frac{r_{g,o}}{r_{g,i}}\right)} \quad (3.18)$$

Where

k_g is thermal conductivity of glass cover (W m^{-2} K^{-1})

$r_{g,o}$ is glass cover outer surface radius (m)

$T_{g,o}$ is average temperature of glass cover's outer surface (°C)

Radiation heat transfer between glass cover and environment in W m^{-1} [10],

$$Q_{rad\_env} = \frac{\sigma(2\pi r_{g,o})(T_{g,o}^4 - T_{env}^4)}{\left(\frac{1+\varepsilon_g}{\varepsilon_g}\right)} \quad (3.19)$$

Where

$T_{g,o}$ average temperature of glass cover's outer surface (K)

Solar radiation absorbed by the glass envelope in W m^{-1} [33],

$$Q_{rad\_absorbed} = Q_{sol_{abs}}\left(\frac{\alpha_g}{\alpha_{abs}\tau_g}\right) \quad (3.20)$$

α_{abs} is absorptivity of receiver tube (-)

α_g is absorptivity of glass cover (-)

τ_g is transmittance of glass cover (-)

Heat transfer through convection to ambient through outer surface of glass cover in W m^{-1} [33],

$$Q_{conv\_amb} = h_{w,g}(2\pi r_{g,o})(T_{g,o} - T_{amb}) \quad (3.21)$$

Where

$h_{w,g}$ is convective heat transfer coefficient for glass cover to wind (W m^{-2} K^{-1})

T_{amb} is temperature of ambient air (°C)

Heat exchange from outer surface of glass cover to inner secondary reflector surface by radiation in W m^{-1} [10],

$$Q_{rad\_sr} = \frac{\sigma(T_{g,o}^4 - T_{sr,i}^4)}{\left(\frac{1-\varepsilon_{sr}}{A_{sr}\varepsilon_{sr}}\right) + \left(\frac{1-\varepsilon_g}{A_g\varepsilon_g}\right) + \left(\frac{2}{A_g}\right)} \quad (3.22)$$

Where

ε_{sr} is emittance of secondary reflector's outer surface (-)

ε_{g} is emittance of inner glass cover surface (-)

A_g is outer surface area of glass cover per unit length (m)

A_{sr} is inner surface area of secondary reflector per unit length (m)

$T_{sr,i}$ is average temperature of secondary reflector's inner surface (K)

Conductive heat transfer between secondary reflector's inner surface and outer surface in W m^{-1},

$$Q_{cond\_sr} = \frac{(2\pi k_{ins})(T_{sr,i} - T_{sr,o})}{\ln\left(\frac{r_{sr,o}}{r_{sr,i}}\right)} \quad (3.23)$$

Where

k_{ins} is thermal conductivity of secondary reflector insulation (W m^{-2} K^{-1})

$r_{sr,o}$ is secondary reflector outer surface radius (m)

$r_{sr,i}$ is secondary reflector inner surface radius (m)

$T_{sr,o}$ is average temperature of secondary reflector's outer surface (°C)

Heat transfer to ambient air from outer surface of secondary reflector in W m^{-1},

$$Q_{conv\_sr} = h_{w,sr}(2\pi r_{sr,o})(T_{sr,o} - T_{amb}) \quad (3.24)$$

Where

$h_{w,sr}$ is convective heat transfer coefficient for secondary reflector outer surface to wind (W m^{-2} K^{-1})

Radiative exchange between outer secondary reflector surface and sky in W m^{-1},

$$Q_{rad\_sr\_amb} = \sigma\varepsilon_{sr}(2\pi r_{sr,o})(T_{g,o}^4 - T_{sky}^4) \quad (3.25)$$

Energy balance at steady state,

$$Q_{conv\_HTF} = Q_{cond\_abs} \quad (3.26)$$

$$Q_{sol\_abs} = Q_{cond\_abs} + Q_{rad\_ann} \quad (3.27)$$

$$Q_{rad\_ann} = Q_{cond\_gl} \quad (3.26)$$

$$Q_{cond\_gl} + Q_{rad\_absorbed} = Q_{rad\_env} + Q_{conv\_amb} + Q_{rad\_sr} \quad (3.27)$$

$$Q_{rad\_sr} = Q_{cond\_sr} \quad (3.28)$$

$$Q_{cond\_sr} = Q_{conv\_sr} + Q_{rad\_sr\_amb} \quad (3.26)$$

The radiation exchange across the annulus (Q_{rad_ann}) is the heat loss from the absorber tube. In case of non-evacuated tube, the heat loss is through convection and radiation heat transfer to the surrounding besides if there is gas seepage in the annulus because of heat transfer fluid, again heat will be lost as a result of both convection and radiation.

3.2.2. Outlet Temperature and Total Energy Gain

In order to calculate the collector outlet temperature, the absorber tube is partitioned into equal length sections as depicted in Figure 3.10. The output temperature from one section is the input temperature of successive section.

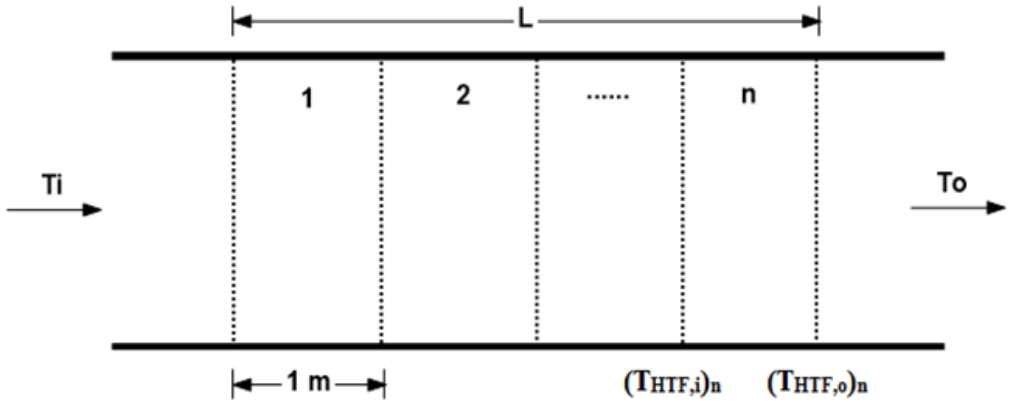

Figure 3.10 Division of absorber tube into longitudinal sections of equal length.

The average heat transfer fluid temperature per unit length in °C is given as,

$$T_{HTF} = \frac{T_{HTF,i} + T_{HTF,o}}{2} \tag{3.27}$$

Where

$T_{HTF,i}$ is HTF inlet temperature in the absorber tube section of unit length (°C)

$T_{HTF,o}$ is HTF outlet temperature in the absorber tube section of unit length (°C)

Useful energy gain by the heat transfer fluid in the absorber tube section of unit length in W m^{-1},

$$Q_u = \dot{m}c_{HTF}(T_{HTF,o} - T_{HTF,i}) \tag{3.28}$$

Where

$\dot{m}$ is mass flow rate of HTF (kg s^{-1})

c_{HTF} is specific heat capacity of HTF (J kg^{-1} K^{-1})

Additionally,

$$Q_u = Q_{conv\_HTF} \tag{3.29}$$

Temperature (in °C) at the exit of the an absorber tube of length 'L' is calculated as,

$$T_o = T_i + \frac{Q_u L}{\dot{m}c_{HTF}} \tag{3.30}$$

Where T_i is the temperature at the inlet of the receiver tube (°C)

The total energy absorbed by the HTF after leaving the absorber in W,

$$Q_{u\_tot} = \dot{m}c_{HTF}(T_o - T_i) \tag{3.31}$$

Furthermore, the thermal efficiency of the collector,

$$\eta_{th} = \frac{Q_{u\_tot}}{I_b A_p} \tag{3.32}$$

3.3. Description of Industrial Process and Requirements

The industry considered is Algida ice cream factory of Unilever in Konya (37°52' N 32°29'E) [50]. The solar field is required to heat up water, from 45°C to 100°C, which is used in Algida's production unit. The nominal power output from solar field is 92 kW_{th}.

A plate heat exchanger (80% efficiency) is used to transfer heat from heat transfer fluid (HTF), Therminol VP-1, to water. The solar field inlet and outlet temperature are 120°C and 160°C respectively. The flow rate of water is 0.325 kg s^{-1} whereas the maximum HTF flow rate is 1.23 kg s^{-1} and minimum HTF flow rate is 0.804 kg s^{-1} to maintain turbulent flow in the absorber tube. The schematic of the industrial process described previously is shown in Figure 3.11.

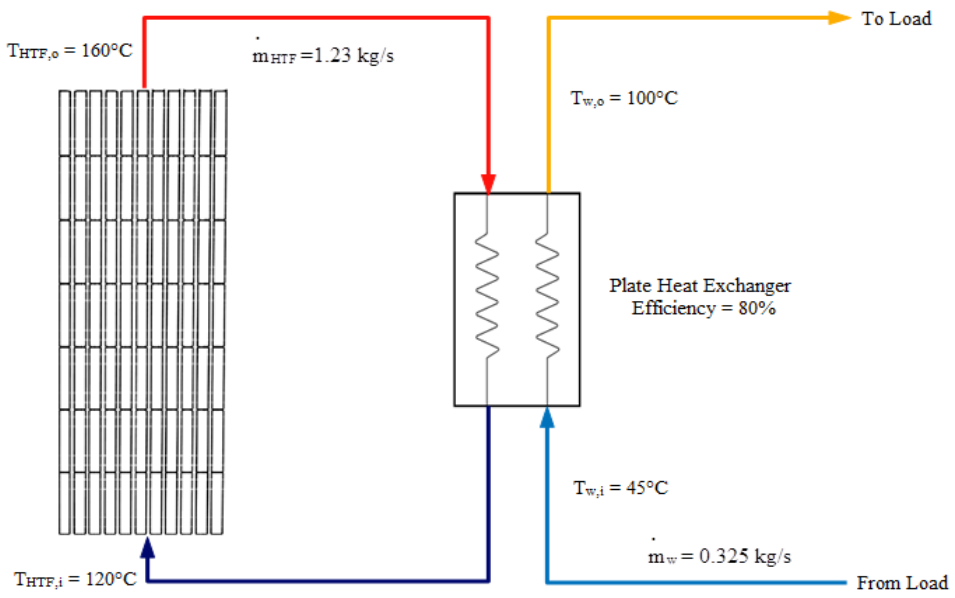

Figure 3.11 Input and output for the industrial process.

The collectors are oriented along North-South axis (tracking in East-West plane about horizontal North-South axis) in the area allotted by Unilever. The dimension of the area assigned is presented in Figure 3.12. The solar field lies between natural gas pressure station and production mechanical building.

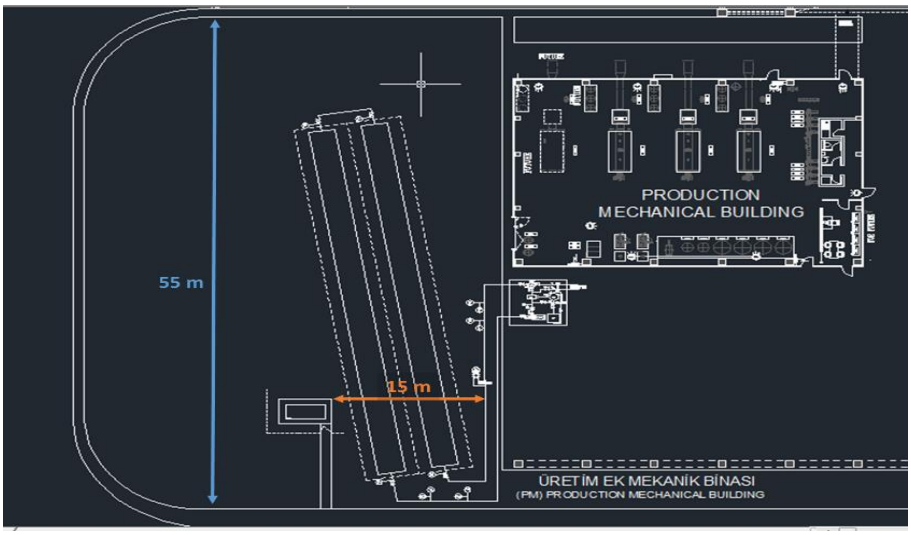

Figure 3.12 Collector location and orientation [50].

CHAPTER 4

RESULTS AND DISCUSSION

In this chapter, results obtained through optical and thermal model are discussed in detail. Validation of optical model and thermal model is done by comparing with experimental results which is the first subject of this chapter. Next, influence of key design parameters on optical efficiency is presented. In the final section, designed LF collector's daily energetic performance for varying weather conditions is described.

4.1. Model Validation

In order to validate the model, the results are compared with measured data presented in the literature with IAM model being validated in Section 4.1.1 and then mirror inclination in Section 4.1.2. After validation of optical model, in Section 4.1.3, thermal model is benchmarked with experimental results from literature.

4.1.1. Incidence Angle Modifier

A commercially available collector Industrial Solar LF-11 [14], specification given in Table 4.1, is selected for the validation of ray trace results. The commercial collector is modelled in Tonatiuh and optical performance is compared with the data given in the technical datasheet provided by the manufacturer.

Transversal and longitudinal IAM curves for LF-11 and results obtained from ray trace simulations are shown in Figure 4.1 and Figure 4.2 respectively.

Table 4.1 LF-11 Specifications [14].

Characteristic	**Value**	**Unit**
Number of mirror rows	11	-
Number of mirrors in each row	16	-
Total mirror area	352	m^2
Row spacing	0.2	m
Mirror profile	Curved	-
Height of primary reflectos above ground	0.5	m
Receiver type	Schott PTR	-
Receiver height above primary reflector plane	4	m
Total receiver tube length	65	m
Maximum operational wind speed	100	Km h^{-1}

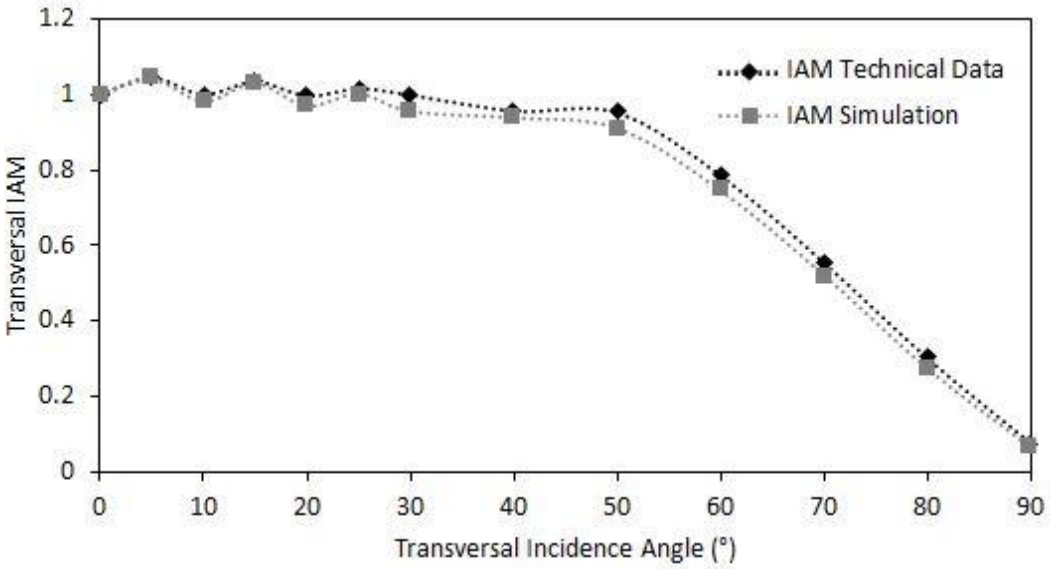

Figure 4.1 Transversal IAM for LF-11 from technical datasheet and ray trace simulation.

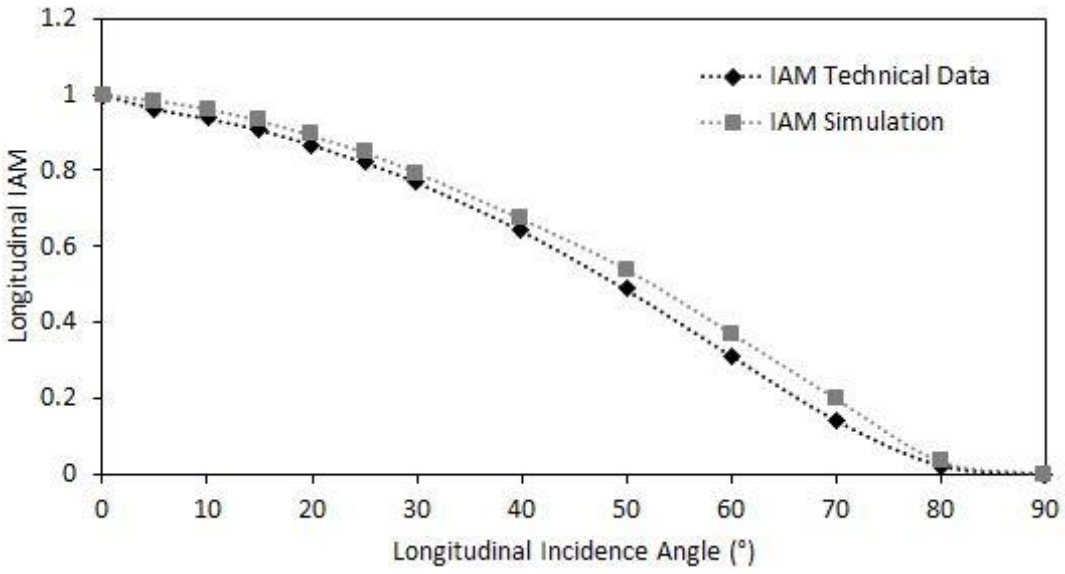

Figure 4.2 Longitudinal IAM for LF-11 from technical datasheet and ray trace simulation.

The IAM results in Figure 4.1 and Figure 4.2 show good agreement in the trends and slight differences can be attributed to the statistical error in Monte Carlo method. As depicted in Figure 4.1, the transversal IAM fluctuates between transversal incidence angle of 0° and 50° which is due to variation in optical properties of receiver, that is, reflectivity of secondary reflector, transmittance of glass cover and absorptivity of the absorber tube. On the other hand, longitudinal IAM decreases gradually from value of 1 to 0 from longitudinal incidence angle of 0° to 90° as shown in Figure 4.2.

4.1.2. Mirror Inclination

The inclination angle measured on 27th May 2009 at 13:00 local time in Seville (Spain) [10] for a linear Fresnel collector with 11 mirror rows and tilt angle obtained by simulation for the same collector are shown in Figure 4.3 and it is seen from that the angles predicted by ray trace and the measured data match well.

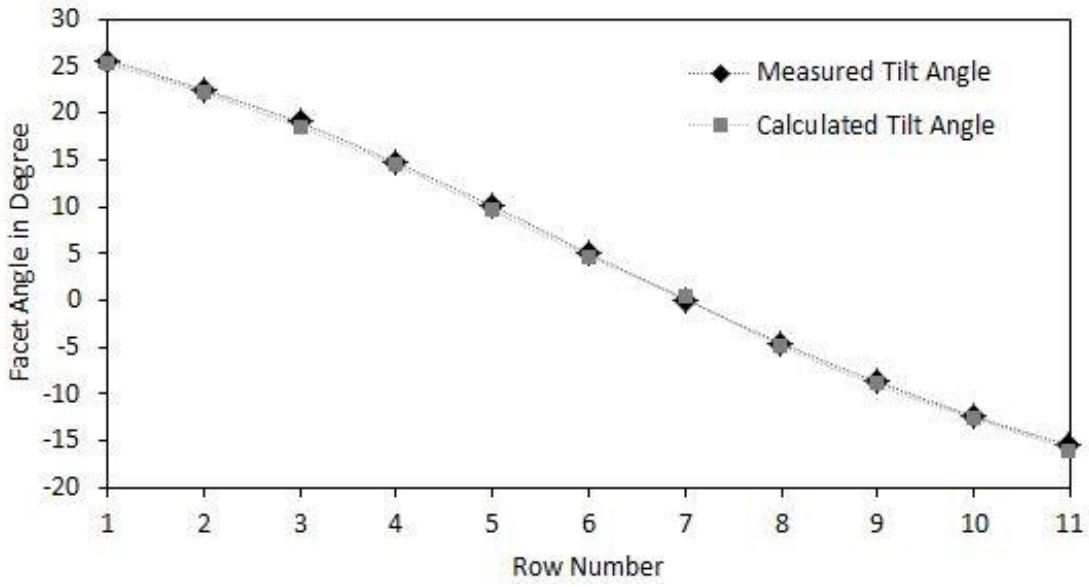

Figure 4.3 Comparison between measured data and simulation results of inclination angle (27 May 2009, Seville, Spain).

Furthermore, the variation in the tilt angle of mirror rows at zero degrees latitude for half day is presented in Table 4.2. The maximum tilt angle is achieved by outer most rows, that is, Row 1 during sunrise and Row 11 during sunset. However, the total movement of each mirror throughout the day is 90° which is half the angle covered by the sun, that is, 180° from 6 am to 6 pm. Furthermore, the change in inclination during an hour for each mirror row is 7.5° in anticlockwise direction – half of angular displacement of sun from east to west per hour. This half angular movement of reflectors is explained using Figure 4.4. Additionally, at the time of solar noon which is 12:07, the mirror inclination is symmetrical along the central axis. The middle row, Row 6, is horizontal with 0° tilt and the mirrors on left side of middle row are exactly like the respective mirrors on the right. The results are consistent with expectations.

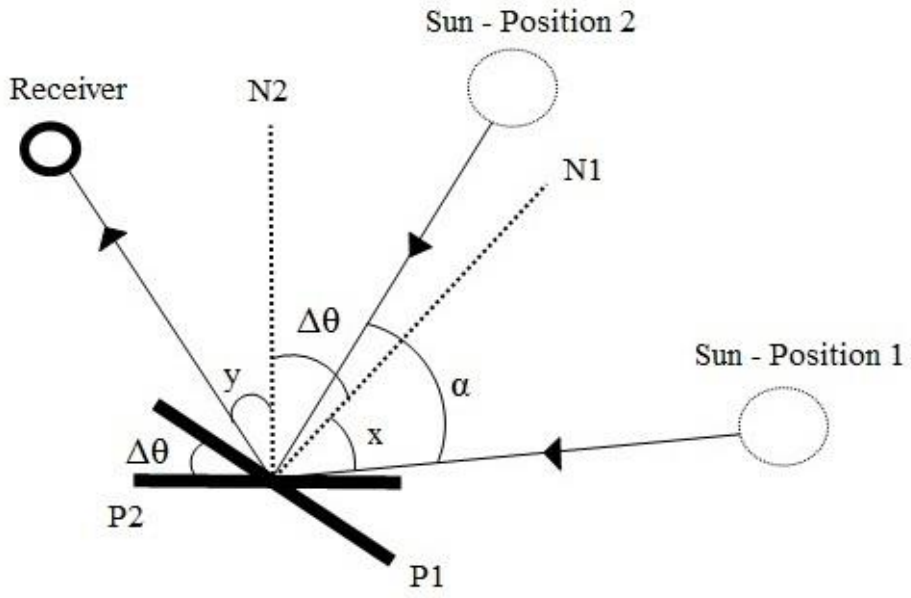

Figure 4.4 Relation between hour angle and mirror inclination.

From Figure 4.4,

$$\alpha - x = \Delta\theta - y \quad \text{and} \tag{4.1}$$

$$x = \Delta\theta + y \tag{4.2}$$

So

$$\alpha - \Delta\theta - y = \Delta\theta - y \tag{4.3}$$

$$\Delta\theta = \frac{\alpha}{2} \tag{4.4}$$

Hence, change in inclination of reflectors is half of angular movement of sun.

Table 4.2 Change in inclination of individual mirrors rows at 0° latitude (anticlockwise '+' and clockwise '–').

12.07	**12.00**	**11.00**	**10.00**	**9.00**	**8.00**	**7.00**	**6.00**	**Time**
-20.58	-21.44	-28.95	-36.46	-43.97	-51.48	-58.99	-66.50	**R1**
-17.48	-18.34	-25.85	-33.36	-40.87	-48.38	-55.89	-63.40	**R2**
-13.87	-14.73	-22.24	-29.75	-37.20	-44.71	-52.22	-59.73	**R3**
-9.63	-10.49	-18.00	-25.51	-33.02	-40.53	-48.04	-55.55	**R4**
-4.99	-5.85	-13.36	-20.81	-28.32	-35.83	-43.34	-50.85	**R5**
0.00	-0.86	-8.08	-15.88	-23.39	-30.90	-38.41	-45.92	**R6**
4.93	4.07	-3.38	-10.89	-18.40	-25.91	-33.42	-40.93	**R7**
9.63	8.77	1.26	-6.19	-13.70	-21.21	-28.72	-36.23	**R8**
13.82	12.96	5.45	-2.01	-9.52	-17.03	-24.54	-32.04	**R9**
17.48	16.62	9.11	1.61	-5.85	-13.36	-20.87	-28.38	**R10**
20.58	19.72	12.21	4.71	-2.75	-10.26	-17.77	-25.28	**R11**

4.1.3. Temperature Rise

The outlet temperature calculated from thermal model is compared with the measured output temperature given in literature [10] which is shown in Table 4.3. The heat transfer fluid used in the system is water and ΔT is difference between calculated outlet temperature ($Cal.T_{out}$) and measured outlet temperature ($Mea.T_{out}$).

Table 4.3 Comparison of outlet temperature with published data (27 May 2009, Seville, Spain).

Sol. Time	**Flow Rate** ($m^3 h^{-1}$)	**T_{amb}** (°C)	**Radiation** (kW)	**T_{in}** (°C)	**$Mea.T_{out}$** (°C)	**$Cal.T_{out}$** (°C)	**ΔT** (°C)
10:39	10.1	27.5	149.9	137.2	145.9	147.0	1.1
11:09	10.5	28.8	152.3	142.3	151.2	152.3	1.1
11:39	12.2	29.0	148.9	158.5	165.2	168.2	3.0
12:09	12.2	29.5	127.8	158.9	166.0	167.2	1.2
12:39	12.8	30.1	88.5	169.4	173.8	175.1	1.3
13:09	12.2	31.0	105.4	162.8	169.4	169.6	0.2

It is observed that the measured values and the temperature predictions from thermal model are in good agreement. The maximum difference between the calculated and measured temperature is 3°C at 11:39 solar time; on the other hand, the difference is less than 1.3°C for other times for the same day.

4.2. Solar Field Sizing

A medium size linear Fresnel collector with 11 mirror rows is modelled in Tonatiuh and analysis is done to determine the optimum range of collector parameters such as height of receiver, width of primary mirror and gap between the mirror rows. Optical efficiency is strictly based on geometry and parametric analysis in the following sections is done for normal incidence.

4.2.1. Focal Length of Primary Mirrors

The dependency of optical efficiency on mirror profile is given in Figure 4.5. The mirror profile is defined by ratio of focal length of individual mirrors (f_i) to the distance of respective mirrors from the receiver (D_i). The height of the receiver is taken as 4 m and the optical efficiency at f_i/D_i equals to unity is considered as reference for normalization. The value of 'D_i' is calculated using following equation,

$$D_i = \sqrt{h^2 + d_i^2} \tag{4.5}$$

Where 'h' is the height of the receiver from horizontal aperture plane and 'd_i' is the distance of individual mirrors from central axis.

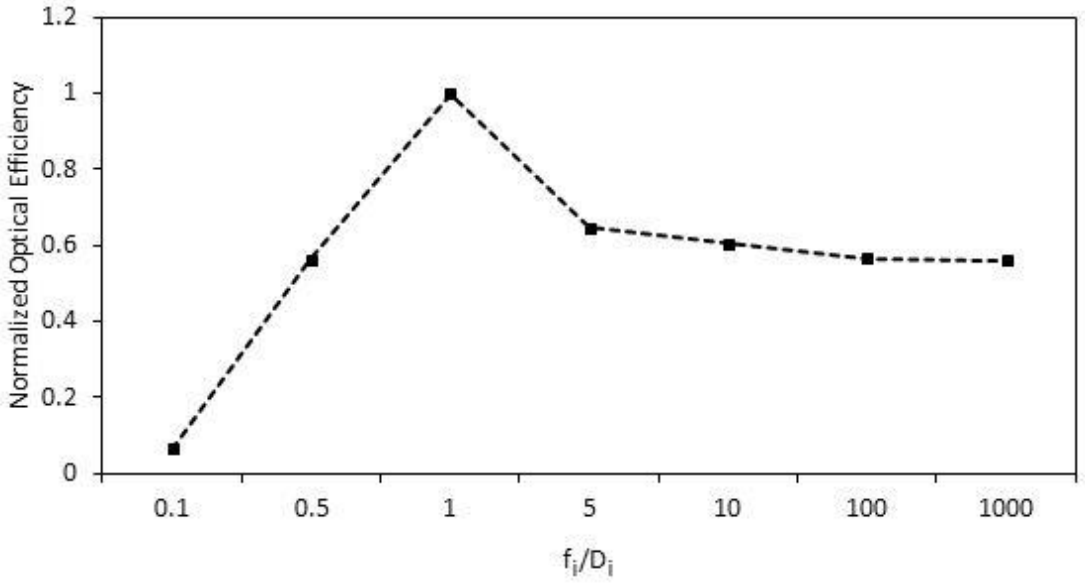

Figure 4.5 Normalized optical efficiency versus f_i/D_i.

According to simulation results shown in Figure 4.5, the peak optical efficiency is obtained when focal length of mirror (f_i) is same as its distance from the reception pipe (D_i). Furthermore, optical efficiency plummets when f_i/D_i ratio is below 1, however, after some decline between 1 and 10, optical performance remains unchanged beyond f_i/D_i = 10. Despite this, in reality optimal f_i/D_i value is found to be 1.1, instead of one, inability of primary reflectors to converge sun rays onto a fixed focal line [44].

4.2.2. Height of Receiver

The optical efficiency for different height at normal incidence is calculated, shown in Figure 4.6 and all the values have been normalized with respect to optical efficiency for 4 m receiver height.

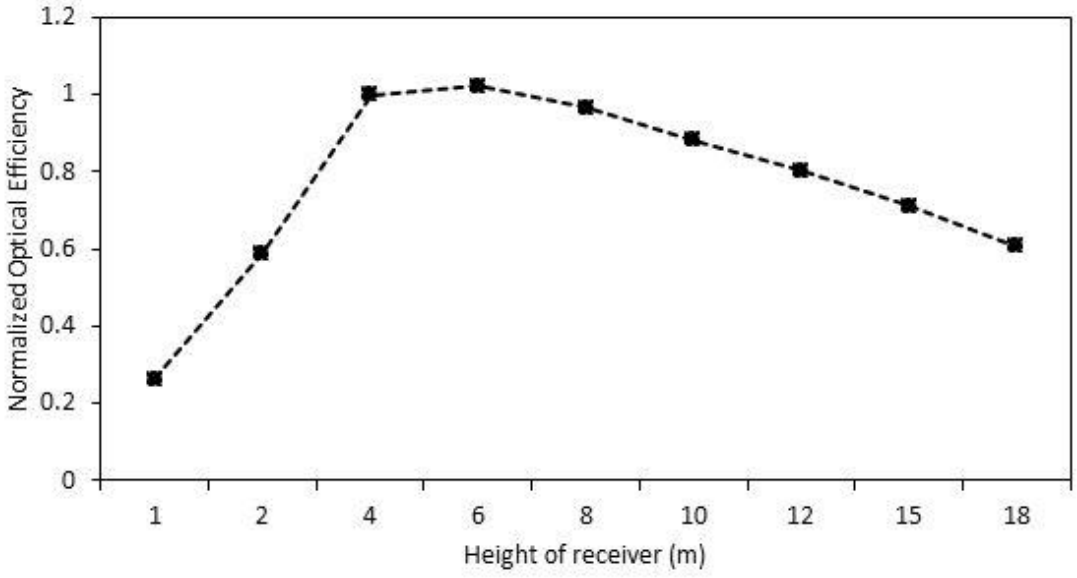

Figure 4.6 Normalized optical efficiency versus height of receiver.

According to Figure 14, the optimal height is between 4 m and 6 m and for values less than this range, the optical efficiency drops drastically due to accruement in shading, blocking and shadow cast by the receiver onto the primary reflectors. Furthermore, above 6 m, the optical performance falls gradually this is due to tracking inefficiency.

4.2.3. Width of Primary Reflectors

The change in optical efficiency of the collector with respect to width of the primary reflector at normal incidence is presented in Figure 4.7. All other parameters are kept constant, that is, receiver height is 4 m and mirror spacing is 0.2 m and optical efficiency is normalized using width of 0.5 m as base.

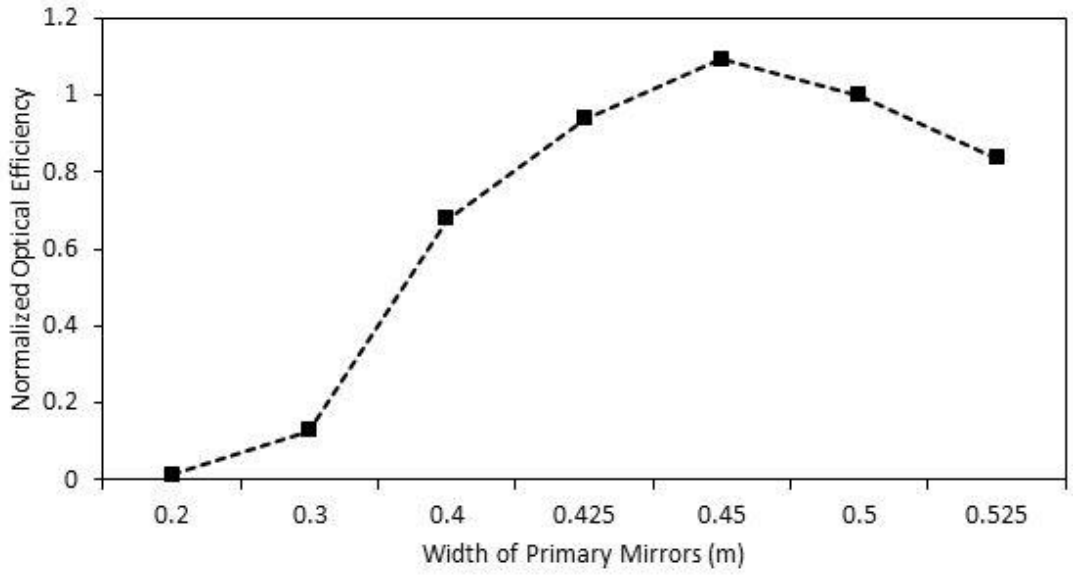

Figure 4.7 Normalized optical efficiency versus width of primary mirrors.

It is inferred from Figure 15 that there is a marked increase in the optical efficiency from mirror width of 0.2 m to 0.425 m and reaches peak value at mirror width of 0.45 m followed by a steady decline in case of wider mirrors. As mentioned earlier, low optical efficiency of narrow mirrors is due to less number of radiation incident on the receiver whereas wider mirrors are inaccurate in reflecting radiation onto the absorber and there is rise in shading and blocking among the adjacent mirrors. Hence, the ideal range for a medium size collector is between 0.425 m to 0.525 m with slight adjustments in the absorber height to attain maximum optical performance.

4.2.4. Spacing between Primary Reflector Rows

Analysis similar to height and width is done for gap between the adjacent mirror rows and value of 0.2 m is used for normalization of optical efficiency. The results from ray tracing are shown in Figure 4.8.

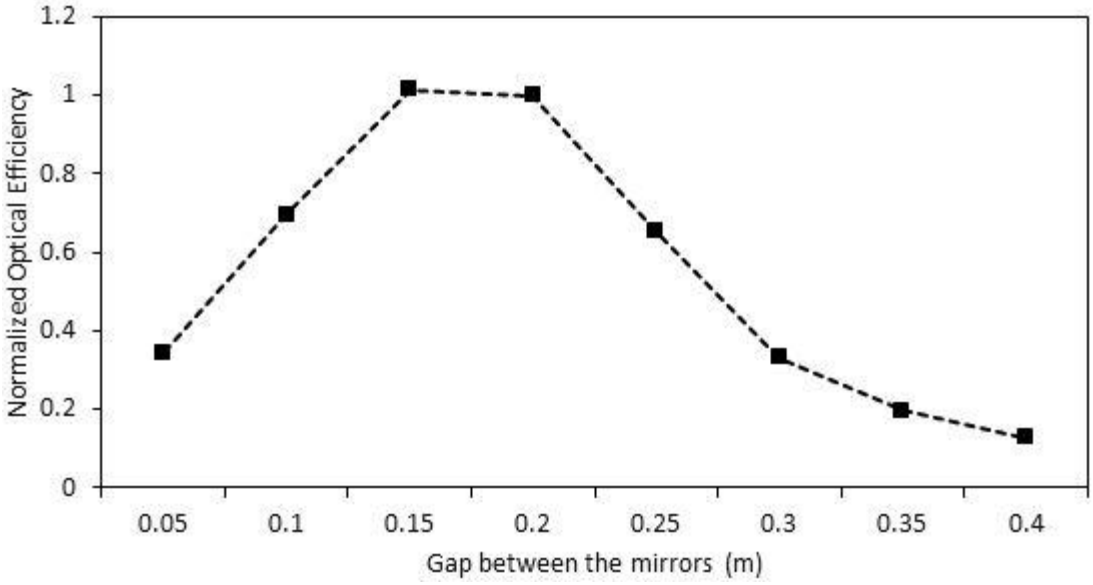

Figure 4.8 Normalized optical efficiency versus spacing between mirror rows.

As it is noted from Figure 4.8, there is a considerable upturn in optical efficiency from 0.05 m to 0.15 m where it reaches maximum and then levelled off. However, beyond 0.2 m, optical performance drops pronouncedly. When mirror rows are tightly packed, for instance gap between 0.05 m and 0.1 m, shading and blocking is prominent whereas when mirrors are wide apart, reflection inaccuracy leads to fall in optical efficiency. Consequently the most favorable spacing between mirrors is from 0.15 m to 0.2 m.

4.2.5. Slope Deviation

The relation between optical efficiency and slope deviation of primary mirrors for normal incidence is illustrated in Figure 4.9. The slope deviation of 4 mrad is used as a base for normalizing optical efficiency as 4 mrad is mid-range value.

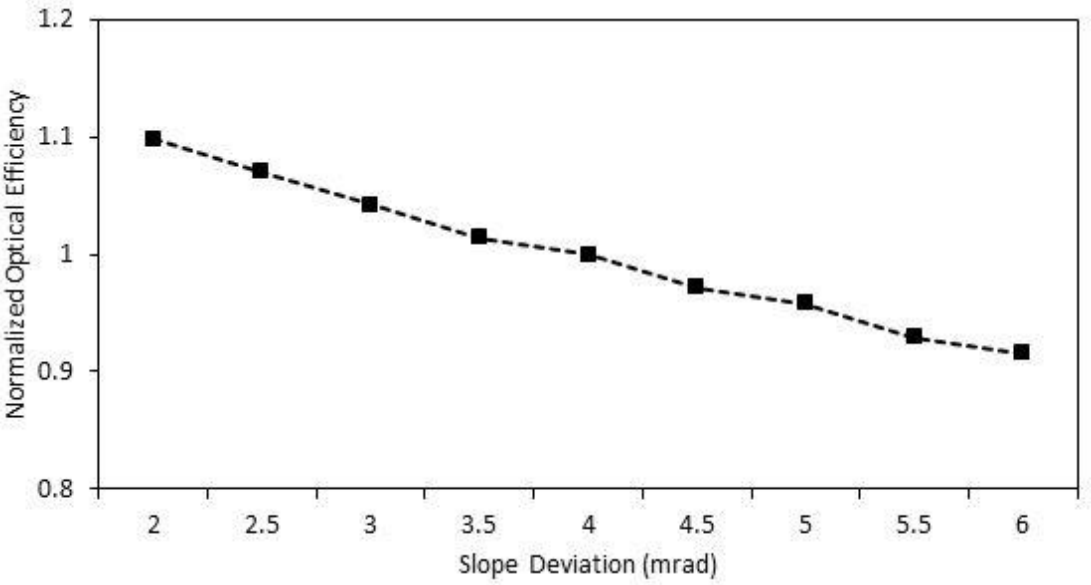

Figure 4.9 Normalized optical efficiency versus slope deviation.

A steady decline in optical performance is observed as the slope deviation or the mirror shape error increases and the drop in optical efficiency is approximately 16.5% between 2 mrad and 6 mrad. As expected mirrors with lowest shape errors are the most preferable choice from an efficiency perspective; nonetheless, selecting the mirrors with appropriate slope deviation depends on the financial resources as constructing a highly accurate mirror is both expensive and time consuming. In this study, a slope deviation of 4 mrad is considered based on assumed economic considerations.

4.3. Flux Distribution on Absorber Tube

The radiation reflected by primary mirrors is not distributed uniformly over the absorber tube surface; instead, the flux incident on the top of the tube is substantially lower than the flux on the side facing the primary reflectors. At normal incidence, for instance, the topmost part receives nearly 1% of the flux at the bottom. Furthermore, the dispersal of flux over the receiver varies significantly with change in angle of incidence.

The cylindrical geometry of tube of length 4 m is transformed into a two-dimensional rectangular plane, shown in Figure 4.10, in order to represent the distribution of flux on the absorber tube and Table 4.4 shows the angle and arc length of different positions on the absorber. The procedure for computing flux distribution is as follows: First of all the tube is divided into grids of specific area and then total power in each element is calculated by counting number of photons incident on each element and multiplying by power per photon, both of which are found using ray tracing. Afterward, flux distribution is determined by dividing total power in each element by area of the element.

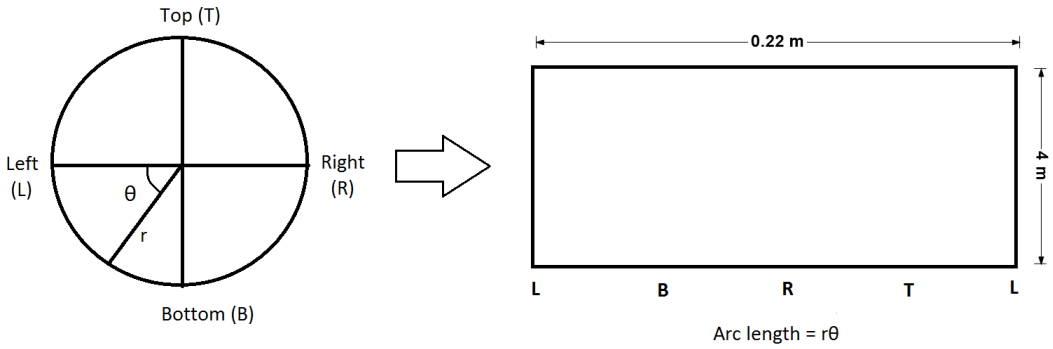

Figure 4.10 Position of points on tube of length 4 m and tube's two dimensional transformation.

Table 4.4 Value of position of points on the tube and rectangle.

Position	**Angle (θ)**	**Arc length**
Left (L)	0°	0
Bottom (B)	90°	0.055 m
Right (R)	180°	0.11 m
Top (T)	270°	0.165 m

4.3.1. Flux Distribution for Incidence Angle 0°

As expected, LF is seen to be most efficient in collecting solar radiation in case of normal incidence. Maximum flux and total power reach their highest value and all mirrors direct almost same number of rays onto the receiver except the one at the center. Notwithstanding nearly no shading or blocking among the primary reflectors, the mirror in the middle is shaded by the receiver which is shown in Figure 4.11.

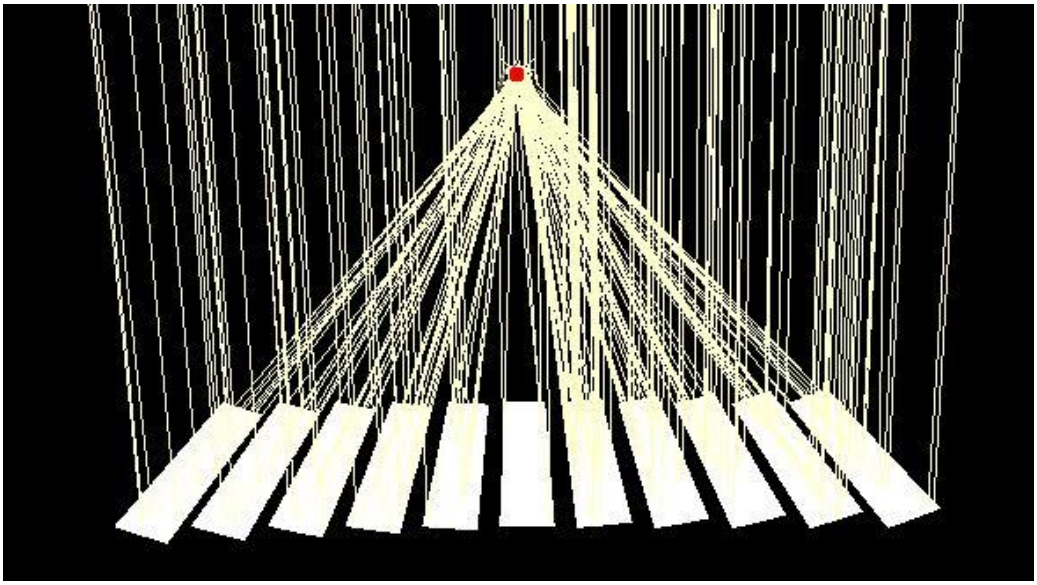

Figure 4.11 Rays incident on the absorber for incidence angle of 0°.

The flux distribution is given in Figure 4.12. Most of the radiation concentrated on the Bottom Left and Bottom Right sections; however, intensity is minimally higher than 30° case. The average flux is around 3.4% more than average for angle of incidence of 30°.

The variation in the value of flux along the circumference of the absorber tube is shown in Figure 4.13. The peak flux is 41.3 kW m^{-2} and minimum flux is just 1% of maximum.

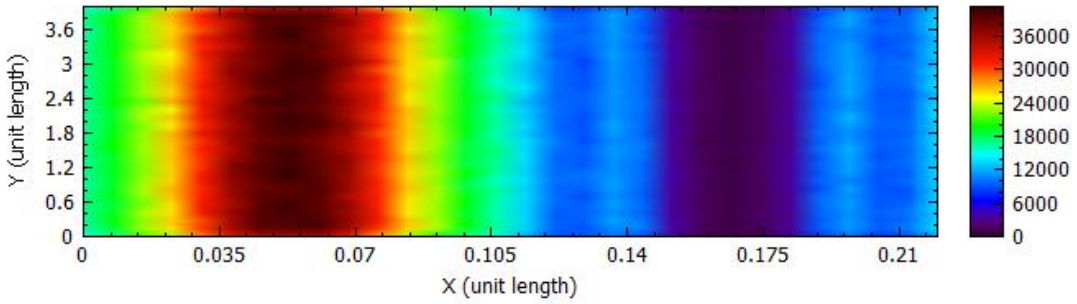

Figure 4.12 Flux distribution on the absorber for incidence angle of 0°.

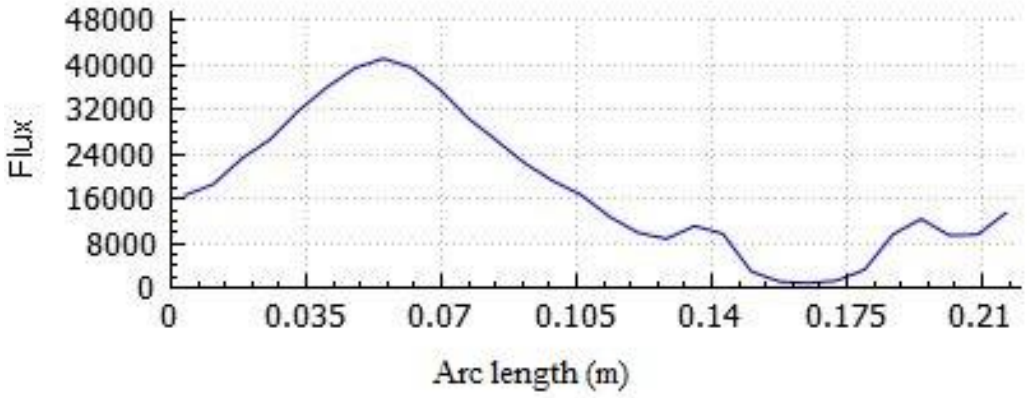

Figure 4.13 Rays incident on the absorber for incidence angle of 0° (Flux in W m^{-2}).

4.3.2. Flux Distribution for Incidence Angle 30°

A substantial amount of radiation strikes the receiver tube and both maximum power and total power are higher compared to previously mentioned cases. However, minimum flux is slightly less than that in 60° incidence angle. As seen in Figure 4.14, the receiver shades the mirror which is third from the left and it reflects less radiation as opposed to other mirrors in the module.

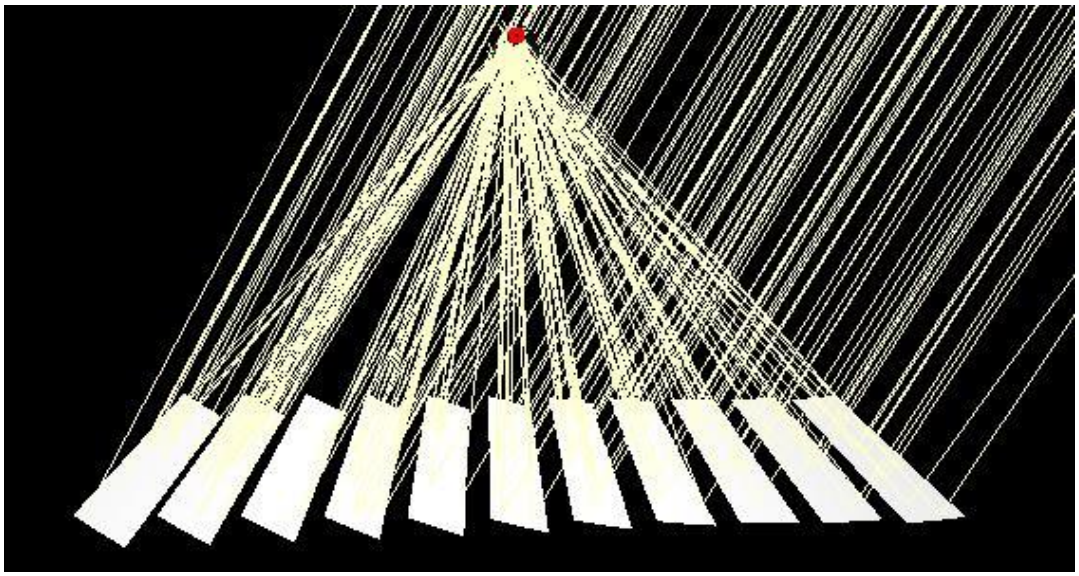

Figure 4.14 Rays incident on the absorber for incidence angle of 30°.

Most of the radiation is concentrated on the bottom left and right regions, shown in Figure 4.15, with peak flux of 40 kW m^{-2} at point B whereas minimum flux of 0.574 kW m^{-2} occurs at 85° above Left(L), illustrated in Figure 4.16. The total power incident on absorber is 15 kW. As demonstrated in Figure 4.16, the flux rises steadily as we move from point L towards bottom and peaks at B. Then there is a marked drop until Top(T) bottoming out then. A slight recovery is observed in Top Left region.

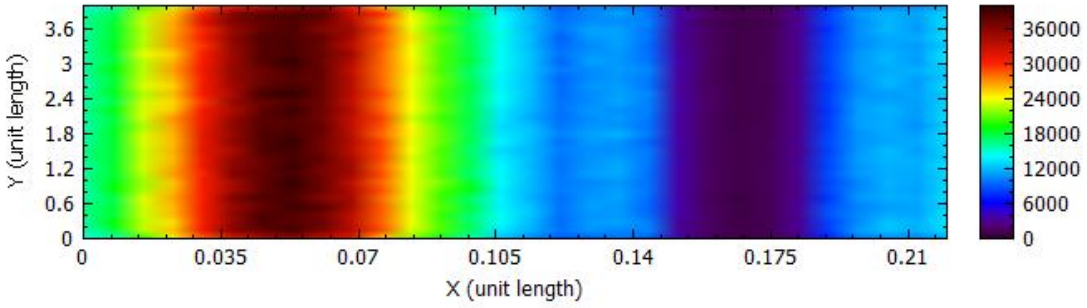

Figure 4.15 Flux distribution on the absorber for incidence angle of 30°.

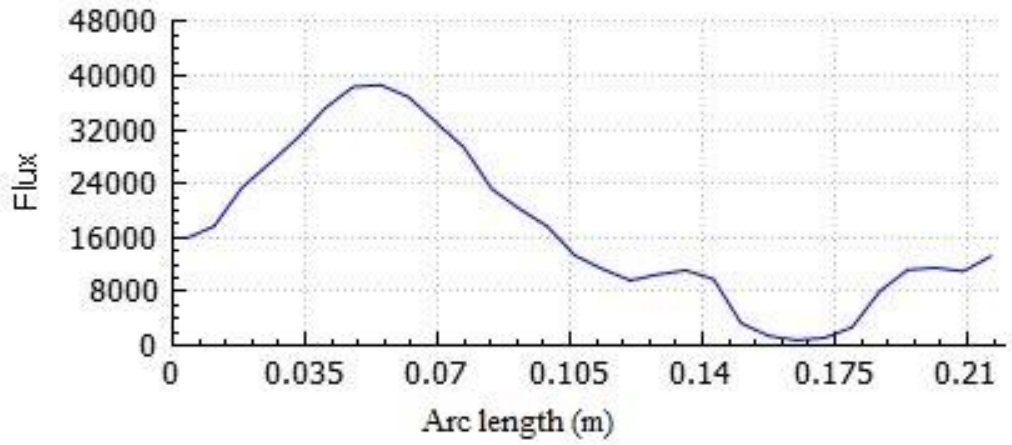

Figure 4.16 Rays incident on the absorber for incidence angle of 30° (Flux in W m^{-2}).

4.3.3. Flux Distribution for Incidence Angle 60°

A considerable amount of radiation is incident onto the absorber as depicted in Figure 4.17 and no shading by receiver or mirror rows is observed. All the mirrors contribute in reflecting sun rays towards the receiver

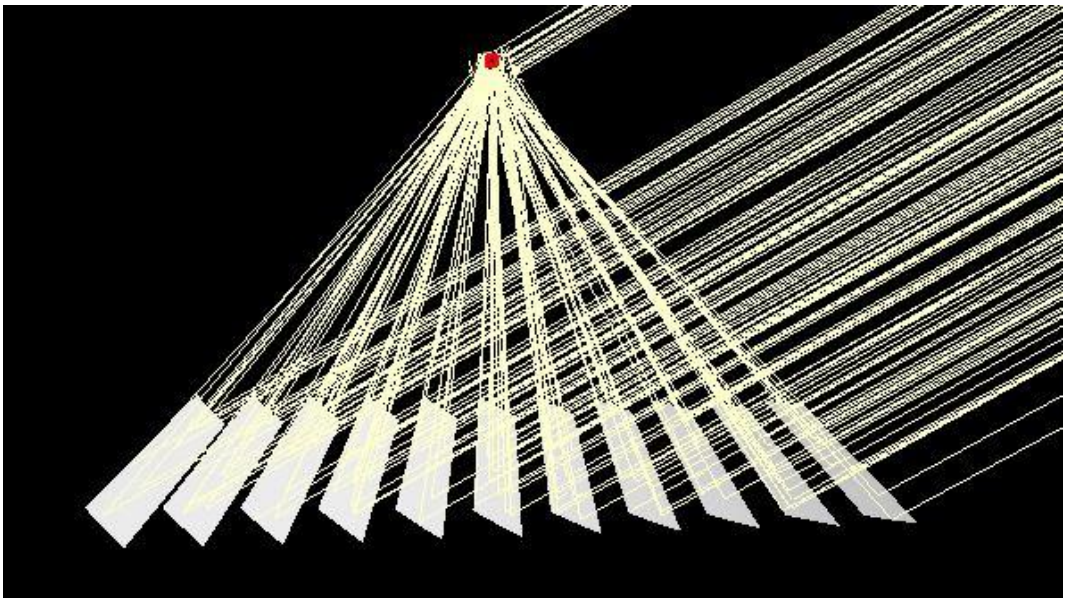

Figure 4.17 Rays incident on the absorber for incidence angle of 60°.

The flux distribution is given in Figure 4.18. The flux is spread over wider area and peaks at 78° below Left(L) with a value of 28.7 kW m^{-2} and it is about 36.5 times the minimum flux. The curve of circumferential heat flux is shown in Figure 4.19 and it is seen that flux increases from Left(L) position and reaches maxima near the Bottom(B) point. Then it falls significantly until Top(T) whereupon recovers to some extent.

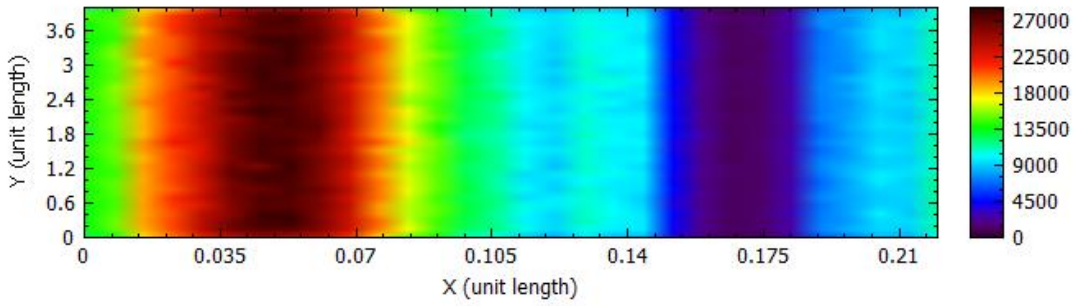

Figure 4.18 Flux distribution on the absorber for incidence angle of 60°.

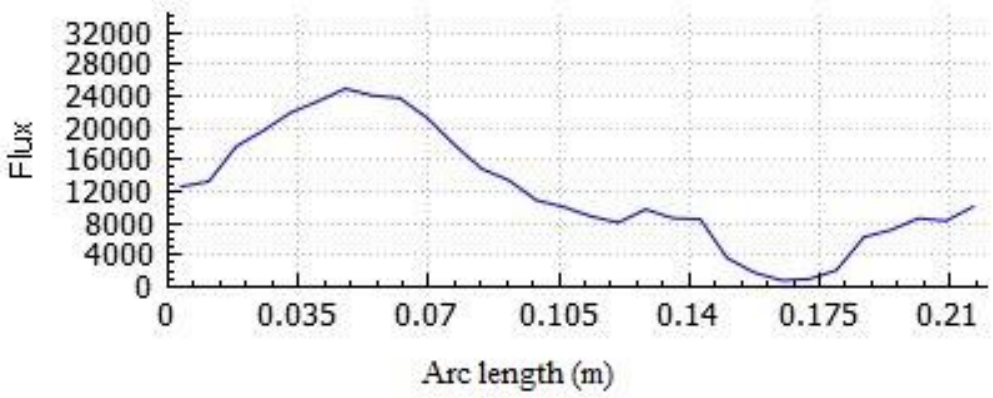

Figure 4.19 Rays incident on the absorber for incidence angle of 60° (Flux in W m^{-2}).

4.3.4. Flux Distribution for Incidence Angle 90°

The amount of energy incident on the receiver for angle of incidence of 90° is quite low as seen in Figure 4.20 and hence the maximum flux on the absorber tube is quite low. The mirrors at the left end of the collector contribute almost nothing in reflecting sun rays onto the receiver and most of the radiation falls on the left bottom of the tube. The flux distribution on absorber surface is shown in Figure 4.21.

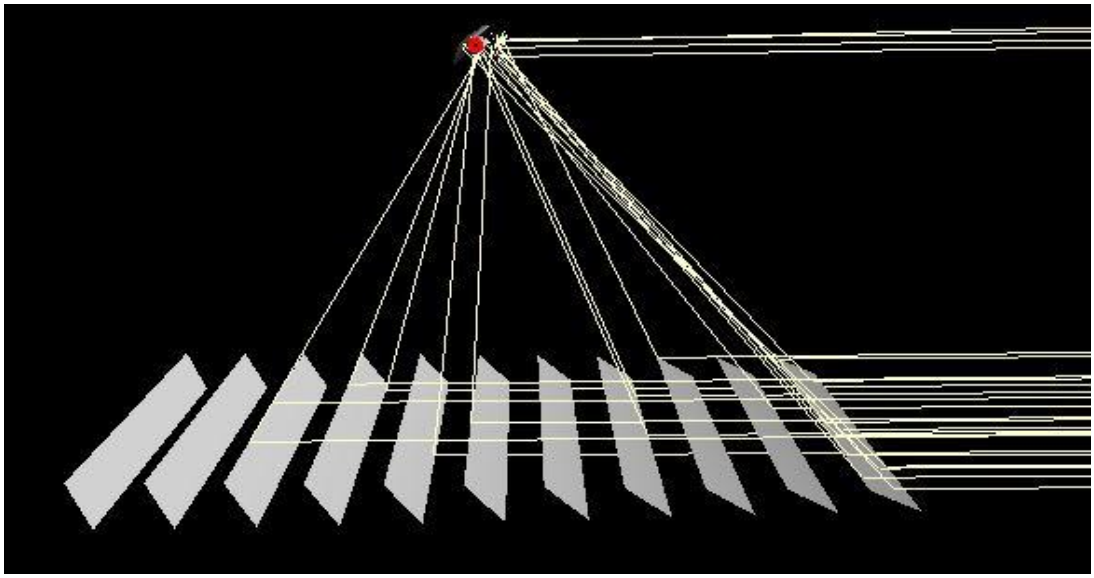

Figure 4.20 Rays incident on the absorber for incidence angle of 90°.

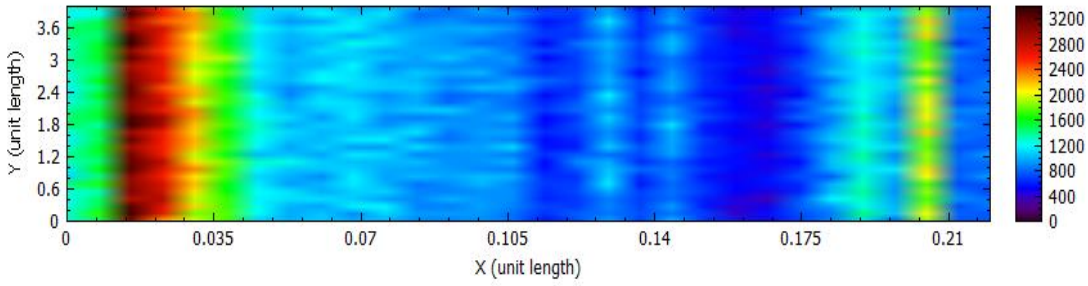

Figure 4.21 Flux distribution on the absorber for incidence angle of 90°.

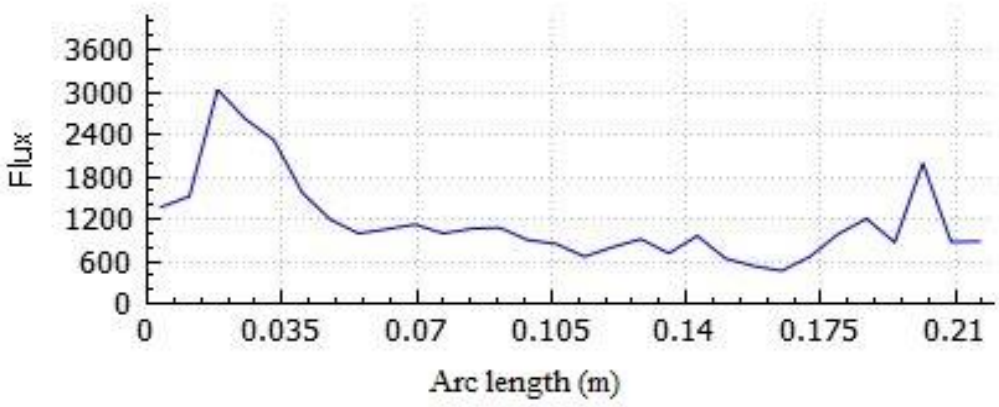

Figure 4.22 Rays incident on the absorber for incidence angle of 90° (Flux in W m^{-2}).

The maximum flux is 3.401.5 kW m^{-2} at 30° below left side as shown in Figure 4.22 and minimum flux is marginally under 10% of maximum flux. As mentioned earlier most rays impinge on left section of the tube, hence highest intensity is at the left bottom and a lesser peak at about 28° above left.

4.4. LF Field Specification

In this section LF field sizing and dimensions of all components of collector is explained.

4.4.1. Primary Mirror Field

Collector's aperture area plays an important role in overall collection of solar energy and so as to determine the most efficient primary mirror width and row arrangement, three cases are examined and the specification which fulfills the area requirement, that is, 160 m^2 which is large enough for LF collector to supply 92 kW. Based on results obtained in Section 4.2.3, three mirror width are considered – mirror width of 0.45 m in Case 1, 0.50 m in Case 2 and 0.52 m in Case 3 which are presented in Table 4.5, Table 4.6 and Table 4.7 respectively.

Table 4.5 Case 1 with mirror width of 0.45 m.

No. of mirrors rows	9	11	13
Aperture width (m)	4.05	4.95	5.85
Length of module (m)	4	4	4
Total length of collector (m)	40	32	28
Module aperture area (m^2)	16.2	19.8	23.4
Number of modules	10	8	7
Total collector area (m^2)	162	158.4	163.8
Total number of mirrors	90	88	91
Comment	Too Large	Too Small	Too Large

Table 4.6 Case 2 with mirror width of 0.50 m.

No. of mirrors rows	9	11	13
Aperture width (m)	4.5	5.5	6.5
Length of module (m)	4	4	4
Total length of collector (m)	36	28	24
Module aperture area (m^2)	18	22	26
Number of modules	9	7	6
Total collector area (m^2)	162	154	156
Total number of mirrors	81	77	78
Comment	Too Large	Too Small	Too Small

Table 4.7 Case 3 with mirror width of 0.52 m.

No. of mirrors rows	9	11	13
Aperture width (m)	4.68	5.72	6.76
Length of module (m)	4	4	4
Total length of collector (m)	36	28	24
Module aperture area (m^2)	18.72	22.88	27.04
Number of modules	9	7	6
Total collector area (m^2)	168.48	160.16	162.24
Total number of mirrors	81	77	78
Comment	Too Large	Suitable	Too Large

The configuration with 11 rows and mirror width of 0.52 m requires least number of mirrors which is 77 and is neither undersized nor oversized and therefore selected for the further calculations in this study.

4.4.2. Secondary Reflector Geometry and Absorber Tube

The absorber used in the simulation is Schott PTR70 which is an evacuated tube, that is, an absorber pipe of stainless steel DIN1.4541 and a glass cover to maintain vacuum around the tube in order to prevent heat losses during operation. The length of each tube is 4 m and they are connected in series to achieve the desired collector length.

Another component of linear Fresnel collector is the secondary reflector. The compound parabolic reflector (CPR) considered in this study is shown in Figure 4.23. The truncation height of the compound parabola is 0.167 m and half acceptance angle is 46° and being a symmetrical compound parabolic reflector, the half acceptance angle is same for both clockwise and anti-clockwise directions. The reflecting material is a layer of polished aluminum and the thickness of insulation to prevent the heat loss to the environment is 0.05 m and the thermal conductivity of insulation is 0.05 W m^{-2} K^{-1} [39].

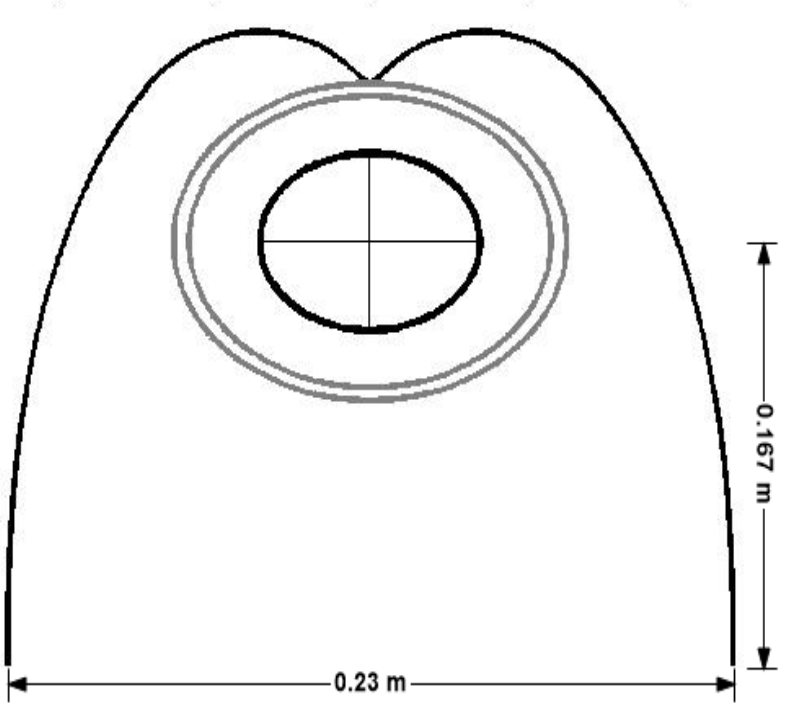

Figure 4.23 Dimensions and geometry of receiver

The parametric equations governing the CPR profile for an evacuated tube receiver is found to be,

$$X = r_{abs,o}\left[\sin(\theta) - \left(\frac{\rho(r_{g,o} - r_{abs,o})\cos(\theta)}{r_{abs,o}}\right)\right] \tag{4.6}$$

$$Y = r_{abs,o}\left[\cos(\theta) - \rho\sin(\theta) + \left(\frac{r_{g,o} - r_{abs,o}}{r_{abs,o}}\right)\right] \tag{4.7}$$

Where

ρ is a parameter which depends on θ and is found using equations below [2],

$$\rho(\theta) = \theta \text{ for } |\theta| \leq \theta_c + \frac{\pi}{2} \tag{4.8}$$

$$\rho(\theta) = \left[\frac{\theta + \theta_c + \left(\frac{\pi}{2}\right) - \cos(\theta - \theta_c)}{1 + \sin(\theta - \theta_c)}\right] \text{ for } \left(\theta_c + \frac{\pi}{2}\right) \leq \theta \leq \left(\frac{3\pi}{2} - \theta_c\right) \tag{4.9}$$

4.4.3. LF Design Summary

Finally, the measurement of mirror field is shown in Figure 4.24 and the optical, thermal and dimensional parameters of the LF are given in Table 4.8

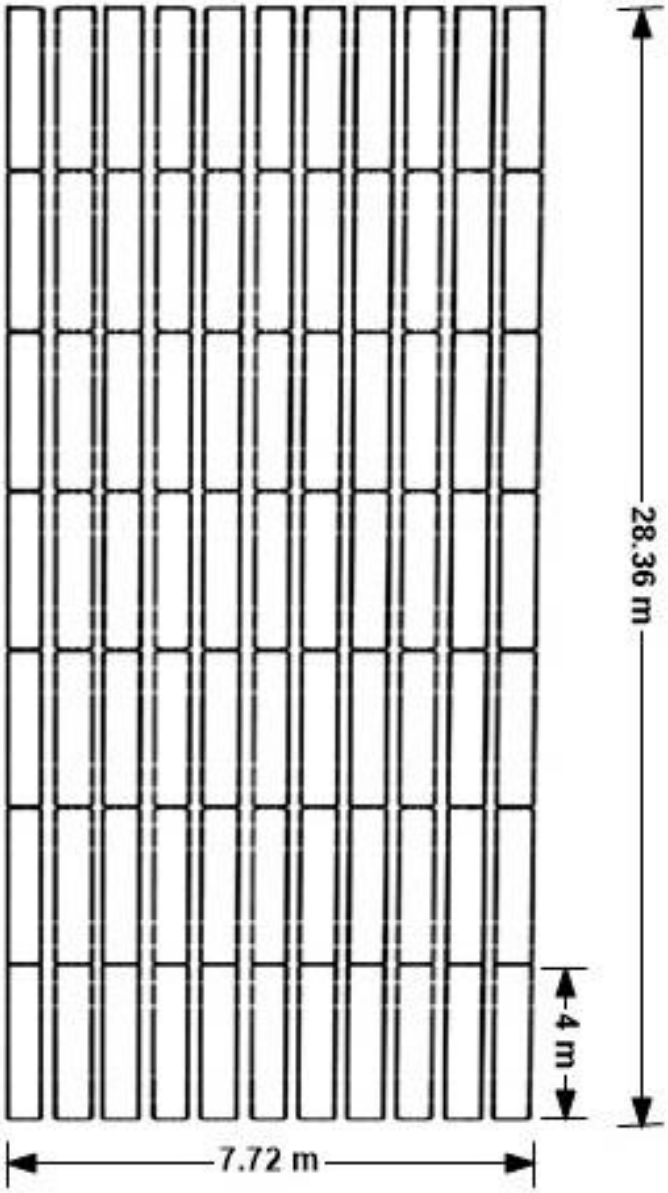

Figure 4.24 LF field dimensions.

Table 4.8 Specification of proposed linear Fresnel collector.

Characteristic	**Value**	**Unit**
Number of mirrors per module	11	-
Number of modules	7	-
Width of each mirror	0.52	m
Length of each mirror	4	m
Longitudinal spacing between mirrors	0.06	m
Transversal spacing between mirrors	0.2	m
Mirror profile	Parabolic	-
Receiver height above primary reflector plane	4.2	m
Absorber tube inner diameter	0.066	m
Absorber tube outer diameter	0.07	m
Receiver Cover glass inner diameter	0.115	m
Receiver Cover glass outer diameter	0.125	m
Total receiver tube length	28.36	m
Reflectivity of primary reflectors at normal incidence	0.95	-
Slope deviation of primary reflectors at normal incidence	4	mrad
Reflectivity of secondary reflector	0.91	-
Secondary reflector acceptance angle	46	°
Absorptivity of receiver at normal incidence	0.95	-
Emissivity of receiver	0.086	-
Transmittance of glass cover	0.965	-
Emissivity of glass cover	0.89	-
Thermal conductivity of glass cover	1.1	$W\ m^{-2}\ K^{-1}$
Emissivity of inner secondary reflector surface	0.04	-
Emissivity of outer secondary reflector surface	0.64	-
Thermal conductivity of secondary reflector insulation	0.05	$W\ m^{-2}\ K^{-1}$

4.5. IAM for Designed Linear Fresnel Collector

A ray trace simulation is done to calculate IAM for the designed collector and the results are shown in Table 4.9.

Table 4.9 IAM for the LF using ray trace analysis.

Incidence Angle	Transversal IAM	Longitudinal IAM
0°	1.000	1.000
10°	0.981	0.962
20°	0.969	0.892
30°	0.955	0.794
40°	0.938	0.672
50°	0.910	0.539
60°	0.745	0.371
70°	0.520	0.198
80°	0.273	0.033
90°	0.064	0.000

A five degree polynomial equation, with good approximation, is found using curve fitting for both transversal and longitudinal incidence angle modifiers and these equations are used further in determining thermal performance of suggested LF.

The equation for transversal incidence angle modifier is

$$\mathrm{IAM}(\phi_T) = a_1 + a_2\phi_T^5 + a_3\phi_T^4 + a_4\phi_T^3 + a_5\phi_T^2 + a_6\phi_T \quad (4.10)$$

And equation for longitudinal incidence angle modifier (IAM (φL)) is

$$\mathrm{IAM}(\phi_L) = b_1 + b_2\phi_L^5 + b_3\phi_L^4 + b_4\phi_L^3 + b_5\phi_L^2 + b_6\phi_L \quad (4.11)$$

The coefficients in polynomial are given in Table 4.10 and Table 4.11.

Table 4.10 Coefficients for transversal IAM.

a_1	1.007
a_2	2.256E-09
a_3	-4.479E-07
a_4	2.802E-05
a_5	-7.134E-04
a_6	5.312E-03

Table 4.11 Coefficients for longitudinal IAM.

b_1	1.000
b_2	9.996E-10
b_3	-1.869E-07
b_4	1.274E-05
b_5	-4.927E-04
b_6	7.248E-04

4.6. Temperatures and Heat Loss

Most industrial processes operate between 80-250°C so the thermal performance of the designed LF is predicted for the medium and medium high temperature range. The surface temperature of various components of receiver is given in Table 4.12 and change in heat loss per unit length with respect to heat transfer fluid temperature is illustrated in Figure 4.25. Ambient temperature of 30°C is considered for each simulation.

As the temperature of the absorber increases, so does the temperature of surrounding, that is, HTF, glass cover and secondary reflector. The glass cover temperature, both inside and outside, is not as high as absorber's outside temperature due to presence of vacuum and low absorptivity of glass material.

Along with this, it is observed that the temperature of secondary reflector's inner surface is close to that of ambient and at low temperatures its outer surface temperature is same as surrounding. The outside surface temperature of secondary reflector depends on the insulation thickness between inner and outer surface.

Table 4.12 Surface temperatures and heat loss.

T_{HTF} (°C)	$T_{abs,i}$ (°C)	$T_{abs,o}$ (°C)	$T_{g,i}$ (°C)	$T_{g,o}$ (°C)	$T_{sr,i}$ (°C)	$T_{sr,o}$ (°C)	**Heat Loss** ($W\ m^{-1}$)
100	105.53	107.47	41.18	41.09	33.15	30.00	11.94
120	125.52	127.46	41.89	41.76	33.36	30.00	16.92
150	155.50	157.44	43.17	42.98	33.73	30.00	25.92
170	175.49	177.43	44.18	43.94	34.03	30.00	33.06
200	205.47	207.40	45.97	45.63	34.56	30.00	45.70
250	255.43	257.35	49.77	49.23	35.72	30.02	72.69
300	305.37	307.27	54.77	53.97	37.31	30.05	108.45

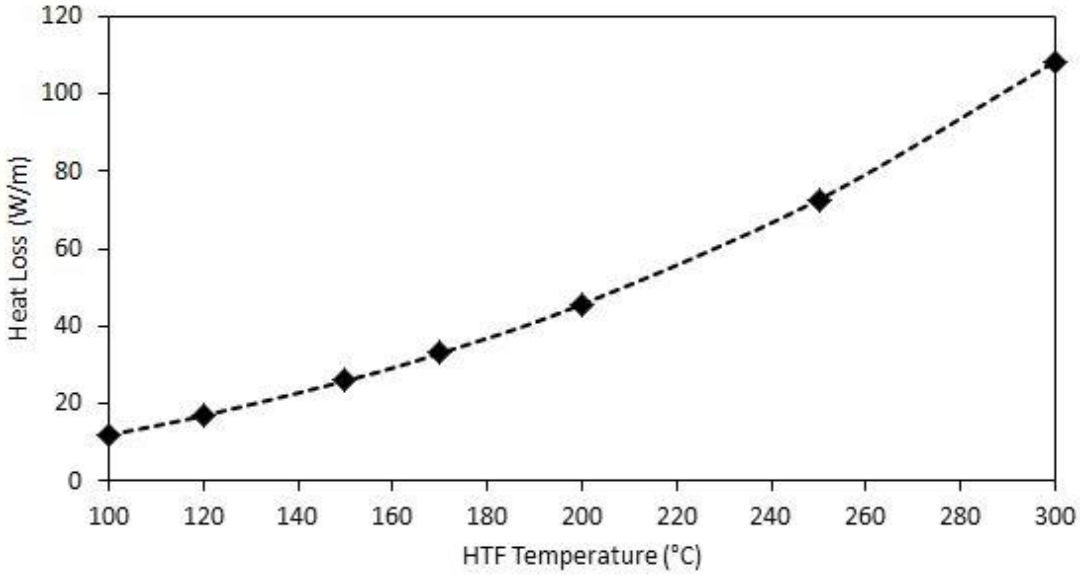

Figure 4.25 Heat loss in the receiver with respect to heat transfer fluid temperature.

According to Figure 4.25, the heat loss rises with the increase in heat transfer fluid temperature because of augmentation in the temperature difference between the receiver and surrounding. Also it is noticed that heat loss does not vary linearly with temperature of heat transfer fluid, for instance, for HTF temperature of 100°C, the heat loss value is 11.94 W m^{-1} and when HTF temperature is doubled, heat loss is increased four times. Similarly a threefold rise in HTF temperature gives a heat loss of 108.45 W m^{-1} which is about nine times the value at 100°C. This nonlinear trend is due to radiative losses.

4.7. Daily and Monthly Performance

The results are presented for representative clear summer day, partially cloudy summer day, cloudy fall day and clear winter day. These days are expected to be sufficient to describe the performance of the system. Furthermore, weather data for Konya (37°52’ N 32°29’E) used in this analysis is obtained using Meteonorm (4-15% uncertainty in DNI).

The outlet temperature prediction for clear summer day (July 3) is shown in Figure 4.26. The temperature output reaches its peak value of 160°C, however, some fluctuations are observed around noon due to variations in irradiance.

Similar trend is observed in thermal efficiency, which is presented in Figure 4.27, with lesser degree of fluctuations and maximum thermal efficiency during the day is 66.35%.

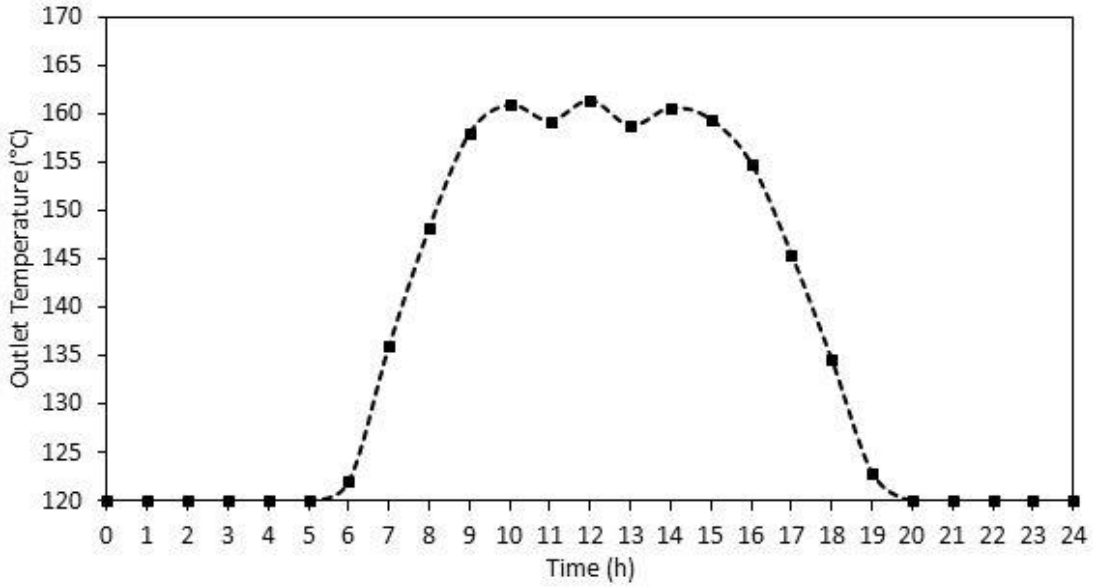

Figure 4.26 Hourly temperature output for clear summer day (July 3).

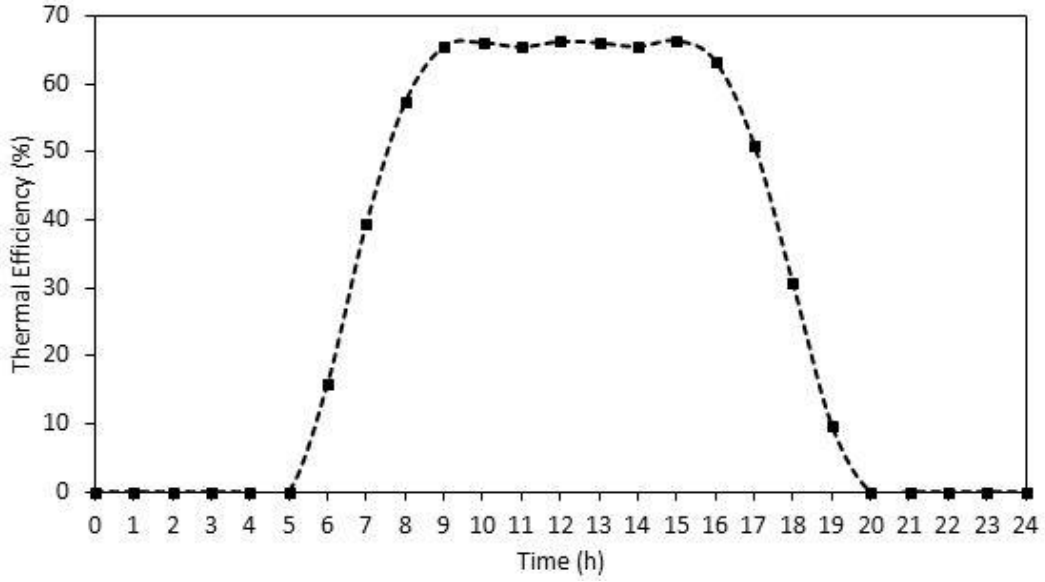

Figure 4.27 Hourly thermal efficiency for clear summer day (July 3).

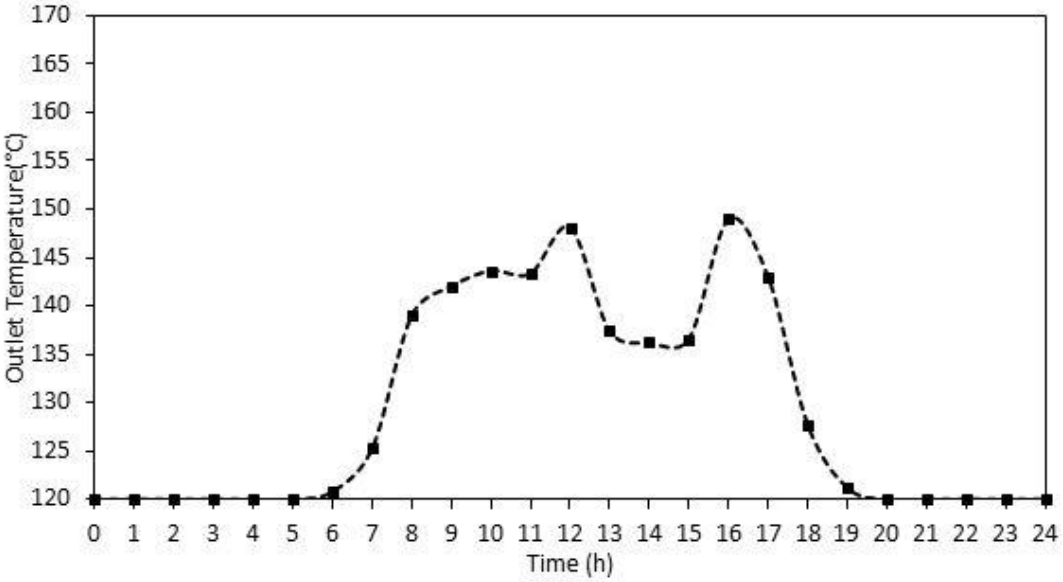

Figure 4.28 Hourly temperature output for partially cloudy summer day (August 7).

Meanwhile, as expected, outlet temperature is markedly non uniform for a partially cloudy summer day illustrated in Figure 4.28. During early sunshine hours, sky is moderately covered and temperature output is in the range of 139°C to 143°C and reaches peak of 148°C at midday followed by a sharp decline and bottoming out at

136°C. At the end of day, the sky is significantly less cloudy hence a peak is observed at 4 pm and later on output decreases gradually in accordance with DNI.

The thermal efficiency (Figure 4.29), however, follows a curve with slight changes during operation time (9:00 to 17:00) and peaks at 63%.

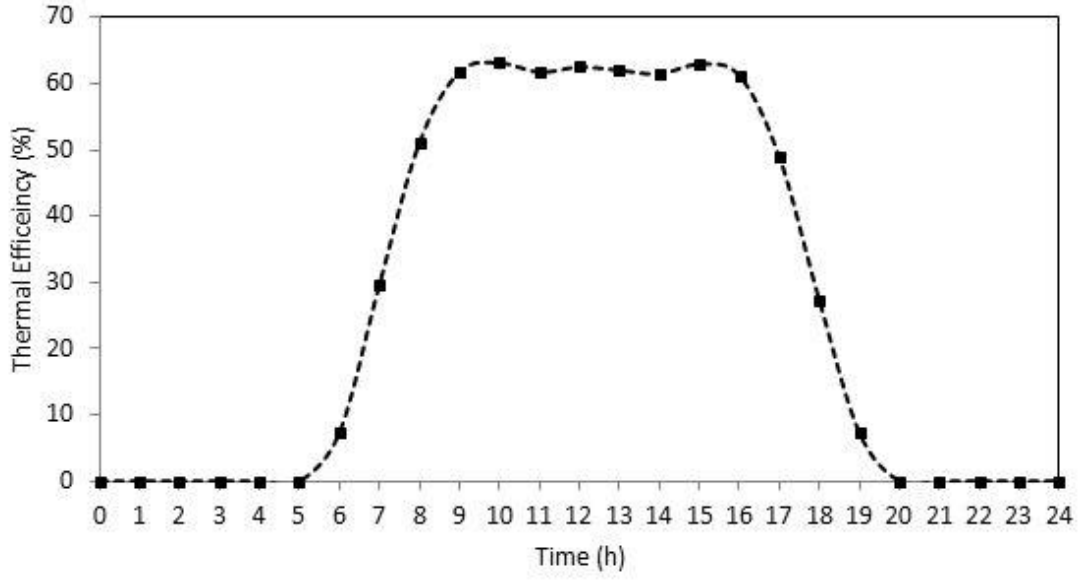

Figure 4.29 Hourly thermal efficiency for partially cloudy summer day (August 7).

The results for a cloudy fall day are presented in Figure 4.30 and it is inferred that the output is substantially low throughout the day with a maximum temperature output of 133°C. This meager performance is on account of moderate DNI and high cloud cover during whole day.

Additionally, significant variation in thermal efficiency is observed from 8 a.m. to 5 p.m as seen in Figure 4.31. The thermal efficiency drops to naught during time of substantial cloud cover and the highest value achieved by the collector is 49%.

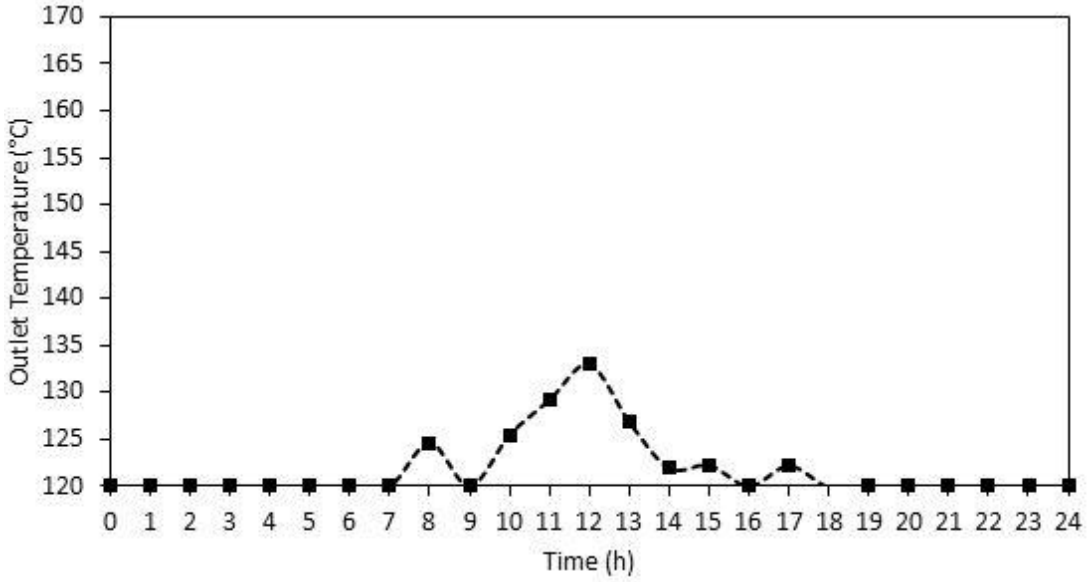

Figure 4.30 Hourly temperature output for cloudy fall day (September 24).

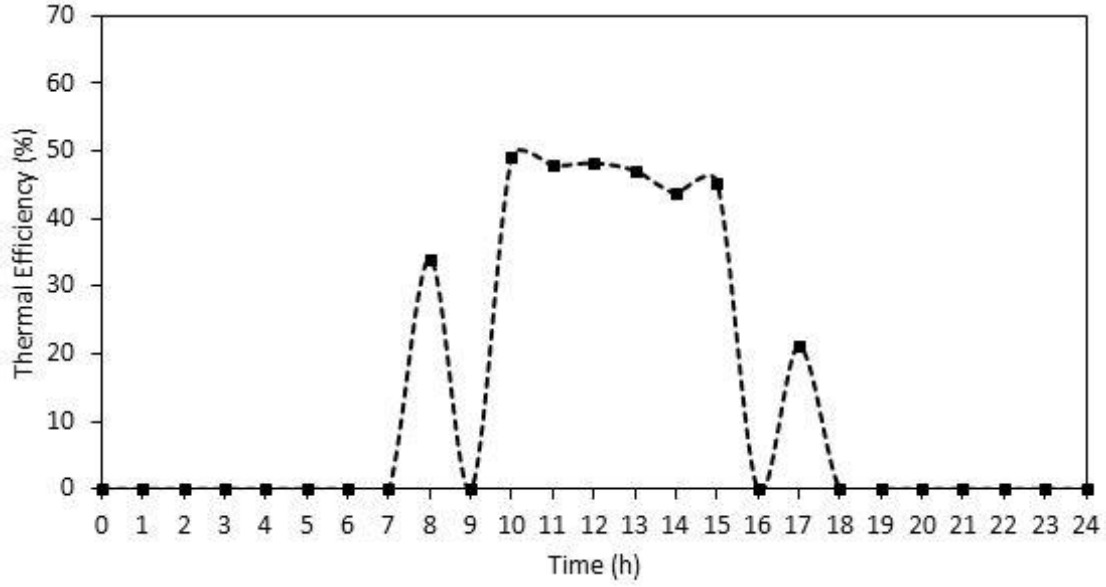

Figure 4.31 Hourly thermal efficiency for cloudy fall day (September 24).

Furthermore, Figure 4.32 shows the thermal performance for a clear winter day and throughout the sunshine hours, the temperature output is consistent with a value of approximately 138°C, with exclusion of solar noon where slight sag is observed. This sag is attributed to the position of sun which is lower in the sky, in the due South direction at noon during winter compared to other times of the winter day and single axis tracking collector is unable to tilt in this direction. Therefore, higher angle of incidence.

The hourly variation in thermal efficiency of the system is presented in Figure 4.33 and noticeable sag, similar to temperature profile, is seen at noon. The thermal efficiency is considerably lower compared to clear summer day with apex of 32% which is marginally less than half of peak thermal efficiency for clear summer day. This decline in thermal efficiency can be explained using Equation (4.12),

$$\eta_{th} = \eta_{opt} - \frac{Q_{loss\_thermal}}{I_b} \tag{4.12}$$

The optical efficiency is independent of the amount of radiation and only varies with solar-collector geometry. The thermal losses are a function of receiver temperature and ambient temperature, and therefore independent of solar radiation. Thus the impact of solar radiation on thermal efficiency is clearly seen in the denominator; i.e., as solar radiation decreases the second term increases and thermal efficiency decreases.

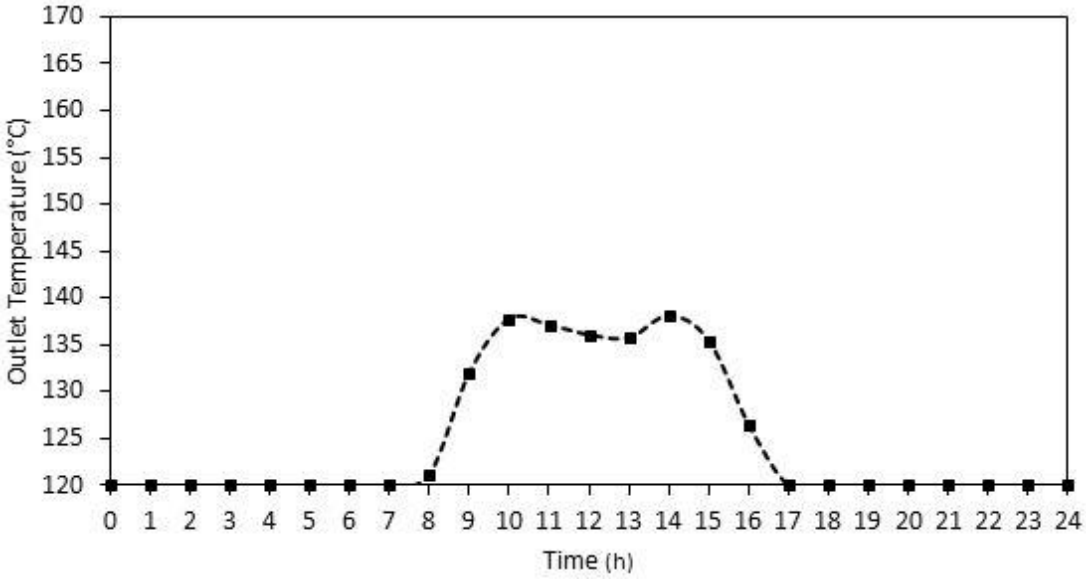

Figure 4.32 Hourly temperature output for clear winter day (November 26).

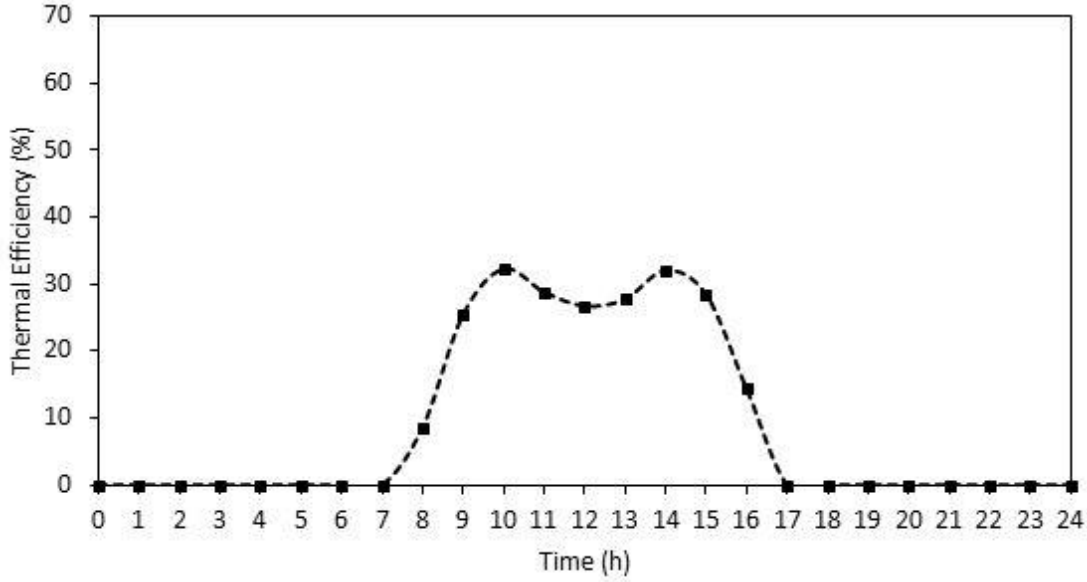

Figure 4.33 Hourly thermal efficiency for clear winter day (November 26).

The monthly performance predictions of the LF are given in Figure 4.34. A substantial amount of energy is delivered during summer months of June, July and August that is 20 MWh, 23 MWh and 21 MWh respectively. On the contrary, it is much lower for the rest of the year. This is due to pronounced insolation and fewer overcast days during summer months. The total useful energy gain for the 6 months from October to March is 32.54 MWh which is nearly half of the energy delivered during three summer months – June, July and August.

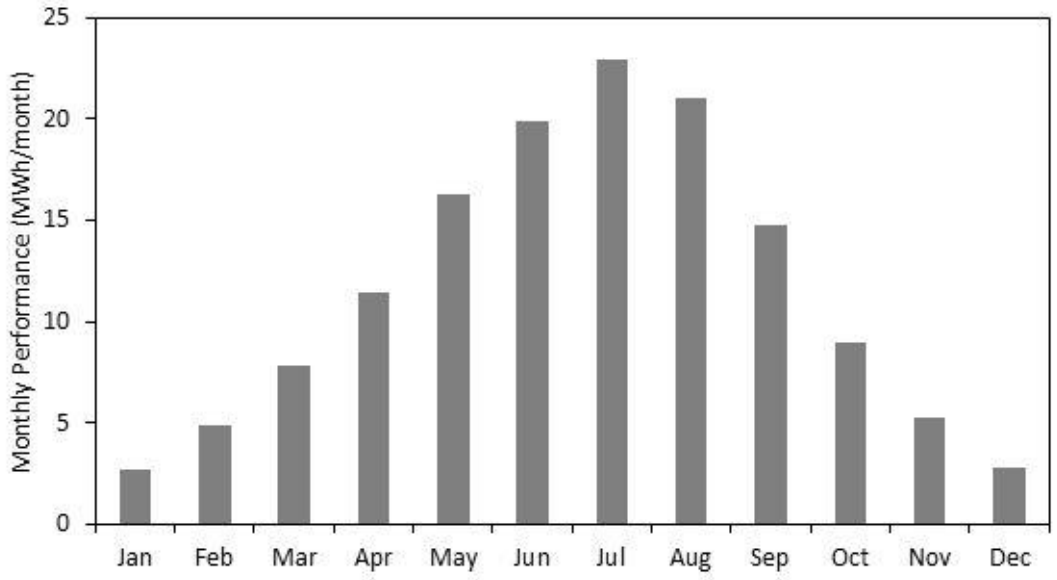

Figure 4.34 Monthly performance of LF system.

Along with this, solar fraction for each month is shown in Figure 4.35 where solar fraction is ratio of total power delivered for a given time period by the solar collectors to the total power required for the industrial process for a given time period. Results are same as monthly performance – maximum solar fraction in July (33.6%) and minimum in January (4%).

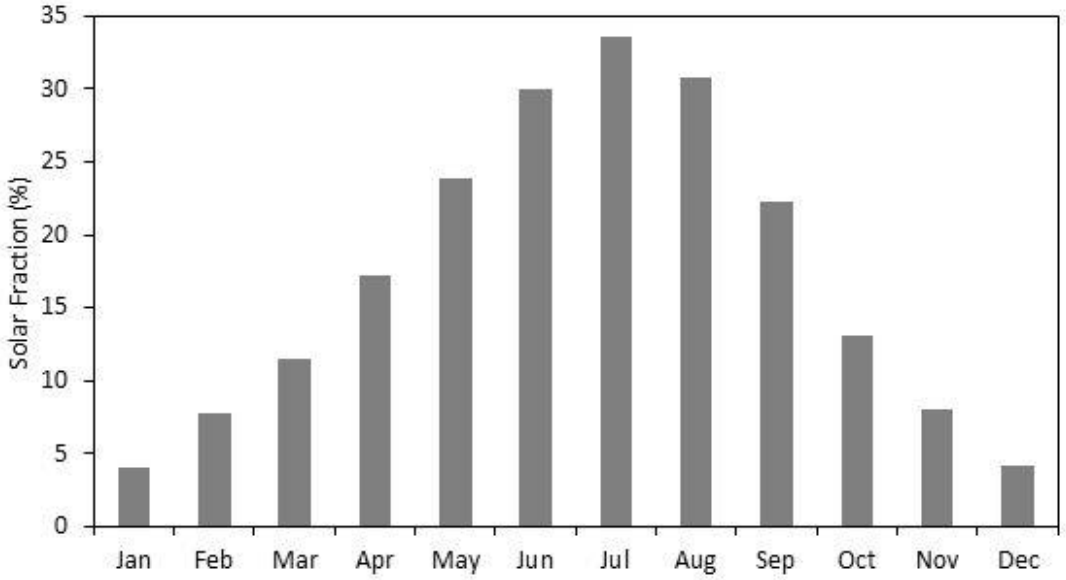

Figure 4.35 Solar fraction for each month.

The abridged summary of the design specification and thermal performance is presented in Table 4.13. The total area required for the setup is approximately 219 m^2 with 77 mirrors and system delivers peak power of 92 kW_{th}.

Table 4.13 Solar field design and performance summary.

Design Parameter	**Value**	**Unit**
Direct Normal Irradiation	900	W m^{-2}
Solar Field Outlet Temperature	160	^oC
Solar Field Inlet Temperature	120	^oC
Peak Thermal Efficiency	66.5	%
Gross Energy Yield	598.5	W m^{-2}
Estimated Solar Circuit Losses	4	%
Net Energy Yield	574.5	W m^{-2}
Area of one module	22.88	m^2
Total Number of Mirrors	77(11x7)	-
Total Collector Area	160	m^2
Net Energy Yield	92	kW
Total Area Required	218.94 (7.72 x 28.36)	m^2

CHAPTER 5

CONCLUSIONS AND RECOMMENDATIONS

In this chapter, major conclusions from analysis presented in this thesis are given in Section 5.1, followed by recommendation for future works in Section 5.2.

5.1. Conclusions

A detailed optical and thermal model of linear Fresnel collector has been developed and validated against published data. Afterwards, the effect of key design parameters on LF's optical performance is studied and LF for an ice cream factory situated in Konya (Turkey) has been designed by considering basic trends in collector parameters. Furthermore, thermal analysis of the designed collector is done. In addition to predicting monthly energy yield, the model is capable of determining temperature output and thermal efficiency for all conditions, but it is applied in this work to clear summer day, partially cloudy summer day, cloudy fall day and clear winter day. The flux distribution on absorber tube throughout the day has also been studied. Significant conclusions from current work are as follows:

- Validation is done in three parts – IAM values from ray tracing were compared with IAM of a commercially available LF collector, then inclination of each row at particular time of year found using ray tracing and measured data are plotted together. Optical as well as thermal results show good agreements with measured data in the literature.

- It is observed that curved mirrors are significantly more efficient than completely flat ones. The optimal ratio of focal length of individual mirrors to the distance of respective mirrors from the receiver is found to be 1 (based on optical considerations and for normal incidence).

- Parametric analysis showed that for a medium sized LF collector suitable: height is between 4 and 6 m, width of primary mirrors is 0.425 m to 0.525 m and row spacing is from 0.15 m to 0.2 m.

- In addition to parametric analysis, flux distribution is also studied and it is observed that most of the radiation is concentrated on bottom half of the tube, that is, the side facing the reflectors. The flux distribution is non-uniform especially for high incidence angles. Symmetrical distribution is seen in case of normal incidence, on the other hand, non-uniform for incidence angle of 90°.

- The most suitable LF design for the industry considered in this study is found to be – 11 mirror rows of 0.52 m width each and 7 modules connected in series to form a collector 28.36 m long and 7.72 m wide with total 77 mirrors.

- According to thermal analysis, for temperature range of 100°C to 300°C, the temperature of glass cover and inside surface of secondary reflector increases with rise in absorber's temperature. Furthermore, the temperature of secondary reflector's outside surface is affected more by insulation thickness and ambient conditions than absorber temperature.

- Heat loss in the receiver is 11.94 W m^{-1} for 100°C absorber temperature and 108.45 W m^{-1} for 300°C absorber temperature. Additionally, the relation between heat loss and absorber temperature is observed to be non-linear due to radiative losses.

- Simulation done for daily performance shows peak thermal efficiency of 66.35% on a clear summer day and 63% on a partially cloudy day, however, output temperature range for partially cloudy is between 139°C to 143°C which is much lower than required output of 160°C. In addition, maximum temperature for cloudy fall day is 133°C with 49% peak thermal efficiency. Temperature output on a clear winter day reaches 138°C, more than cloudy fall day, but maximum thermal efficiency is 32% which is lowest among all the days.

- Monthly energetic calculations shows July as the month of highest energy yield as well as maximum solar fraction which are 23 MWh and 33.6% respectively. The total energy gain during June, July and August is found to be twice the total energy yield from October to March.

5.2. Recommendations for Future Work

The current study is a basic model for design and application of LF for SHIP and therefore should be seen as a stepping stone for further research. There are several additions which could be made to improve the model presented in this thesis. Firstly, optical and thermal properties such as emissivity, heat capacity and thermal conductivity are considered constant, however, for more accurate results, temperature dependence of these properties should be considered especially for high temperature applications. Secondly, the convective heat transfer coefficient for the heat transfer between outer surface of the secondary reflector and ambient is calculated using relations for flow over cylindrical surface. This is due to unavailability of convective heat transfer equations for compound parabolic geometry. A simulation through CFD is required to determine the flow characteristics, heat transfer coefficient and temperature distribution in the inner and outer vicinity of secondary reflector.

Other extensions include accounting non-uniform flux distribution on receiver and gas seepage in the annulus during heat loss calculations. Furthermore, the LF with an auxiliary heater or storage can be studied which will make it a credible system able to operate all year long. Finally, the weather data used for simulation is generated by Meteonorm software which lacks the accuracy of real data. The uncertainty in DNI is 4-15% and depends on the accuracy of measurement stations [51]. Therefore, latest weather data can be used for better accuracy. Another important addition can be optimization of LF design parameters. In addition to technical assessment, an economic analysis can provide more insight into feasibility of LF for SHIP.

REFERENCES

[1] G. Morin, J. Dersch, W. Platzer, M. Eck, A. Haberle, "Comparison of Linear Fresnel and Parabolic Collector poer plants", *Solar Energy*, vol. 86, pp. 1-12, 2012.

[2] Kalagirou, S. A., "Solar Energy Engineering Processes and Systems", 1st edition, Massachusetts: Elsevier, 2009.

[3] "Linear Fresnel Reflector based Solar System: Operation and Maintenance Manual", Ministry of New and Renewable Energy, Government of India, 2014.

[4] G. Zhu, T. Wendelin, M. J. Wagner, and C. Kutscher, "History , current state , and future of linear Fresnel concentrating solar collectors," *Sol. Energy*, vol. 103, pp. 639–652, 2014.

[5] Patnode M. A., "Simulation and Performance Evaluation of Parabolic Trough Solar Power Plants", M.S. Thesis ,University of Wisconsin, Madison, 2006.

[6] "Process Heat Collectors", IEA SHC-Task 33 and SolarPACES-Task IV, 2008.

[7] Dickinson, W. C., Cheremisinoff, P. N., "Solar Energy Technology Handbook - Applicatoin system design and economics", *Energy, Power and Environment*, vol.6, 1980.

[8] "Solar Heat for Industrial Processes", IEA-ETSAP and IRENA Technology Brief E21, 2015.

[9] Silvi, C., "The pioneering work on linear Fresnel reflector concentrators in Italy", 15th SolarPACES International Symposium, 2009.

[10] F. J. Pino, R. Caro, F. Rosa, and J. Guerra, "Experimental validation of an optical and thermal model of a linear Fresnel collector system," *Appl. Therm. Eng.*, vol. 50, no. 2, pp. 1463–1471, 2013.

[11] Sen, P. K., K. Ashutosh, K. Bhuwanesh, Z. Engineer, S. Hegde, P. V. Sen, and P. Davies., "Linear Fresnel Mirror Solar Concentrator with tracking," *Procedia Eng.*, vol. 56, pp. 613–618, 2013.

[12] G. Mokhtar, B. Boussad, and S. Noureddine, "A linear Fresnel reflector as a solar system for heating water: Theoretical and experimental study," *Case Stud. Therm. Eng.*, vol. 8, no. August 2010, pp. 176–186, 2016.

[13] Dostucok, I., Selbas, R., Sencan, A., "Experimental Investigation of a Linear Fresnel", *J. of Thermal Science and Technology*, vol. 34, pp. 77–83, 2014.

[14] Industrial Solar, http://www.industrial-solar.de/content/en, last visited on January 2016.

[15] Feranova, www.feranova.com, last visited on January 2016.

[16] M. Haagen, C. Zahler, E. Zimmermann, and M. M. R. Al-najami, "Solar process steam for pharmaceutical industry in Jordan," *Energy Procedia*, vol. 70, pp. 621–625, 2015.

[17] J. D. Nixon and P. A. Davies, "Cost-exergy optimisation of linear Fresnel reflectors," *Sol. Energy*, vol. 86, no. 1, pp. 147–156, 2012.

[18] J. He, Z. Qiu, Q. Li, and Y. Zhang, "Optical design of linear Fresnel reflector solar concentrators," *Energy Procedia*, vol. 14, no. 2011, pp. 1960–1966, 2012.

[19] R. Abbas, M. J. Montes, M. Piera, and J. M. Martínez-Val, "Solar radiation concentration features in Linear Fresnel Reflector arrays," *Energy Convers. Manag.*, vol. 54, no. 1, pp. 133–144, 2012.

[20] G. Zhu, "Development of an analytical optical method for linear fresnel collectors," *Sol. Energy*, vol. 94, pp. 240–252, 2013.

[21] R. Abbas, J. Muñoz-Antón, M. Valdés, and J. M. Martínez-Val, "High concentration linear Fresnel reflectors," *Energy Convers. Manag.*, vol. 72, pp. 60–68, 2013.

[22] M. J. Montes, C. Rubbia, R. Abbas, and J. M. Martínez-Val, "A comparative analysis of configurations of linear fresnel collectors for concentrating solar power," *Energy*, vol. 73, pp. 192–203, 2014.

[23] F. Huang, L. Li, and W. Huang, “Optical performance of an azimuth tracking linear Fresnel solar concentrator,” *Sol. Energy*, vol. 108, pp. 1–12, 2014.

[24] V. Sharma, “Hourly and monthly variation in shading and blocking of aperture area in a linear fresnel reflector field,” *Energy Procedia*, vol. 48, pp. 233–241, 2014.

[25] S. Song, J. Ma, Z. Zhan, Y. Dai, "Optical Analysis and Optimization of the Linear Fresnel Collector's Mirror Field", *International Forum on Energy, Environment Science and Materials*, 2015.

[26] R. Abbas and J. M. Martínez-Val, “Analytic optical design of linear Fresnel collectors with variable widths and shifts of mirrors,” *Renew. Energy*, vol. 75, pp. 81–92, 2015.

[27] V. Sharma, J. K. Nayak, S. B. Kedare, "Effects of shading and blocking in linear Fresnel reflector field", *Solar Energy*, vol. 113, pp. 114-138, 2015.

[28] A. Hofer, D. Buchner, K. Kramer, S. Fahr, A. Hemisath, W. J. Platzer, S. Scholl, “Comparison of Two Different (Quasi-) Dynamic Testing Methods for the Performance Evaluation of a Linear Fresnel Process Heat Collector,” *Energy Procedia*, vol. 69, pp. 84–95, 2015.

[29] R. Abbas, M. J. Montes, A. Rovira, and J. M. Martínez-Val, “Parabolic trough collector or linear Fresnel collector? A comparison of optical features including thermal quality based on commercial solutions,” *Sol. Energy*, vol. 124, pp. 198–215, 2016.

[30] V. Sharma, S. Khanna, J. K. Nayak, and S. B. Kedare, “Effects of shading and blocking in compact linear fresnel reflector field,” *Energy*, vol. 94, pp. 633–653, 2016.

[31] S. Benyakhlef A. A. Mers, O. Merroun, A. Bouatem, N. Boutammachte, S. E. Alj, H. Ajdad, Z. Erregueragui, E. Zemmouri., “Impact of heliostat curvature on optical performance of Linear Fresnel solar concentrators,” *Renew. Energy*, vol. 89, pp. 463–474, 2016.

[32] R. Forristall, "Heat Transfer Analysis and Modeling of a Parabolic Tough Solar Receiver Implemented in Engineering Equation Solver", National Revewable Energy Laboratory, 2008.

[33] F. Burkholder and C. F. Kutscher, “Heat loss testing of Schott’s 2008 PTR70 parabolic trough receiver,” NREL Technical Report, 2009.

[34] A. Heimsath, F. Cuevas, A. Hofer, P. Nitz, and W. J. Platzer, “Linear Fresnel Collector receiver: Heat loss and temperatures,” *Energy Procedia*, vol. 49, pp. 386–397, 2013.

[35] R. G. Patil, D. M. Kale, S. V. Panse, and J. B. Joshi, “Numerical study of heat loss from a non-evacuated receiver of a solar collector,” *Energy Convers. Manag.*, vol. 78, pp. 617–626, 2014.

[36] R. G. Patil, S. V. Panse, and J. B. Joshi, “Optimization of non-evacuated receiver of solar collector having non-uniform temperature distribution for minimum heat loss,” *Energy Convers. Manag.*, vol. 85, pp. 70–84, 2014.

[37] K. S. Reddy and K. R. Kumar, “Estimation of convective and radiative heat losses from an inverted trapezoidal cavity receiver of solar linear Fresnel reflector system,” *Int. J. Therm. Sci.*, vol. 80, no. 1, pp. 48–57, 2014.

[38] E. Guadamud, A. Oliva, O. Lehmkuhl, I. Rodriguez, and I. González, “Thermal Analysis of a Receiver for Linear Fresnel Reflectors,” *Energy Procedia*, vol. 69, pp. 405–414, 2015.

[39] G. Xu, G. Song, X. Zhu, W. Gao, H. Li, and Y. Quan, “Performance evaluation of a direct vapor generation supercritical ORC system driven by linear Fresnel reflector solar concentrator,” *Appl. Therm. Eng.*, vol. 80, pp. 196–204, 2015.

[40] A. Hofer, F. Cuevas, A. Heimsath, P. Nitz, W. J. Platzer, and S. Scholl, “Extended Heat Loss and Temperature Analysis of Three Linear Fresnel Receiver Designs,” *Energy Procedia*, vol. 69, pp. 424–433, 2015.

[41] Y. Qiu, Y. L. He, Z. D. Cheng, and K. Wang, “Study on optical and thermal performance of a linear Fresnel solar reflector using molten salt as HTF with MCRT and FVM methods,” *Appl. Energy*, vol. 146, pp. 162–173, 2015.

[42] J. P. Ryan, "Incidence Angle Modifiers in Cylindrical solar Collector Design", MS Thesis, Colorado State University, 1997.

[43] M. J. Wagner, "Results and Comparison from the SAM Liner Fresnel Technology Performance Model", NREL/CP-5500-54758, 2012.

[44] M. Gunther, "Linear Fresnel Technology", enerMENA-DLR, www.energy-science.org, last visited on January 2017.

[45] H. Lee, "The geometric-optics relation between surface slope error and reflected ray error in solar concentrators", *Solar Energy*, vol. 101, pp. 299-307, 2014.

[46] E. Lupfert, "Reflector Shape Measurements: Solar Mirror Shape", 4th SFERA Summer School, 2013.

[47] Tonatiuh, https://code.google.com/archive/p/tonatiuh/, last visited on January 2017.

[48] Duffie, John A., and Beckman, William A.,"Solar Engineering of Thermal Processes " 3rd edition, New York: John Wiley and Sons, Inc., 2006.

[49] Incropera, Frank P.,and DeWitt, David P. "Fundamentals of Heat and Mass Transfer", 5th edition, New York: John Wiley and Sons, Inc., 2002.

[50] C. Ozalevli, "Algida Solar Pilot Project", TYT System Design Report, 2014.

[51] Meteonorm, http://www.meteonorm.com/, last visited on January 2017.

[52] The R Project for Satistical Computing, https://www.r-project.org/, last visited on January 2017.

APPENDIX A

RAY TRACING IN TONATIUH

This section provides a general overview of ray tracing program Tonatiuh. The window, shown in Figure A.1, is divided into three sections – 3-D View on the left which shows the design, Tree View on the right shows all the components in hierarchical order and Parameter Window on the right bottom allows user to define values of collector parameters. Additional sections include a menu bar and a tool bar.

The coordinate system in Tonatiuh is as follows:

- South → +z
- North → -z
- East → +x
- West → -x

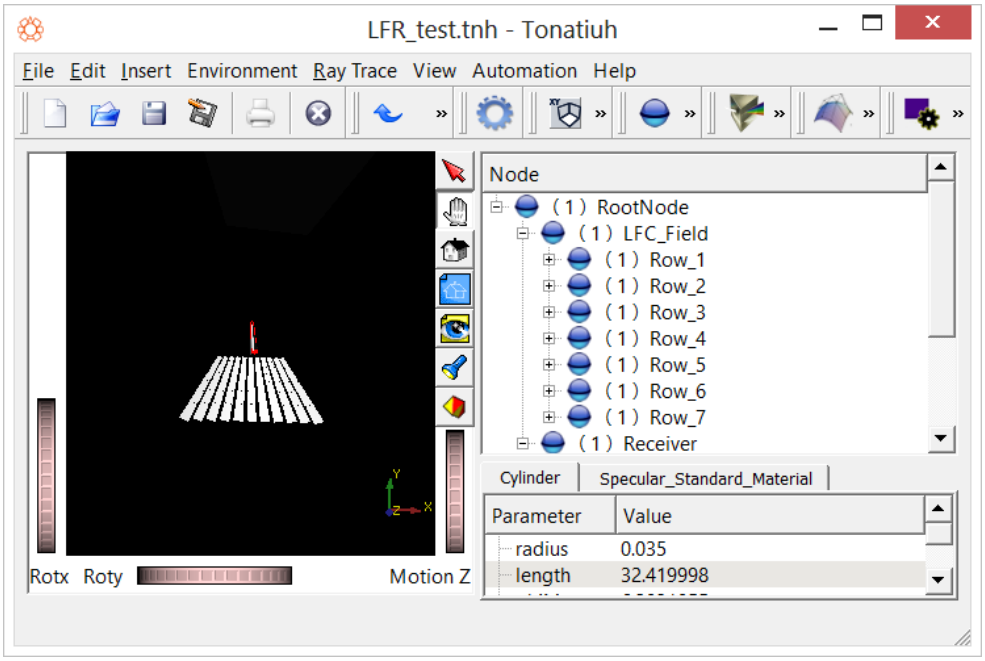

Figure A.1 Screenshot of Tonatiuh window.

Components can be added or removed by selecting ‘Group Node’ or ‘Surface Node’ from ‘Insert’ menu (Figure A.2). Group Node contains all sections and subsections including Surface Nodes and Tracker. Surface Node is used to define type of shape, material and optical properties.

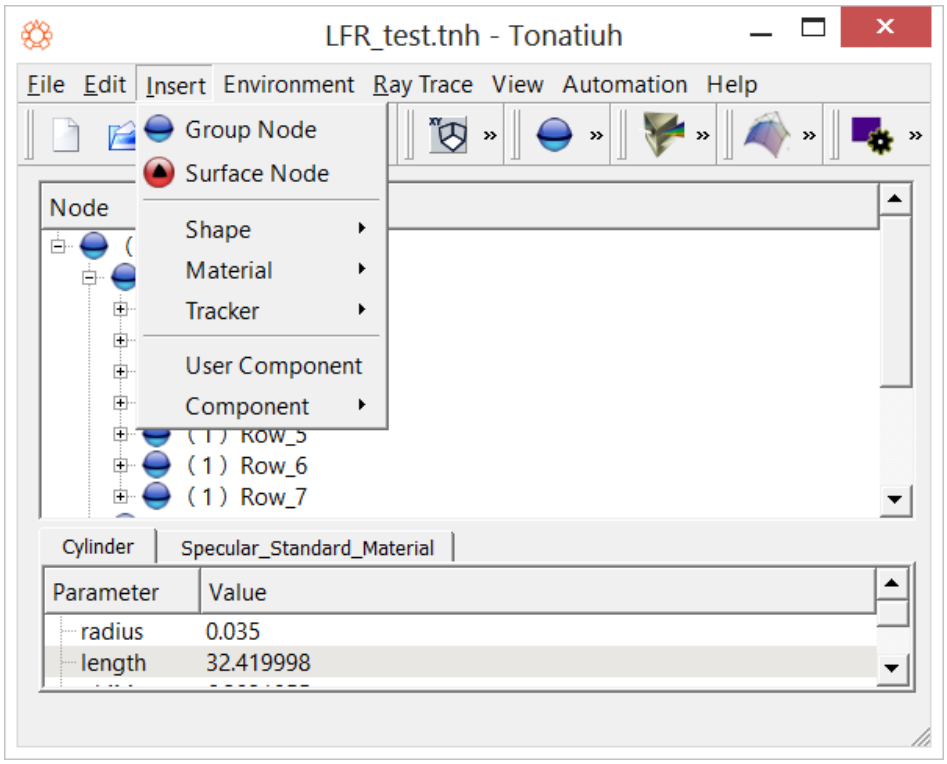

Figure A.2 Nodes in Tonatiuh.

After adding nodes, next step is to define shape, material and type of tracking method. There are many pre-defined shapes in Tonatiuh which can be seen in Figure A.3, ranging from flat rectangle to asymmetric compound parabola. Later dimensions and other physical properties are defined in Parameter Window.

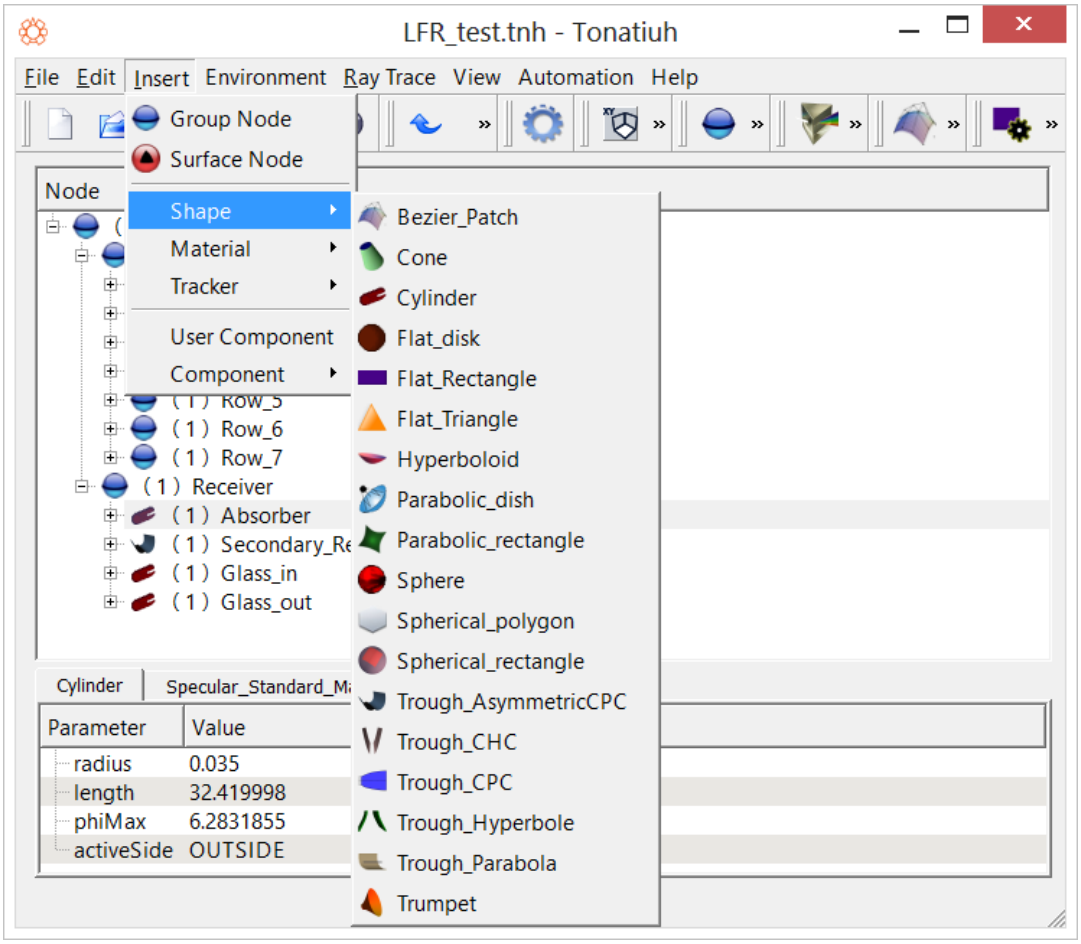

Figure A.3 Default shapes in Tonatiuh.

The ‘Material’ menu contains list of available materials, given in Figure A.4, which can be applied to the previously added shape, for instance, ‘Specular_Standard_Material’ is used for reflective surfaces such as mirrors. Again, optical properties are defined in Parameter Window. Similarly, tracking mode can be selected from ‘Tracker’ menu. Default tracking modes in Tonatiuh are illustrated in Figure A.5

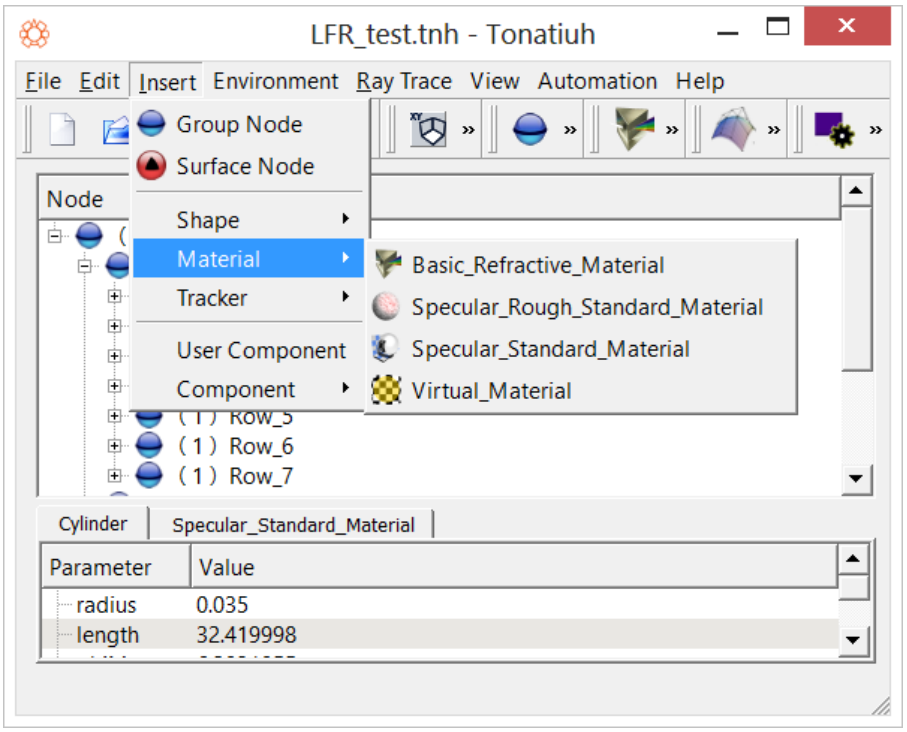

Figure A.4 Default materials in Tonatiuh.

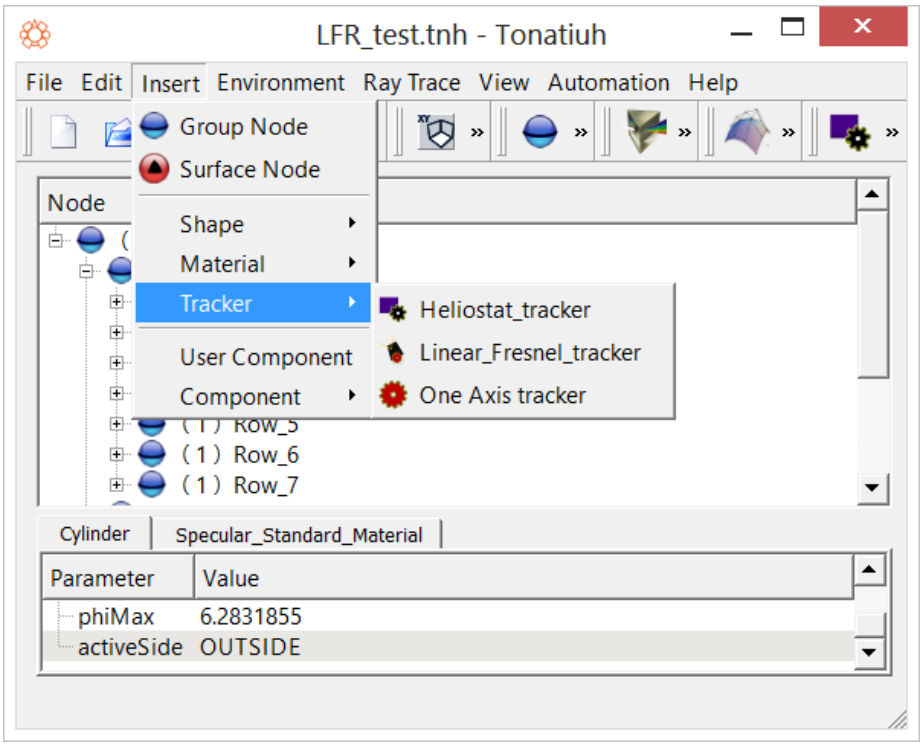

Figure A.5 Default tracking modes in Tonatiuh.

All parameters can be modified by simply selecting a component in the Tree View, for example, ‘Absorber’ node is selected from ‘Receiver’ Group Node and the absorber tube’s properties are shown in Parameter Window (Figure A.6) where absorber’s radius and length can be changed according to requirement. Furthermore, setting ‘activeSide = OUTSIDE’ means during ray tracing, the rays falling on the outside surface of absorber tube will be counted as ‘hit’.

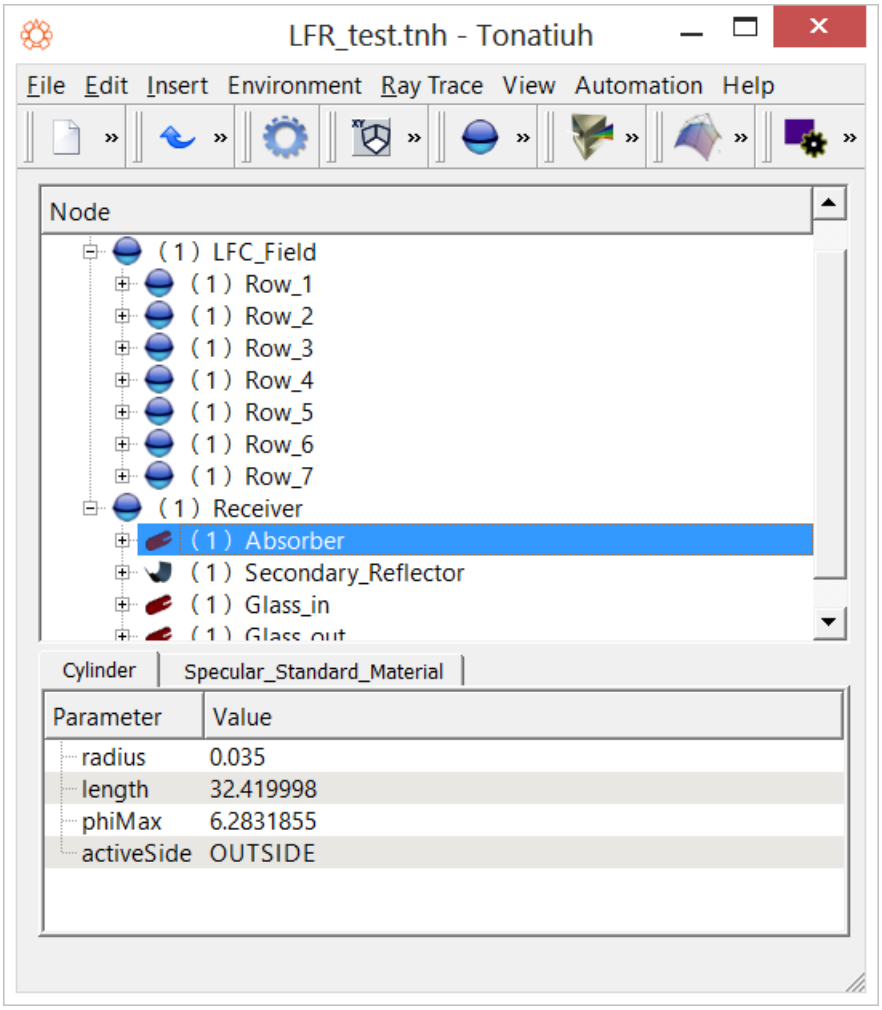

Figure A.6 Tree View and Parameter Window in Tonatiuh.

Additionally, sun shape and position is set from ‘Define Sun Light’ dialog box in ‘Environment’ menu. Pillbox and Buie are the types of sun shapes available in Tonatiuh which can be selected from ‘Sun Shape’ tab. Sun’s position in the sky can defined manually using ‘Sun Position’ tab as shown in Figure A.7 or ‘Sun Position Calculator’ can be used to find solar azimuth and solar zenith, for a particular time of year, just by entering coordinates of location and selecting the date. The ‘Sun Position Calculator’ is illustrated in Figure A.8

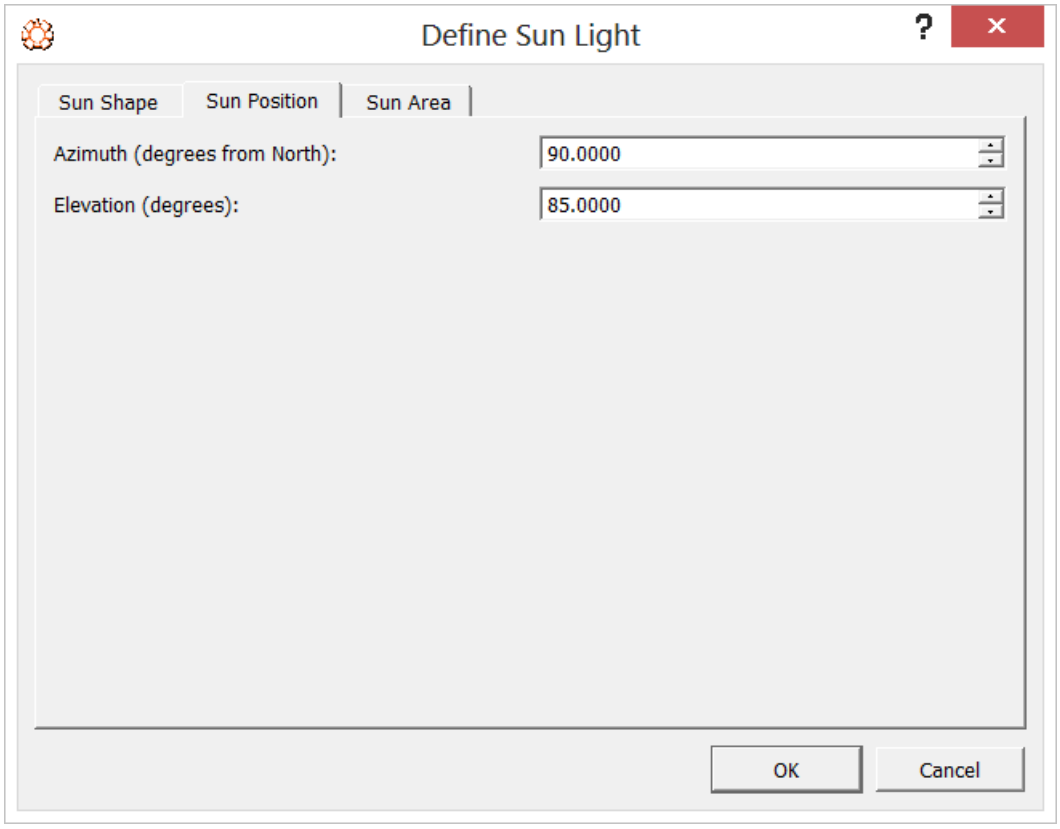

Figure A.7 Define Sun Light dialog box.

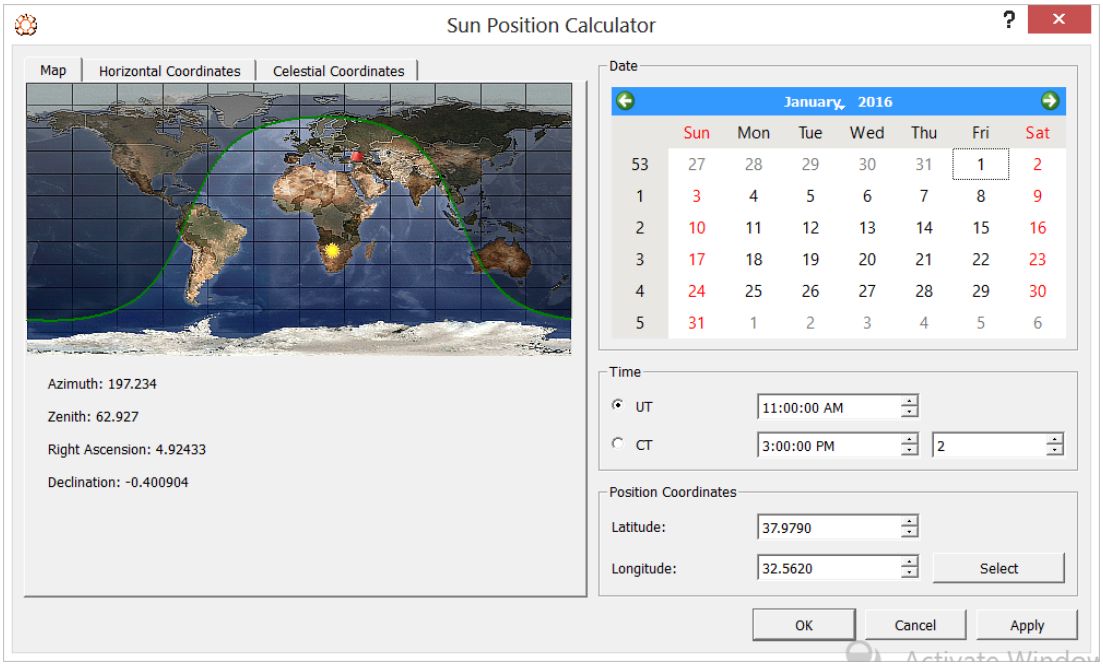

Figure A.8 Sun Position Calculator dialog box.

After completing the design and setting sun's geometry, ray tracing simulation is performed in two steps. First, ray tracing parameters like number of rays are specified in 'Options' dialog box, shown in Figure A.9, which can be found in 'Ray Trace' menu. Second step is to run the simulation, which is done by selecting 'Run' from 'Ray Trace' menu. This opens 'Photon Map Export Settings' window (Figure A.10) where following changes are made:

- Set 'Store type' to 'Binary_file'.
- Choose suitable location for saving output file in 'Directory name'.
- Enter name of output file in 'File name'.
- Uncheck 'Maximum number of photons per file' in case number of rays are more than 1,000,000.
- Select 'Export surfaces' and click 'Add' which opens a list.
- Choose 'Absorber' from the list and click 'OK'.
- Check 'Coordinates' and choose 'Local Coordinates'.
- Check 'Surface Identifier' and 'Surface Side' and then 'OK'.

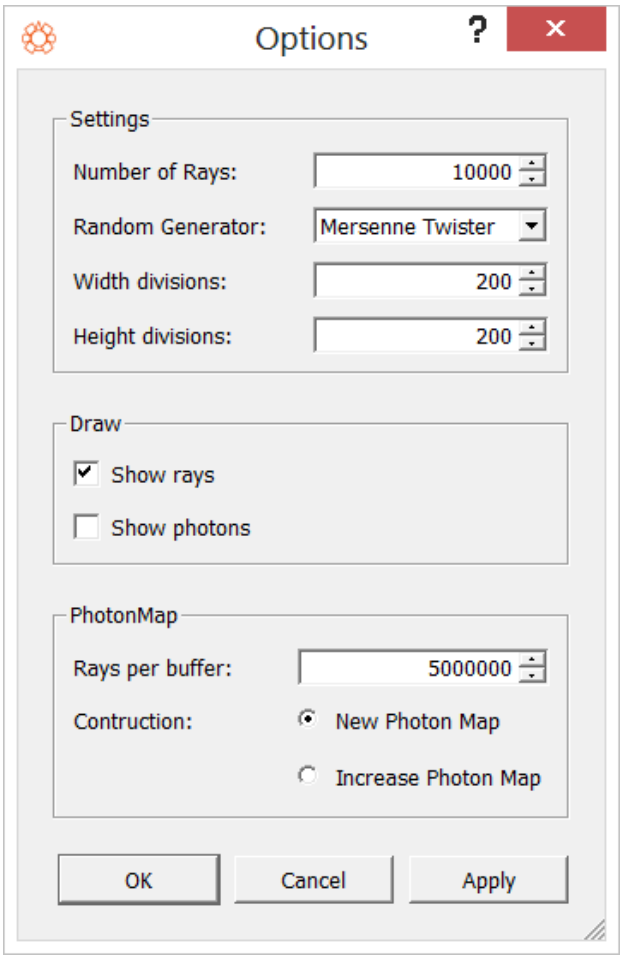

Figure A.9 Ray Trace Options dialog box.

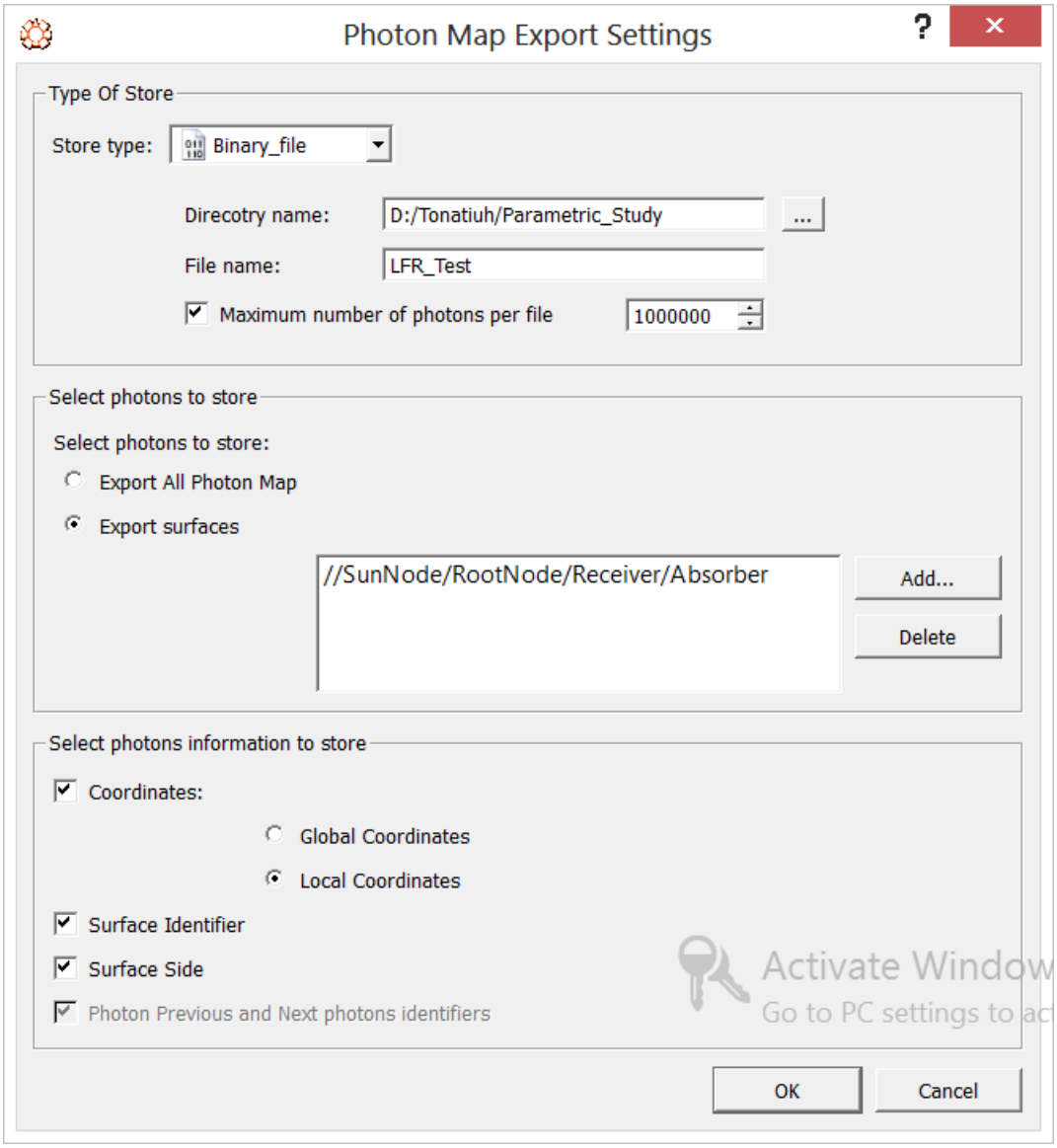

Figure A.10 Photon Map Export Settings dialog box.

After simulation is completed, Tonatiuh generates two files – ‘dat file’ and ‘txt file’. The ‘dat file’ contains photon path information and each photon us defined using six pointers – photon id, photon’s position in the 3-D space (x,y and z coordinates), photon incident side and surface ID. The ‘txt file’ shows how photon path information is organized in the binary data file. This structure is crucial for processing the ray tracing output. The content in the ‘txt file’ is illustrated below:

START PARAMETERS

id

x

y

z

side

surface ID

END PARAMETERS

START SURFACES

1 //SunNode/RootNode/Receiver/Absorber

END SURFACES

0.0634721

The number at the end is power per photon.

APPENDIX B

R-CODE FOR RAY TRACING

The output generated by Tonatiuh can be processed using code written in R [61]. The R-code given below reads photon data from ‘dat file’ creates a photon map which is used to calculate number of photons impinging on absorber surface and finally optical efficiency of the collector.

```
#Select the text file with exported parameters definition and save in a table
tablefileName<-as.matrix(read.csv2(file.choose(),skip=0,header=F,dec=".",sep =""))
tablefileName

#Read power per photon from row 12 and column 1 of the table
powerPerPhoton=as.double(tablefileName[12,1])
powerPerPhoton

#Select the binary file
filename = file(file.choose(),"rb")
filename
```

```
#Photon record from binary file is saved in "raw data" variable
endoffile = FALSE
rawdata = vector(mode="numeric")
rawdata

#Processing 1000 photon records per iteration and each photon record cosists of 6 numbers
nDataBlock = 6*10000
nDataBlock

while(!endoffile)
{
dataBlock = readBin(filename, what="numeric", n=vDataBlock, endian="big")
rawdata = append(rawdata, dataBlock)
if (length(dataBlock) < nDataBlock) endoffile = TRUE
}
#Close the file
close(filename)

#A photon map is created using 6 column matrix
photonmap = matrix(rawdata, ncol=6, byrow=T)
colnames(photonmap)= c("PhotonID","x","y","z","SideSurface","IDSurface")

#Number of photons hitting the absorber tube
numphotons = length(photonmap)/6
numphotons
```

```
#Total area of the collector
collector_area = 0.55*11*28
collector_area

#Total power incident on collector surface
tot_power = 1000*collector_area
tot_power

#Power incident on the absorber tube
abs_power = numphotons*powerPerPhoton
abs_power

#Optical efficiency of the collector
opt_eff = abs_power/tot_power
opt_eff
```